General Disclaimer

One or more of the Following Statements may affect this Document

- This document has been reproduced from the best copy furnished by the organizational source. It is being released in the interest of making available as much information as possible.

- This document may contain data, which exceeds the sheet parameters. It was furnished in this condition by the organizational source and is the best copy available.

- This document may contain tone-on-tone or color graphs, charts and/or pictures, which have been reproduced in black and white.

- This document is paginated as submitted by the original source.

- Portions of this document are not fully legible due to the historical nature of some of the material. However, it is the best reproduction available from the original submission.

NASA CR-145154

RESEARCH REPORT

RESONANCE TESTING OF SPACE SHUTTLE THERMOACOUSTIC STRUCTURAL SPECIMEN

By
A. L. Abrahamson
and
John Osinski

Prepared for:

NASA

NATIONAL AERONAUTICS AND SPACE ADMINISTRATION
LANGLEY RESEARCH CENTER
HAMPTON, VIRGINIA 23665

CONTRACT NUMBER NAS1 - 12841

WYLE LABORATORIES REPORT NUMBER 50621

MARCH 1977

WYLE LABORATORIES
SCIENTIFIC SERVICES & SYSTEMS GROUP
3200 MAGRUDER BLVD., HAMPTON, VIRGINIA

NASA CR-145154

RESEARCH REPORT

RESONANCE TESTING OF SPACE SHUTTLE THERMOACOUSTIC STRUCTURAL SPECIMEN

By
A. L. Abrahamson
and
John Osinski

Prepared for:

NASA

NATIONAL AERONAUTICS AND SPACE ADMINISTRATION
LANGLEY RESEARCH CENTER
HAMPTON, VIRGINIA 23665

CONTRACT NUMBER NAS1 - 12841

WYLE LABORATORIES REPORT NUMBER 50621

MARCH 1977

WYLE LABORATORIES
SCIENTIFIC SERVICES & SYSTEMS GROUP
3200 MAGRUDER BLVD., HAMPTON, VIRGINIA

1. Report No.	2. Government Accession No.	3. Recipient's Catalog No.
NASA CR-145154		

4. Title and Subtitle	5. Report Date
RESONANCE TESTING OF SPACE SHUTTLE THERMOACOUSTIC STRUCTURAL SPECIMEN	March 1977
	6. Performing Organization Code
7. Author(s)	8. Performing Organization Report No.
A. L. Abrahamson and John Osinski	50621
	10. Work Unit No.
9. Performing Organization Name and Address	
Wyle Laboratories 3200 Magruder Boulevard Hampton, Virginia 23666	11. Contract or Grant No. NAS1-12841
	13. Type of Report and Period Covered
12. Sponsoring Agency Name and Address	Contractor Report
National Aeronautics and Space Administration Washington, D.C. 20546	14. Sponsoring Agency Code

15. Supplementary Notes

FINAL REPORT

16. Abstract

This report describes the resonance testing of a structural specimen related to the space shuttle vehicle. The specimen consisted of a thin aluminum skin reinforced by hat-section stringers and supported by two ribs or bulkheads of corrugated web. A representative section of the space shuttle thermal protection system was bonded to the outer surface of the skin.

Initially, determination of modal deformation patterns was to be performed by using laser holography, but this method was discontinued because interpretation of the interference pattern was extremely difficult except for the lowest order modes.

The tests were completed by using miniature accelerometers to collect vibration data from locations forming a predetermined mesh over the tiles and base structure. The signals were recorded on FM magnetic tape and subsequently analyzed on a modal analysis system.

17. Key Words (Suggested by Author(s))		18. Distribution Statement
Modal Analysis	Thermoacoustic	Unclassified - Unlimited
Resonance Testing	Structural Damping	
Laser Holography	Panel Vibration	

19. Security Classif. (of this report)	20. Security Classif. (of this page)	21. No. of Pages	22. Price*
Unclassified	Unclassified	80	

*For sale by the National Technical Information Service, Springfield, Virginia 22151

TABLE OF CONTENTS

LIST OF TABLES AND FIGURES

LIST OF TABLES AND FIGURES (continued)

LIST OF TABLES AND FIGURES (continued)

LIST OF TABLES AND FIGURES (continued)

RESONANCE TESTING OF SPACE SHUTTLE THERMOACOUSTIC STRUCTURAL SPECIMEN

By
A. L. Abrahamson
and
John Osinski
Wyle Laboratories

1.0 SUMMARY

This report describes the resonance testing of a structural specimen related to the space shuttle vehicle. The specimen consisted of a thin aluminum skin reinforced by hat-section stringers and supported by two ribs or bulkheads of corrugated web. A representative section of the space shuttle thermal protection system was bonded to the outer surface of the skin.

Initially, determination of modal deformation patterns was to be performed by using laser holography, but this method was discontinued because interpretation of the interference pattern was extremely difficult except for the lowest order modes.

The tests were completed by using miniature accelerometers to collect vibration data from locations forming a predetermined mesh over the tiles and base structure. The signals were recorded for later analysis on a modal analysis system.

2.0 INTRODUCTION

During the design and development of a flight vehicle, the aerospace industry commonly constructs specimens which are representative of particular characteristics of the vehicle structure. These specimens may range from entire vehicle assemblies to individual components such as fins, fairings, wings or undercarriages, and are used for determining the behavior of the structure under simulated service conditions.

This report is concerned with resonance testing of a particular structural specimen described in Section 3.0 that is related to the space shuttle. The specimen consists of a thin aluminum skin reinforced by hat section stringers

and supported by two ribs or bulkheads of corrugated web. A representative section of the space shuttle thermal protection system is bonded to the outer surface of the skin. In subsequent tests, the specimen will be used for structural design verification in successive exposures to a simulated thermo-acoustic mission environment.

Resonance testing of the specimen prior to its subjection to simulated mission environments is required on the following grounds:

- Understanding of basic dynamic properties of the specimen is necessary for interpretation of structural failures in subsequent tests. (Reference Rucker and Mixson[1])

- Comparison of basic dynamic properties of the specimen with predictions from theoretical models qualifies theoretical approximations inherent in the models. (Reference Vaicaitis and Dowell[2], and Ojalvo and Ogilvie[3])

- Comparison of basic dynamic properties of the specimen in its current configuration with those before the addition of the thermal shield shows the effects of the thermal shield on resonant properties of the specimen.

Design of the space shuttle is uniquely different from any previous space flight vehicle because of the requirement for multiple reentries into the atmosphere. The basic structure is fairly conventional, however, thin aluminum skins are stiffened periodically by stringers along the span and ribs or frames along the chord. Different companies with different design philosophies designed different portions of the vehicle which resulted in slight variations in the structural configuration. For example, stringers of three different sections are found: hat section, T-section and integrally machined I-section.

Because the basic aluminum structure cannot withstand the high rate of kinetic heating encountered on reentry into the atmosphere, it is protected by a thermal shield of ceramic (silica) material. This material has a Young's modulus substantially lower than that of aluminum and fails at relatively low stress levels. Consequently, in design of the shuttle, it was necessary to ensure that deformations of the basic load-carrying aluminum structure do not induce stress above the failure limit of the thermal protection layer. The problem was solved by fabricating the thermal protection layer from small tiles. These tiles are generally about 15.2 cm (six inches) square with the depth tailored to predicted intensity of kinetic heating at each specific location on the vehicle skin. Tiles are not applied directly to the aluminum base structure which would transmit stresses, but to a strain isolator layer of Nomex felt.

The usual sonic fatigue problems which might occur on any aircraft or space vehicle are now augmented by a new problem, i.e., integrity of the thermal protection system. Predominant acoustic loads occur during lift-off with lower levels occurring on reentry. This sequence is critical, particularly since a failure resulting in loss of a tile on lift-off would not be noticed before reentry, and could result in catastrophic local overheating of the surface area from which it had become detached.

Sonic fatigue failure of the structure itself is probably immediately less likely to result in catastrophic failure. Past experience shows that sonic fatigue failures usually occur first on secondary structure, rather than primary structure, particularly in the vicinity of rivets, cleats and other attachment points.

Consequently, determination of the dynamic characteristics of the thermal protection system of the structural specimen was the principle objective of the resonance testing. The use of time-averaged laser holography to obtain pictorial images of structural modes was intended; however, for all but the lowest order modes, the interpretation of the interference pattern observed was extremely difficult. Due to the discontinuous nature of the tiled thermal shield, interference fringes between adjacent tiles were also discontinuous. In addition, the small degree of tile deformation superimposed on a large rigid body motion resulted in only small changes of gray on the photographs rather than clear black and white fringes. These difficulties, and the desirability of determining the behavior of the thermal tiles relative to that of the aluminum base structure, led to the decision to discontinue the holographic study. The experimental setup and preliminary results are described in Section 4.0.

Instead, miniature accelerometers were used to collect vibration data from locations forming a predetermined mesh over tiles and the base structure. The signals were recorded and subsequently analyzed using a Hewlett-Packard modal analysis system. The measurements and results of this method are described in Section 5.0.

3.0 DESCRIPTION OF THE STRUCTURAL SPECIMEN

The description of the structural specimen may be seen in the photograph and dimensional sketches shown in Figure 1. The specimen is designed for thermoacoustic testing of the space shuttle orbiter thermal protection system, the skin-stringer structure, and the interfaces between the skin-stringer panels and the rib bulkheads.

Thermal tiles of Lockheed LI900 silica material are 15.2 cm (6 inches square by 5.8 cm (2.3 inches) thick with a 2 mm (0.008-inch) thick ceramic coating. The strain isolator is 4 mm (0.16 inch) thick Nomex felt. The structure was fabricated from 2024T3 aluminum 0.81 mm (0.032 inch) thick by NASA and Rockwell International, prime contractor for the shuttle, who bonded the thermal coating to the tiles.

The skin-stringer panel is 91.4 cm (36 inches) long between supports and 45.7 cm (18 inches) wide. Overall length of the panel is 141 cm (55.5 inches). Seven hat-section stringers run parallel to the long edge of the panel. Stringer dimensions are given in Figure 1. Rib webs are 91.4 cm (36 inches) deep by 92.7 cm (36.5 inches) wide with flat-topped corrugations 2.54 cm (one inch) in width. Corrugations are angled at 30° from perpendicular and are nominally 2.54 cm (one inch) on each side (see Figure 1).

Stringers are continuous through the skin-rib joint. Attachment is by angles which join stringer apexes to flat sections of rib webs. Additional stiffening and distribution of stresses are accomplished by the use of cleats directly from rib webs to skin.

4.0 MODAL PATTERNS BY HOLOGRAPHY

4.1 HOLOGRAPHIC INTERFEROMETRY

To provide a background for discussing the results of holographic determinations of modal deformation patterns, the following description of holography and holographic interferometry is included.

The term "holography" is used to describe a means of recording and reconstructing the visual image of objects so that the result, incorporating both phase and amplitude information, is truly three-dimensional. A basic experimental configuration for producing and viewing holograms is shown in Figure 2.

When a hologram is made, light waves from a coherent source (a laser) are reflected from the object and interact with waves from the same source reflected from a mirror to form an interference pattern. The interference pattern in an arbitrary plane is the result of vector additions of the two beams and is called a hologram when it is recorded simply as an intensity distribution of a photographic plate. The virtual image of the object may be reconstructed by illuminating the hologram with laser light from the direction of the original reference beam. The concept of holography was first described by Gabor[4] and demonstrated by Leith and Upatnieks[5].

Although holography for the basic purpose of image reconstruction involves an interference pattern in the plane of the hologram, the term holographic interferometry is reserved for multiple exposure or time-averaged holography.

Holographic interferometry is used for measuring small motions or deformations of an object without the need for physical contact. To explain this procedure, consider a hologram of an object. Suppose the object is deformed or displaced slightly from its original position and the same hologram exposed a second time. When the double-exposed hologram is developed and illuminated with light from a coherent source, two images are produced. Although the relative deformation or displacement may be too small to be detected by the viewer, light from the two images interacts to produce a set of interference fringes in the form of light and dark bands superimposed on the double image of the object. It is possible to relate the fringes to surface deformations of the object, e. g., Haines and Hildebrand[6]; Brown, Grant and Stroke[7].

Time-averaged holography is similar to the multiple exposure holography just described. Consider the hologram of a flexible, continuous structure which is vibrating at a single frequency in one of its normal modes. Points on the structure which are vibrating at different amplitudes will appear as being of a different brightness when the image of the structure is ultimately reconstructed. This is the result of different degrees of phase modulation of the object beam by the different amplitudes of the two signals. The way in which different degrees of phase modulation result in different time-integrated brightness may be explained with reference to Figure 3a. Here, two bright bands are shown together with one band relatively darker. Relative degrees of shading may be calculated by summing light and dark areas under the sinusoid over one cycle. Clearly, the brightest band possible occurs on a structural node as shown in Figure 3b., where there is no motion and the amplitude of the sinusoid is zero. With each successive positive reinforcement between the two waves, the brightness decreases as shown in Figure 3b., until with excessive motion the distinction between dark gray areas and black fringe areas becomes impossible.

Excellent examples of the pictorial representation of structural modes by this technique of time-averaged holography may be seen in a report by Evenson and Aprahamian[8].

4.2 EXPERIMENTAL SETUP AND PROCEDURES

A fundamental requirement in holography is that the relative phase between object and reference beam must remain stable for the duration of the holographic exposure. To achieve this stability over long exposures necessary for low-power lasers, it is necessary to mount the laser, the structural specimen, the photographic plate, and all of the optics on a single seismic platform.

In the experimental setup shown in Figures 4 and 5 for producing time-averaged holograms of the space shuttle thermoacoustic test structure, a solid granite platform with dimensions of 2.44 m by 1.83 m by 25.4 cm was used. The platform rested on pneumatic supports to minimize vibration transmitted to the optical system. Also, disturbances transmitted to the optical system by airflow from the room heating and air-conditioning system were eliminated. This was achieved by turning the system off for the duration of the tests. Turning the system off during only the holographic exposure part of the tests produced different thermal changes in optical components during the exposure causing phase instability between object and reference beams.

A 50-milliwatt helium-neon laser instrument that produces a continuous source of light was used for this experiment. A photographic shutter, as shown in Figure 4, was placed immediately in front of the laser exit lens to control holographic exposure times. On passing through the shutter, the beam was turned through 90° by a mirror before being divided into object and reference beams by the beam splitter. This instrument consisted of a circular mirror supported on a central shaft enabling it to be rotated through 360°. The density of the reflecting surface is uniform along any radius, but varies continuously as a function of angle except at one value where it is discontinuous. Reflectivity and transmissibility of the mirror is thus dependent on its angle of rotation and is variable over a considerable range to allow intensity balancing of object and reference beams at the holographic plate. Both beams are expanded in the directions shown in Figure 4, by spatial filters. These instruments each consist of a lens system and a pinhole. The lens system collimates and focuses the beam on the pinhole which diffracts the beam causing it to expand as illustrated. Collimating and focusing reduce beam irregularities and increase light intensity at the pinhole giving the instrument its name, spatial filter.

Although a laser is spoken of as a source of coherent light, it is less than perfect in this respect. Coherence of the beam falls off rapidly at distances greater than a few inches so it is necessary to ensure that object and reference beams have almost equal path lengths. This is difficult to achieve due to the spatial distribution of the object, and careful adjustment is necessary to ensure good quality holograms.

A block diagram of the electronics and transducers used for exciting the test specimen and monitoring its response is also shown in Figure 4. The shaker was mounted close to the center of the skin-stringer panel while the accelerometer was moved to different positions to find peak responses at different frequencies.

During the experiment, the sine signal generator was swept manually from 20-1200 Hz and peaks of response monitored from the accelerometer output. These frequencies were noted for obtaining holograms.

In previous holographic studies of the test specimen (Reference 1) before installation of the thermal protection system, exposure times of a few seconds were possible. In the case of the specimen in its tiled configuration, exposure times of one minute or longer were required due to the relatively lower reflectivity of the tile surface.

4.3 DISCUSSION OF RESULTS

4.3.1 Modal Deformation of Untiled Test Specimen

To provide a basis for comparison with holograms of the tiled test specimen, consider briefly in a qualitative sense, examples of time-averaged holograms from Reference 1 of the test specimen before installation of the thermal shield.

Figure 6 shows a photograph of a time-averaged hologram that was taken while the structure was excited at 182 Hz. The brightest areas represent nodes or those areas where little or no movement took place. At this frequency, nodes occurred over the rib/bulkhead supports, and along two lines perpendicular to these, one-quarter span from the top and bottom panel edges.

Antinodes, points of maximum amplitude, occurred at the center of the dark ellipsoidal fringes, each fringe representing a contour of equal amplitude. We can now qualitatively depict the shape of the mode by a line drawing as shown below the photograph in Figure 6.

Similarly, a photograph of a time-averaged hologram, with a line drawing of the shape of the mode derived from it, of the same panel at 434 Hz is presented in Figure 7.

4.3.2 Modal Deformation of Thermal Protection System

The thermal protection system, which is described in detail in Section 2.0, is fabricated with a strain isolator bonded to the skin of the base aluminum structure and the ceramic tiles are in turn bonded to the strain isolator. Thus, each individual tile is free to respond to forces exerted on it by the structure below it, and itself to exert forces on this structure through the strain isolator. The motion of adjacent tiles is related only sofar as the integrated motions of the aluminum structure below them are related.

The type of motion thus expected from the thermal protection system, if it responds according to design, involves rigid body motion of tiles resulting from the integrated motion of the structure beneath each tile. Actual

deformation of the base structure beneath each tile is absorbed by stretching and compressing the strain isolator.

Motion of the structure and the strain isolator is indeterminable from holograms of the tiles; however, time-averaged holograms of the tiled face of the panel should provide information about rigid body motion and bending of the tiles themselves, which the photograph of the hologram shown in Figure 8 appears to yield. Nodal lines are clearly distinguishable and are generally linear across each tile. Fringes are also straight and spaced equally. A straight nodal line with parallel fringes across a tile indicate that the tile is rotating about that nodal line and that the curvature parallel to the nodal line is zero.

Curvature perpendicular to the nodal line may be determined from fringe spacing using the analysis of Powell and Stetson[9] whose results showed that the amplitude of vibration for points on the beam covered by a fringe can be related to the roots of J_o, the zero-order Bessel function. That is, a fringe is formed where

$$J_o(\Omega_i) = 0$$

and Ω_i is defined by

$$\Omega_i = \frac{2\pi}{\lambda} (\cos \theta_1 + \cos \theta_2) A_i$$

where

λ is the wavelength of light used to make the holograms

θ_1 is the angle between the displacement vector of the beam and the line of sight of the observer through the hologram

θ_2 is the angle between the displacement vector of the beam and the illuminating light source

A_1 is the amplitude of vibration (at fringe i)

The angles θ_1 and θ_2 are shown in Figure 4. A helium-neon laser was used in the experiments, and λ was 6238 Angstroms. At Ω_1, the first root of J_o, we have

$$\Omega_1 = 2.405 = \frac{2\pi}{\lambda} (\cos \theta_1 + \cos \theta_2) A_1$$

or

$$A_1 = \frac{\lambda}{2\pi(\cos \theta_1 + \cos \theta_2)} \frac{\Omega_1}{} = \frac{(12.1 \times 10^{-6} \text{ cm})}{\frac{1}{2} (\cos \theta_1 + \cos \theta_2)}$$

for the amplitude of vibration at the location of the first fringe. Similarly, the vibration amplitude A_2 corresponds to the second root, Ω_2, etc. Near the center of the beam, the optical arrangement was such that $\theta_1 = \theta_2 = 0$ and the amplitudes are especially easy to compute. The first five fringe numbers and the corresponding vibration amplitudes A_n are given in Table I.

TABLE I

Amplitude Determination for
Time-Averaged Holograms

Fringe Number	Root, Ω_i	Vibration Amplitude (cm)
1	2.405	12.1×10^{-6}
2	5.520	27.7
3	8.654	43.4
4	11.79	59.2
5	14.93	74.9

The results in Table I were used to calculate the deformation of six tiles from the fringe pattern shown on the photograph of the hologram in Figure 8. These calculated deformations which are shown below the photograph were readily derived from tiles where a node line was present. For other tiles, the small changes of shading from gray to black made it very difficult to determine deformation. Also, in the absence of a nodal line on a tile, there is no absolute reference with which to relate rigid body motion.

Other holograms taken at different frequencies show some interesting characteristics. For example in Figure 9, a close up of the fringes on one particular tile reveals that neither they nor the edges of the nodal line are completely straight, and the axis of rotation on adjacent tiles is not parallel and is discontinuous across tile boundaries.

Since we are concerned primarily with maximum tile curvature in a particular mode, it is desirable to take particular note of deformations on tiles where no nodal line exists because on these tiles maximum curvature is expected. It is on these tiles, however, where the measurement of fringe separation is most difficult.

This phenomenon may be explained if, with reference to Figure 3, we suppose that curvature across a tile is small compared with its rigid body motion. This is consistent with the theoretical results of references 2 and 3. Suppose that in two-dimensional bending of a tile, motion at its center (W_c) is described by:

$$W_c = A \sin \omega t \qquad (\omega = \text{frequency})$$

and that, at two opposite edges its motion (W_e) is given by:

$$W_e = .9\ A \sin \omega t$$

In order for a bright fringe to appear on the tile edges and a dark fringe across the tile center as shown, it is necessary that:

$$W_e = 6\lambda$$

$$W_c = 6.66\lambda$$

Thus, the smallest fringe order which yields any detail of the curvature is "7". However, it is extremely difficult to detect fringes of this high order, due to the small difference in integrated light intensity over one cycle between dark and bright fringes.

In the example considered in Figure 3, a fringe order of 7 is in fact not high enough to measure curvature with any confidence. Ideally, several bands

across a tile are required for this purpose. At higher frequencies holograms become even more difficult to interpret as shown by the many degrees of shading and complete lack of fringes in Figure 10.

Because of the difficulties encountered in measuring the curvature of the tiles and the greater desirability of using a method of modal analysis that gives information on the relative motion between the basic structure and thermal protection system, the study using holographic interferometry was discontinued in favor of using accelerometers as described in Section 5.0.

5.0 MODAL SURVEY USING ACCELEROMETERS

5.1 RATIONALE FOR USE

Theoretical analyses of aircraft skin-stringer panels excited by acoustic pressures have been frequently based on approximate models that treat these structures as simply supported orthotropic plates. The dynamics of the test structure under consideration can not be viewed as those of a simply supported two-dimensional orthotropic plate. In each mode, the corrugated rib/bulkhead support structure and the thermal protection system must be incorporated.

Experimentally, it is also necessary to determine the motion of the support structure and the thermal protection system, but time-averaged holography is not capable of giving phase relationships between the different elements of the test structure. Stored-beam holography is capable of showing phase, but a single hologram is not capable of "seeing" all members simultaneously, and due to the difficulties of fringe interpretation with the discontinuous tile structure, the decision was made to use accelerometers as vibration transducers for obtaining phase-calibrated data from all structural components.

5.2 EXPERIMENTAL PROCEDURE

The structure and shaker were mounted as described in Section 3.2 with the exception that the shaker was not mounted in the panel center, but at the point shown in Figure 11. White noise (from 20 to 200 Hz) from a signal generator was applied through a power amplifier to the shaker. Force exerted on the structure by the shaker was measured by a force gauge mounted in the stem of the shaker shaft.

Structural response was monitored by an array of five accelerometers which were moved successively to cover all positions shown in Figures 11, 12 and 13. In each position of the accelerometer array, accelerometer and force gauge outputs were recorded on FM magnetic tape for five minutes.

Before the tests, the accelerometers, the cables and associated electronics (see block diagram Figure 14) were calibrated against a "reference standard" accelerometer on an electrodynamic shaker. Amplifier gains on each channel were adjusted so that all accelerometers exhibited identical calibration at a frequency of 100 Hz. Frequency and phase response of the six systems were checked. Below frequencies of 2000 Hz, no significant difference between any of the channels was observed.

Three different types of accelerometer were used: Endevco type 22 (0.14 gm), Endevco type 2222 B (0.5 gm), and Endevco type 2226C (2.8 gm). For all positions on the thermal tiles (Figure 12) only Endevco type 22 accelerometers were used so as not to affect materially the dynamics of the tiles themselves.

5.3 DATA ANALYSIS THEORY

The data analysis theory of modal analysis from random data is well described in literature for the Hewlett-Packard model 5451B Fourier analyzer and in references 10 and 11. For completeness, however, the elements of the process are described below.

The basic assumptions implicit in the extraction of "modes" from structural response data are:

- Linearity (i.e., restoring force is proportional to displacement)
- Limited modal overlap (i.e., finite modal density and low damping)

Suppose that the structure is described in terms of a mathematically equivalent system of masses, springs, dampers and external forces related by a set of linear second order ordinary differential equations. For an n-degree of freedom system:

$$[M]\{\ddot{x}\} + [c]\{\dot{x}\} + [K]\{x\} = \{F\} \qquad \text{(Eq. 1)}$$

where

$[M]$ = mass matrix (nxn)

$[C]$ = damping matrix (nxn)

$[K]$ = stiffness matrix (nxn)

$\{F\}$ = force vector (nxn)

Taking the Laplace transform of equation 1 gives

$$B(s)\{X(s)\} = \{F(s)\} \qquad \text{(Eq. 2)}$$

where

$$[B(s)] = \left[[M]s^2 + [c]s + [K]\right] \qquad \text{(Eq. 3)}$$

$$\{X(s)\} = [H(s)]\{F(s)\}$$

where each element of the H(s) matrix is a transfer function. From the general form of equation 2, H(s) can always be written in partial fraction form as

$$[H(s)] = \sum_{k=1}^{2n} \frac{1}{s - p_k}[a_k]$$

where

n = number of degrees of freedom

p_k = kth root of equation obtained by setting $\det [B(s)] = 0$

$[a_k]$ = n x n residue for kth root

Except where the system is critically damped, the p_k's occur as a complex conjugate pairs and may be written as

$$p_k = \sigma_k + j\omega_k$$

and

$$p^*_k = \sigma_k - j\omega_k$$

The resonant frequency of the kth mode is given by

$$\Omega_k = (\sigma^2{}_k + \omega_k{}^2)^{\frac{1}{2}}$$

and the damping factor, or percentage of critical damping by

$$\xi = \frac{\sigma_k}{\Omega_k}$$

A single row or column of H(s) is sufficient to define all system mode shapes, since a mode shape of an elastic structure is usually independent from the point of excitation, although the amplitude is dependent upon the point of excitation.

5.4 DATA ANALYSIS PRACTICE

Calculation and storage of transfer functions is the first step in carrying out data analysis. A brief explanation of this process is shown in Figure 15. Consider two signals, one from the force gauge mounted on the shaker shaft and the second from an accelerometer mounted on the structure. In order to obtain the transfer function between input (force gauge) and output (accelerometer) it is necessary to obtain the following spectral functions:

- Power spectrum of force gauge signal (S_A)
- Power spectrum of accelerometer signal (S_B)
- Cross spectrum between accelerometer and force gauge (G_{AB})

The power spectrum is an array of real numbers and is obtained by taking the Fourier transform of the time history and multiplying it by its complex conjugate. Each number is associated with a particular frequency and represents the mean square power present in the signal at that particular frequency.

The cross spectrum is an array of complex numbers and is obtained by conjugate multiplying the Fourier transforms of two signals, accumulating the result, repeating the process for new time frames, and finally carrying out an ensemble average. The squared magnitude of each number represents the coherent part of the mean square power, present in the two signals at the associated frequency. The phase represents the phase relationship between the two signals at that frequency.

The transfer function defined by the expression,

$$H(f) = \frac{G_{AB}}{S_A}$$

has the phase of the cross spectrum between accelerometer and force gauge, but the magnitude of output/input or accelerometer amplitude normalized by force gauge amplitude.

Once transfer functions are calculated and stored in the analyzer on disk, a selection must be made on the portion of the structure to be displayed and corresponding accelerometer positions which will be used to determine its mode. Coordinates of these positions are fed into the analyzer with a sequence list of connecting lines to enable the graphics program in the analyzer to draw the structure. This information is stored on disk for later use.

Transfer functions from accelerometers, mounted in the positions defined above, are recalled from the disk by the operator and "fitted" with the analytical function described in the previous section. Briefly, this process is carried out as follows. Suppose the first transfer function in the sequence is recalled. In some way the analyzer must determine the number of resonances (modal frequencies) present in the transfer function, and must determine for each mode the values of:

- damping
- resonant frequency
- amplitude
- phase

which when substituted into the analytical expression give the best least-squares fit to the experimental transfer function.

This process requires the solution of an initially undetermined number of simultaneous nonlinear equations. The iterative techniques used for converging on a solution depend for convergence on the initial choices of a number of resonances and values of the variables listed above. Algorithms for initial determination of these parameters are contained in the analyzer, but operator intervention is allowed at this point for the following two reasons:

- Topology is difficult to program and what is obvious at a glance to a human operator may be unrecognizable to the machine.

- From a knowledge of the physical experiment, the operator may wish to ignore small amplitude resonances or may wish to concentrate his efforts in a particular frequency band.

The algorithm for selecting the number of resonances is appropriately called a "peak picker". It scans the amplitude part of the transfer function to find resonance peaks. Those peaks of lower amplitude, or outside the frequency bounds set by the operator, are ignored. Other algorithms then scan areas of the transfer function in regions of these peaks to find preliminary estimates of damping amplitude and phase. When this is completed, the analyzer enters these values into the equations for fitting the analytical expression to the experimental transfer function and carries out the number of iterations predetermined by the operator.

The analyzer then presents the operator with a view of experimental and analytical transfer functions. If the operator decides that the fit is good enough, he may suspend the operation, or if not good enough, instruct the analyzer to carry out more iterations.

This process is repeated on each transfer function in the set, with values of damping, resonant frequency, amplitude and phase for each resonance in each transfer function being stored in the analyzer.

When all transfer functions are processed, the analyzer is able to construct a modal vibration pattern for each resonant frequency simply by referring to the values of amplitude and phase already tabulated at that resonant frequency. These are associated with the coordinate data already resident in the analyzer and an animated isometric display of the structure vibrating in a particular mode is displayed on the viewing screen.

Tabulations of modal parameters may be obtained on the printer, while permanent copies of the isometric display at any point in the animation cycle may be obtained on a plotter.

5.5 EXPERIMENTAL RESULTS

Modal analysis of accelerometer data from the space shuttle thermoacoustic test panel was divided into the groups below for reasons that follow:

a. Frequency Range 0-230 Hz

- Aluminum skin-stringer panel only
- Aluminum skin-stringer panel with one rib/bulkhead supporting web

b. Frequency Range 0-450 Hz

- Aluminum skin-stringer panel only

c. Frequency Range 0-450 Hz and 0-2000 Hz

- Single tile and aluminum structure immediately behind
- Assembly of twelve tiles and base structure immediately behind

Because a finite Fourier transform always introduces smoothing leading to errors in modal damping amplitude and phase estimates, division of the analysis into the frequency groups above was necessary. Spectral resolution is simply the ratio of the maximum number of spectral points to the frequency range of the analysis. In its current configuration, the Fourier analyzer available for this project permitted a maximum of 1024 spectral points. Damping is usually a constant proportion of the center frequency of a resonance, so higher resolutions are required at low frequencies. Since structural damping was not known at first, the first analysis group was conducted at a conservative resolution of 0.24 Hz. Modes of both the base aluminum skin-stringer structure and the supporting corrugated web rib/bulkhead panel were determined.

The frequency range was then extended to 450 Hz and the entire analysis conducted again at a resolution of 0.49 Hz. It was found that modal patterns above 230 Hz possessed nonstationary nodal lines and deformation patterns changing continuously with frequency and not readily interpretable.

Examination of modes incorporating coupling between structure and tile motion was carried out over a frequency range from 0 to 1000 Hz. This was expected to provide adequate resolution due to higher tile damping and higher resonant frequencies.

Results from individual test groups are described in the following sections.

5.5.1 Modes of Base Aluminum Structure in Frequency Range 0-230 Hz

A limited number of accelerometer positions, at which data were recorded, were used for modal analysis in this frequency range. The expected orders of structural deformation were calculated and grids for resolving these experimentally were determined. Accelerometer position numbers for this portion of the analysis and their grid coordinate positions are shown in centimeters in

Figure 13. All accelerometer positions on the skin-stringer panel are on stringer apexes.

Typical transfer functions for several positions on the skin-stringer panel are shown in Figures 16 through 21. Isometric plots of modes on the skin-stringer panel and rib are shown in Figures 22 through 36.

Typical resonant peaks that occurred in the frequency range 0-230 Hz may be seen in Figures 16 or 21. These two figures contain transfer functions from positions 6 and 37 (Figure 13) on the skin-stringer panel. The positions are not located in a position of any obvious low-order symmetry on the panel and would not be expected to lie on a low-order mode nodal line and contain all frequency response peaks.

Major resonant peaks were seen at 67, 83, 93, 122, 140, 192, 204 Hz. Modal deformations on skin and rib for these frequencies are identified in isometric plots in Figures 22 through 26 and 29 through 34.

If axes are chosen, as shown in Figure 14, modes may be described by the number of modal lines parallel to these axes. Then an (X, Y) mode on the skin-stringer panel will have "X" nodal lines parallel to the X-axis (short side of panel) and "Y" modal lines parallel to the Y-axis (long side of panel). Modes corresponding to major resonances, on the skin-stringer panel are interpretable as:

	X	Y	
67 Hz	2	0	(Figure 22)
83 Hz	2	1	(Figure 24)
93 Hz	2	1	(Figure 26)
122 Hz	2	2	(Figure 29)
140 Hz	2	3	(Figure 31)
193 Hz	3	0	(Figure 33)
204 Hz	3	1	(Figure 35)
217 Hz	2	4	(Figure 36)
	3	2	(Figure 37)

Variations on the 93 Hz mode involving small differences in motion of the panel edges beyond the rib attachment points occur at 103 Hz and 108 Hz (See Figures 27 and 28). The amplitudes of these motions were so small that accurate data were not obtainable for them. Modal frequencies evident on the corrugated rib webs were identical to those on the front panel. To illustrate this coupled motion, modal deformations of a single rib web, together with the skin-stringer panel, are drawn in isometric plots at resonant frequencies in Figures 23, 25, 30, 32, 34, 36, 37, 38. It is evident from these plots that the skin-rib junction rotates in all modes without bending and that the junction remains at 90 degrees. Close to the junction, the number of nodal lines on the rib web parallel to the Z-axis corresponds to the number of nodal lines on the skin-stringer structure parallel to the Y-axis.

Farther away from the skin-rib junction, motion of the rib web becomes more difficult to characterize. Its behavior is less like that of a plate and more like an ensemble of parallel unconnected beams, each with slightly different edge conditions. This behavior occurs due to the great disparity in bending stiffness in the X and Z directions.

5.5.2 Modes of Base Aluminum Structure in Frequency Range 230-450 Hz

All accelerometer positions shown in Figure 11 were used for this part of the modal analysis on the expectation of high-order deformations of the structure.

Close examination of the transfer functions revealed the existence of resonant peaks consisting of a combination of many simple modes at frequencies above 210 Hz. For example, the transfer function, shown in Figure 39 taken from an accelerometer in a position close to the center of the skin-stringer panel, contains a wide resonance peak from 210 to 250 Hz which does not represent one single mode of varying amplitude possessing a constant deformation pattern throughout the frequency range, but a continually changing combination of coupled modes (Figures 37 and 38).

At higher frequencies, interpretation of the deformation patterns becomes still more difficult as modal density increases. Modes are intrinsically coupled and the result may no longer be regarded as the superposition of a few single-degree-of-freedom systems. As an example of this type of response, the power spectrum of an accelerometer signal from a position close to the panel center is shown in Figure 40. The broad response peak from 500 to 1000 Hz is not due to inadequate spectral resolution, but to the coupling described above.

Because of difficulty in interpretation of the "modal" deformation patterns at higher frequencies and because most acoustic energy during lift-off of the space shuttle falls at lower frequencies, no further isometric plots of the deformation pattern were obtained.

5.5.3 Coupled Vibration of Aluminum Base Structure and Thermal Protection System

Accelerometer positions on the tiles of the thermal protection system and their mirror image positions on the rear of the skin-stringer aluminum structure are shown in Figure 12.

Two separate aspects of the test are described: a) an intensive study of the motion of a single tile, and b) a more general study of an ensemble of twelve adjacent tiles. In both cases, tile resonant frequencies corresponded roughly with resonances of the base aluminum structure below a frequency of 210 Hz.

Above this frequency, both structural response and tile response were broadband in nature with frequencies of major peaks not necessarily coincident (Figure 41).

Typical displacement patterns of a single tile (Tile 12, Figure 12) are shown in Figures 42 through 45. Figure 42 shows that at 67 Hz the tile moved in phase with the base structure with little compression or extension of the strain isolator. Curvature is evident in the base structure but negligible in the tile itself. At 140 Hz (Figure 43), the tile still moved in phase with the base structure with small compression and extension of the strain isolator, but tile curvature was 180° out of phase with structural curvature and was of comparable magnitude in some directions.

The first "tile-bouncing mode" occured at 233 Hz (Figure 44). Tile and structural motions are in phase but tile displacement greatly exceeds displacement of the base structure. Curvatures are in phase and of comparable magnitude.

At 474 Hz, phase relationships between tile and structure are extremely complex as seen in the isometric plots in Figure 45. Substantial extension and compression of the strain isolator exists throughout the motion but tile curvature is negligible compared with the curvature of the base structure.

The degree of strain isolator extension or compression relative to displacement of the base structure for the entire range of resonant response is summarized in the form of a bar chart in Figure 46. A rapid rise in this ratio with the first tile-bouncing mode is evident following low initial values. From this chart, maximum dynamic stresses tending to separate the tile from the strain isolator should occur in the frequency region of 220-300 Hz with significant stresses also occurring in the range 580-670 Hz.

Data from Figure 46 gives a ratio of 0.17 for isolator extension/panel displacement in the 67 Hz mode, and a frequency of 233 Hz for the tile-bouncing mode. Theory suggests values for these two parameters of 0.02 and 685 Hz.

Dowell[12] has shown that these may be reconciled if one assumes the isolator modulus is lower than nominal:

$$\left\{\frac{685}{233}\right\}^2 \sim \left\{.17/.02\right\} \sim 8.5$$

The frequency (squared) should scale with modulus, and also the isolator deflection should scale inversely with modulus. Hence, the above data may be used to infer that the nominal isolator modulus of 1.03×10^5 N/m^2 (15 psi) should be reduced to

$$15/8.5 = 1.22 \times 10^4 \text{N/m}^2 (1.77 \text{ psi})$$

The ratio of tile curvature to base structure curvature was plotted over the range of resonant response at the same peaks as plotted above for the isolator extension (Figure 47). Tile curvature was estimated from acceleration amplitudes taken from the three lines comprising three accelerometers (see Figures 42-45). In each of the three lines, displacement was assumed to be half-wave sinusoid. This ratio is equal to, or slightly less than unity in the frequency region 140-360 Hz. Above 360 Hz, tile curvature is small; while below 140 Hz, tile curvature is roughly equal to one-half of the curvature of the base structure.

The ratio of tile curvature to panel curvature was determined in the following way. Suppose the displacement (W) of a single tile in an arbitrary direction "x" is given by:

$$W_t = \left(A_t \frac{\cos 2\pi x}{a} + B_t x + C_t\right) e^{i(\omega t + \phi_t)}$$

where a = tile dimension in x direction

A_t, B_t, C_t = constants

ω = frequency

ϕ_t = phase

and Bx + C represents the rigid body motion of the tile. Acceleration is given by:

$$\ddot{W}_t = \frac{d^2 W_t}{dt^2} = -\omega^2 W_t$$

and curvature by:

$$W_t'' = \frac{d^2 W_t}{dx^2} = -\frac{1}{\omega^2}\frac{d^2}{dx^2}(\ddot{W}_t) = -\frac{1}{\omega^2}\ddot{W}_t''$$

$$= -\frac{4\pi^2}{a^2} A_t \cos\frac{2\pi x}{a} e^{i(\omega t + \phi_t)}$$

Similarly, if panel curvature is given by:

$$W_p = \left(A_p \cos\frac{2\pi x}{a} + B_{px} + C_p\right) e^{i(\omega t + \phi_p)}$$

then $W_p = -\omega^2 W_p$

and $W''_p = -\frac{4\pi^2}{a^2} A_p \cos\frac{2\pi x}{a} e^{i(\omega t + \phi_p)}$

Suppose we choose to measure W''_t at a time (t_1) in the cycle when

$$\omega t_1 + \phi_t = 2n\pi \qquad (n = \text{integer})$$

and suppose we choose to measure W''_p at another time (t_2) in the cycle when

$$\omega t_2 + \phi_p = 2n\pi$$

$$\text{Then } W''_t\big|_{t = t_1} = -\frac{4\pi^2}{a^2} A_t \cos\frac{2\pi x}{a}$$

$$\text{and } W''_p\big|_{t = t_2} = -\frac{4\pi^2}{a^2} A_p \cos\frac{2\pi x}{a}$$

The ratio of these two quantities is then:

$$\frac{W''_t\big|_{t = t_1}}{W''_p\big|_{t = t_2}} = \frac{\ddot{W}''\big|_{t = t_1}}{\ddot{W}''\big|_{t = t_2}} = \frac{A_t}{A_p}$$

Experimentally, the ratio of $\frac{A_t}{A_p}$ may be determined at $x = 0$ by simply subtracting the rigid body motion from the accelerometer data. This was performed for curvature in three directions from the three lines comprising three accelerometers each at each resonant frequency in isometric plots similar to those shown in Figures 42-45. The rigid body motion is subtracted simply by measuring the perpendicular heights of the various triangles formed by the displaced lines of three accelerometers as shown for some examples in Figure 40.

Modes of the ensemble of 12 adjacent tiles from the center of the panel arranged in a 3 x 4 array are plotted together with the deformation of the

skin-stringer panel and shown in Figures 48 through 53. Only points at the centers of each tile are shown in the plots. Lines connecting the points are justified in the case of the base structure which is a continuous structure, but do not represent actual displacement in the case of the tiles because the tiles are not connected to each other.

These plots show panel displacement, tile displacement, and strain isolator extension simultaneously for the twelve tiles under consideration.

5.5.4 Damping

Damping in a built-up structure results from complex processes within the constitutive materials and joints of the structure which cause the transfer of mechanical energy into heat. Modal damping is usually assumed either to be proportional to velocity, or to the strain energy of the modal deformed structure. Clearly, neither of these assumptions is accurate, but no better approximations are in common use.

Experimental values of modal damping are used to provide proportional constants in these relations but are also useful for providing a basis of comparison for the damping properties of different structural configurations.

Values of modal damping for the space shuttle thermoacoustic test specimen are summarized below where measurements taken from transfer functions on the skin-stringer structure are averaged separately from those taken on the thermal protection tiles. Modal damping is given as a percentage of critical damping based upon the single degree of freedom analogy.

TABLE II

Values of Modal Damping

Modal Frequency	Damping % Measured on Structure	Std. Dev.	No. Meas.	Damping % Measured on Tiles	Std. Dev.	No. Meas.
67 Hz	0.30±	0.02	24	0.51±	0.06	5
83 Hz	1.13±	0.25	23	0.64±	0.02	4
94 Hz	0.77±	0.08	22	0.62±	0.05	3
122 Hz	0.74±	0.10	25	1.20±	0.15	4
140 Hz	1.20±	0.07	22	1.80±	0.10	4
193 Hz	0.36±	0.03	40	1.10±	0.10	3
204 Hz	0.72±	0.10	19	2.10±	0.90	4

The values shown in Table II are typical of damping factors measured on an aircraft structure above 50 Hz. Little difference is evident between these results and those reported in Reference 1 for the same test structure before the addition of tiles and the strain isolator. This indicates that the addition of these items has little effect on structural damping below 210 Hz.

Above 210 Hz, however, increased damping evident from the modal coupling described earlier is almost certainly attributable to the addition of the thermal protection system.

6.0 CONCLUSIONS

This report describes techniques and results of tests to determine the resonant properties of a space shuttle thermoacoustic test specimen.

The space shuttle consists essentially of a conventional lightweight aircraft type, aluminum load-carrying structure with a unique thermal protection system.

A substantial amount of both theoretical and experimental experience exists concerning an aircraft type aluminum structure. Thus, resonant properties and fatigue characteristics of the space shuttle structure are perhaps less interesting than the dynamic behavior of the thermal protection system and its potential failure characteristics.

Most significant of the results from these tests are the following:

- Addition of the thermal protection system to the aluminum structure does not increase structural damping significantly except in high-order modes.

- Tile curvature is comparable in magnitude to panel curvature at modal frequencies below 400 Hz (see Figure 47).

- Amplitude of the extension-compression cycle of the strain isolator exceeds the amplitude of panel displacement by substantial amounts in many modes (see Figure 46).

- Nominal strain isolator, Young's modulus of $1.03 \times 10^5 N/m^2$ (15 psi) should be reduced to $1.22 \times 10^4 N/m^2$ (1.77 psi) for computations of tile dynamics.

REFERENCES

1. Rucker, C. E., and Mixson, J. W., "Vibroacoustic Testing of Space Shuttle Thermal Protection System Panels," paper presented at AIAA/ASME/ASE 17th Structures, Structural Dynamics, and Materials Conference, Valley Forge, Pennsylvania, May 1976.

2. Vaicaitis, R. and Dowell, E. H., "Response of Reusable Surface Insulation Panels to Random Pressure," paper presented at AIAA/ASME/ASE 17th Structures, Structural Dynamics, and Materials Conference, Valley Forge, Pennsylvania, May 1976.

3. Ojalvo, I. U. and Ogilvie, P. L., "Modal Analysis and Dynamic Stresses for Acoustically Excited Shuttle Insulation Tiles," paper presented at AIAA/ASME/ASE 17th Structures, Structural Dynamics, and Materials Conference, Valley Forge, Pennsylvania, May 1976.

4. Gabor, D., "Microscopy by Reconstructed Wavefronts," Proc. of the Royal Society (London), Series A, Vol. 197, pp. 457-484, 1949.

5. Leith, E. N., and Upatnieks, J., "Wavefront Reconstruction with Diffuse Illumination and Three-Dimensional Objects," Journal of the Optical Society of America, Vol. 54, No. 11, pp. 1295-1301, November 1964.

6. Haines, K. A., and Hildebrand, B. P., "Surface Deformation Measurement Using the Wavefront Reconstruction Technique," Applied Optics, Vol. 5, No. 4, pp. 595-602, April 1966.

7. Brown, G. M., Grant, R. M., and Stroke, G. W., "Theory of Holographic Interferometry," Journal of the Acoustical Society of America, Vol. 45, No. 5, pp. 1166-1197, May 1969.

8. Evenson, D. A., and Aprahamian, R., "Applications of Holography to Vibrations, Transient Response, and Wave Propagation," NASA Contractor Report - NASA CR-1671, December 1970.

9. Powell, R. L., and Stetson, R. A., "Interferometric Hologram Evaluation and Real Time Vibration Analysis of Diffuse Objects," Journal of the Optical Society of America, Vol. 55, No. 12, pp. 1694-1695, 1965.

10. Ramsey, K. A., "Effective Measurements for Structural Dynamics Testing," Sound and Vibration, pp. 24-35, November 1975.

11. Ramsey, K. A., "Effective Measurements for Structural Dynamics Testing, "Sound and Vibration, pp. 18-31, April 1976.

12. Dowell, E. H., private communication, December 1976.

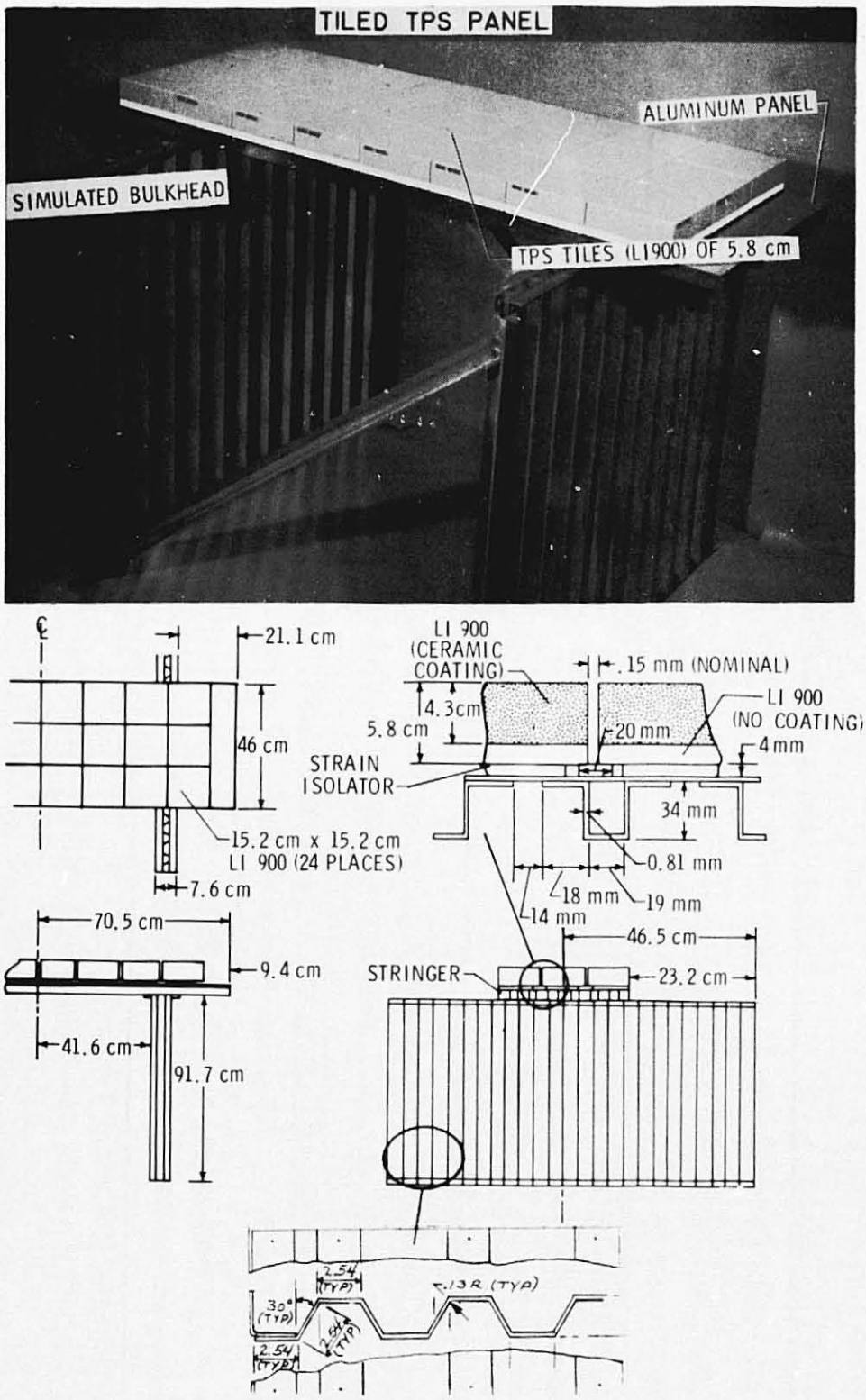

Figure 1. Test Specimen.

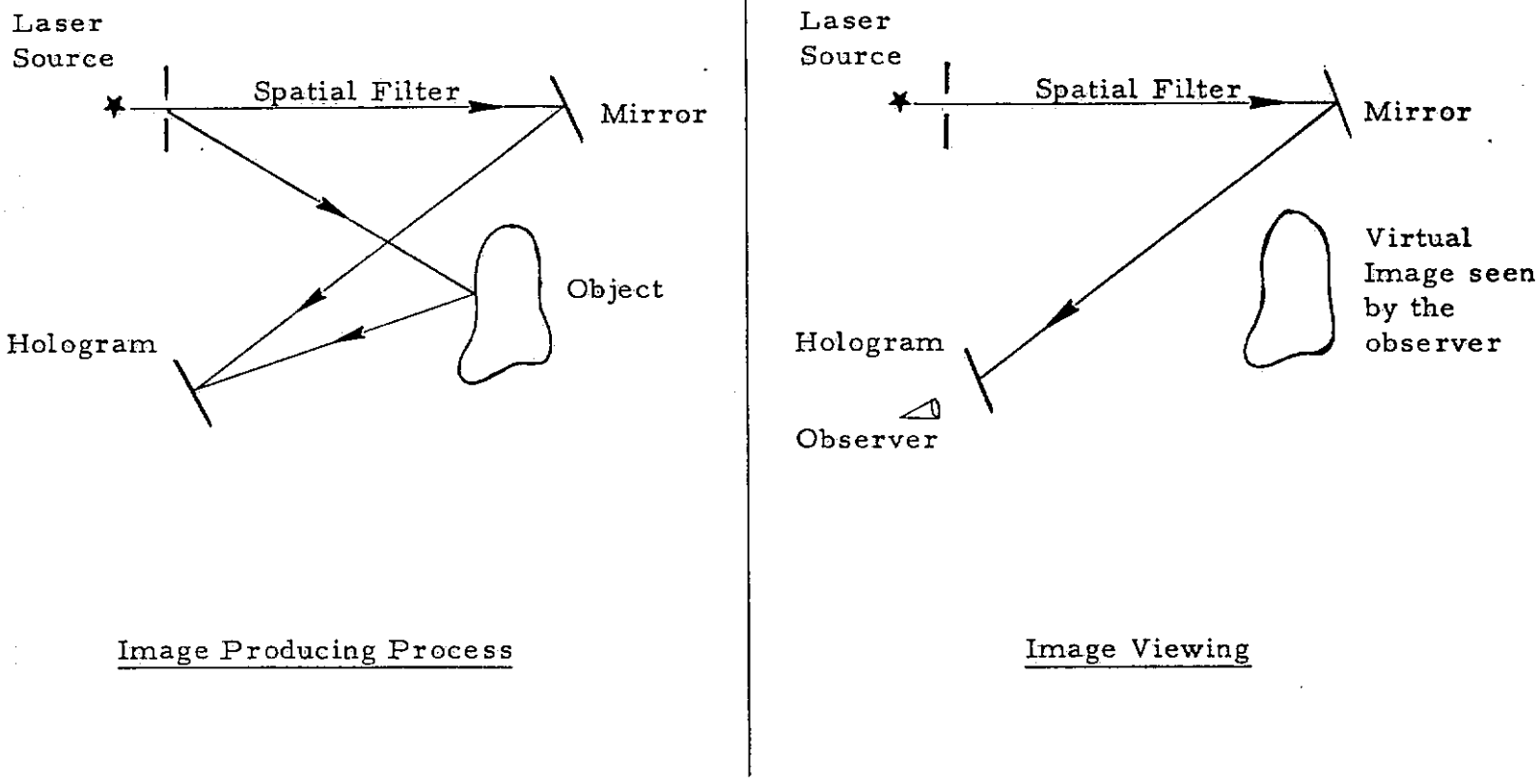

Figure 2. Basic Experimental Configuration for Producing and Viewing Holograms.

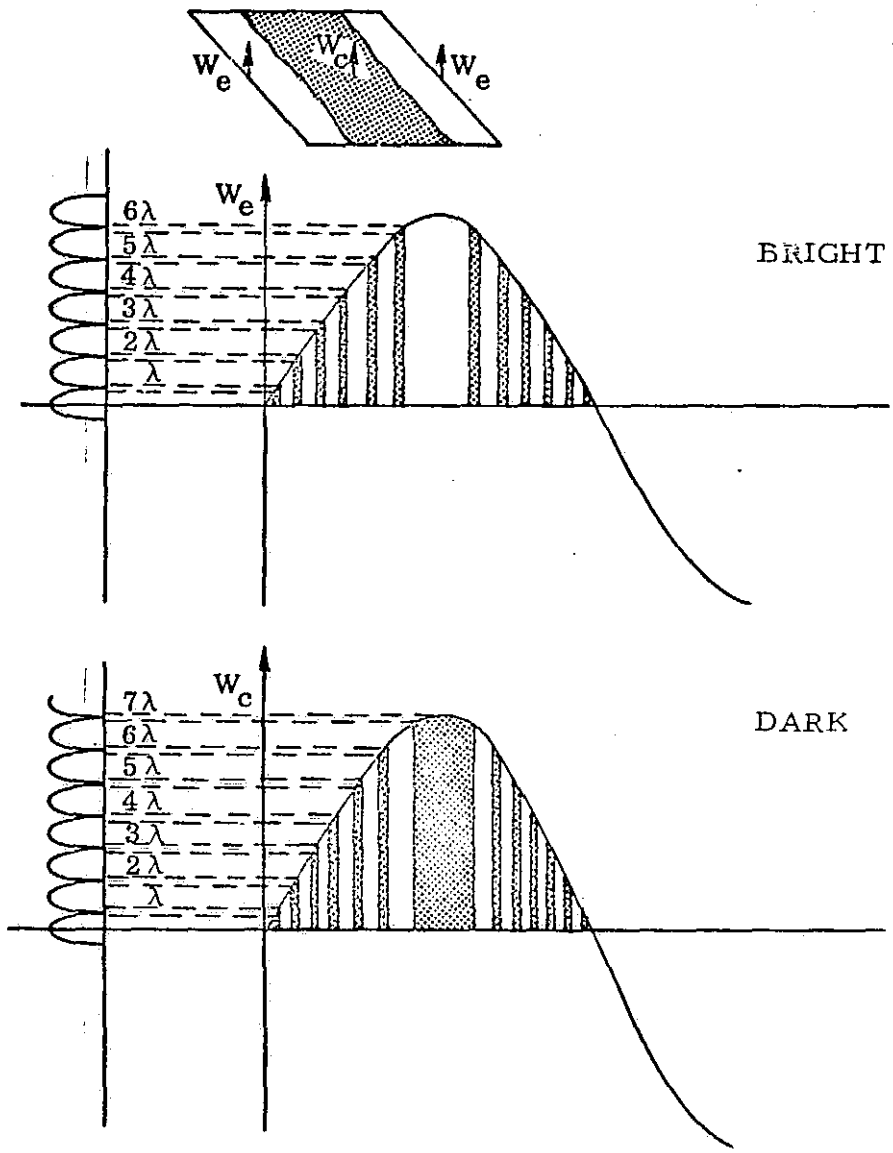

Figure 3a. Occurrence of a Bonded Structure on a Time-Averaged Hologram of a Vibrating Tile.

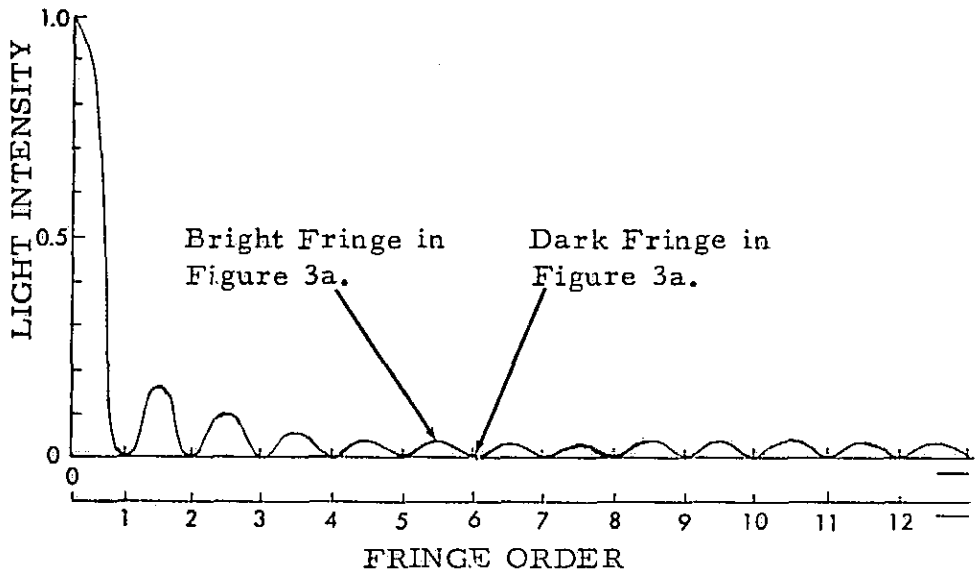

Figure 3b. Plot of Light Intensity versus Fringe Order for a Time-Averaged Hologram.

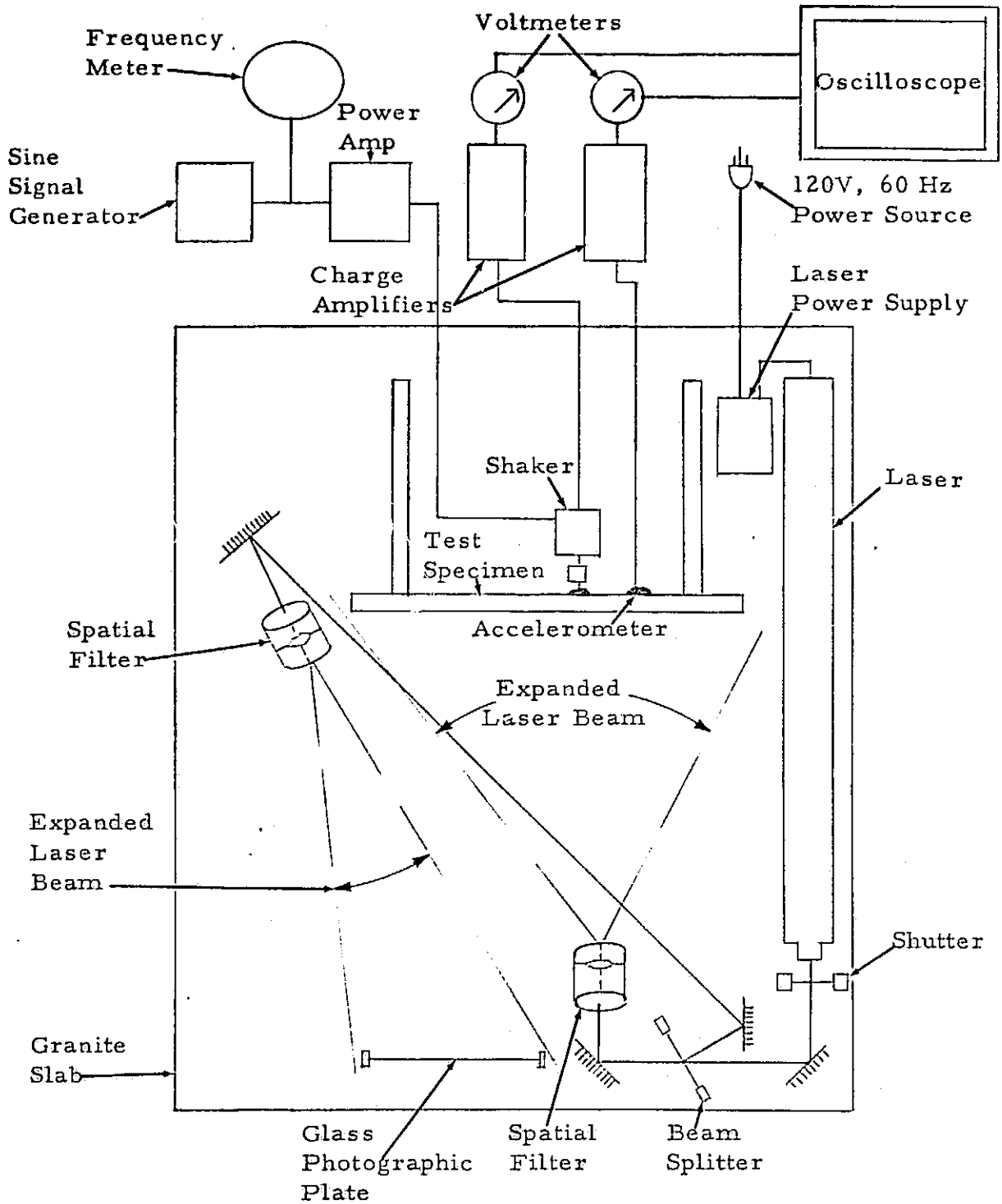

Figure 4. Experimental Setup for Time-Averaged Holography.

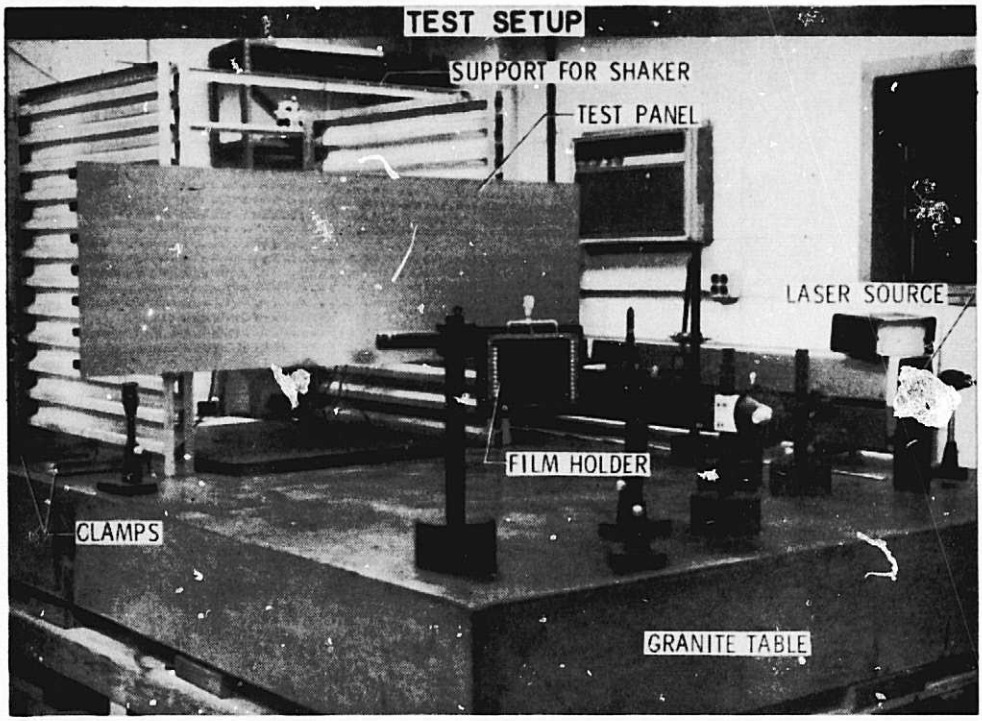

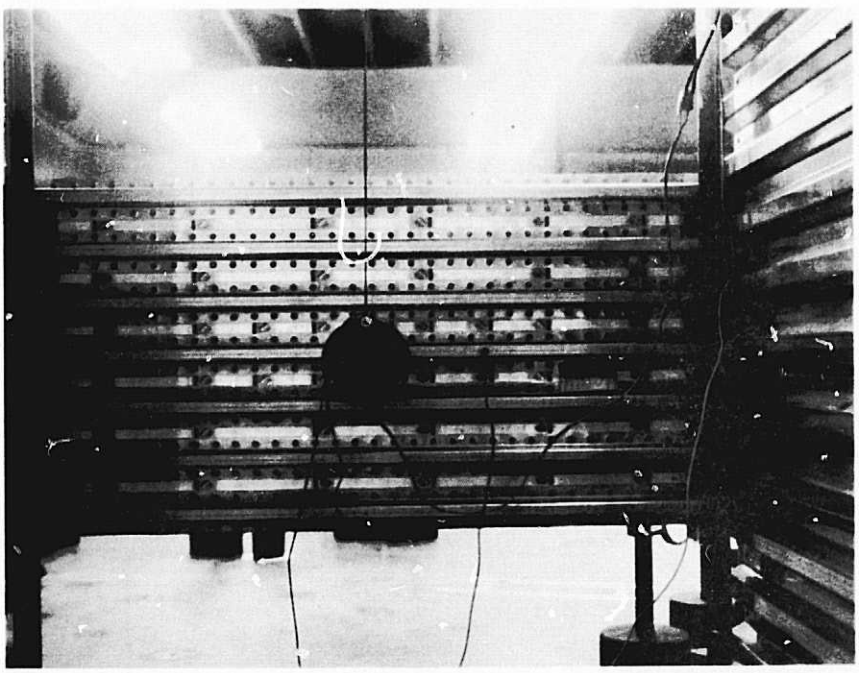

Figure 5. Experimental Configuration Used for Producing Holograms of the Space Shuttle Test Panel.

Figure 6. Time-Averaged Hologram of Untiled Panel, 182 Hz.

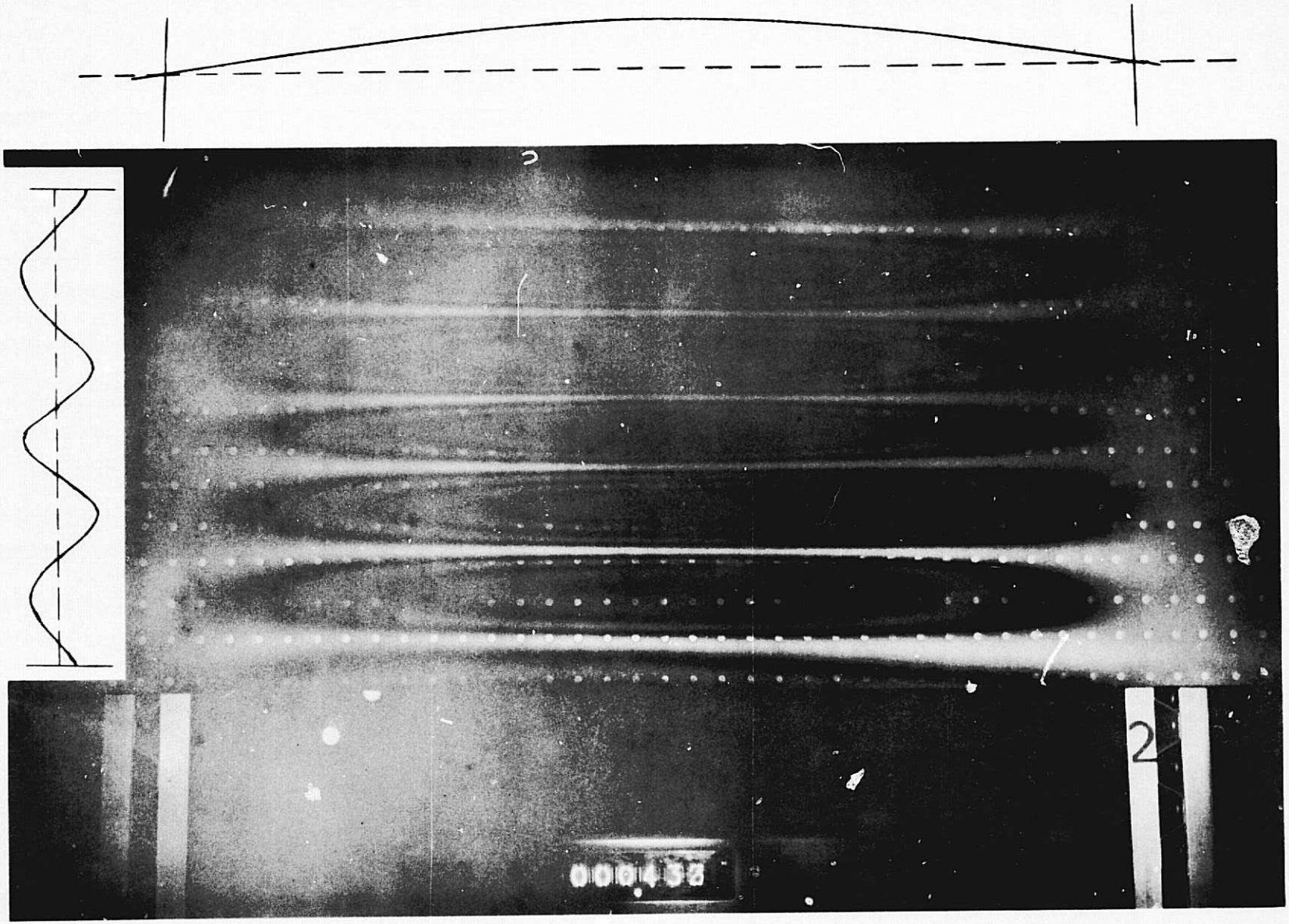

Figure 7. Time-Averaged Hologram of the Untiled Panel, 434 Hz.

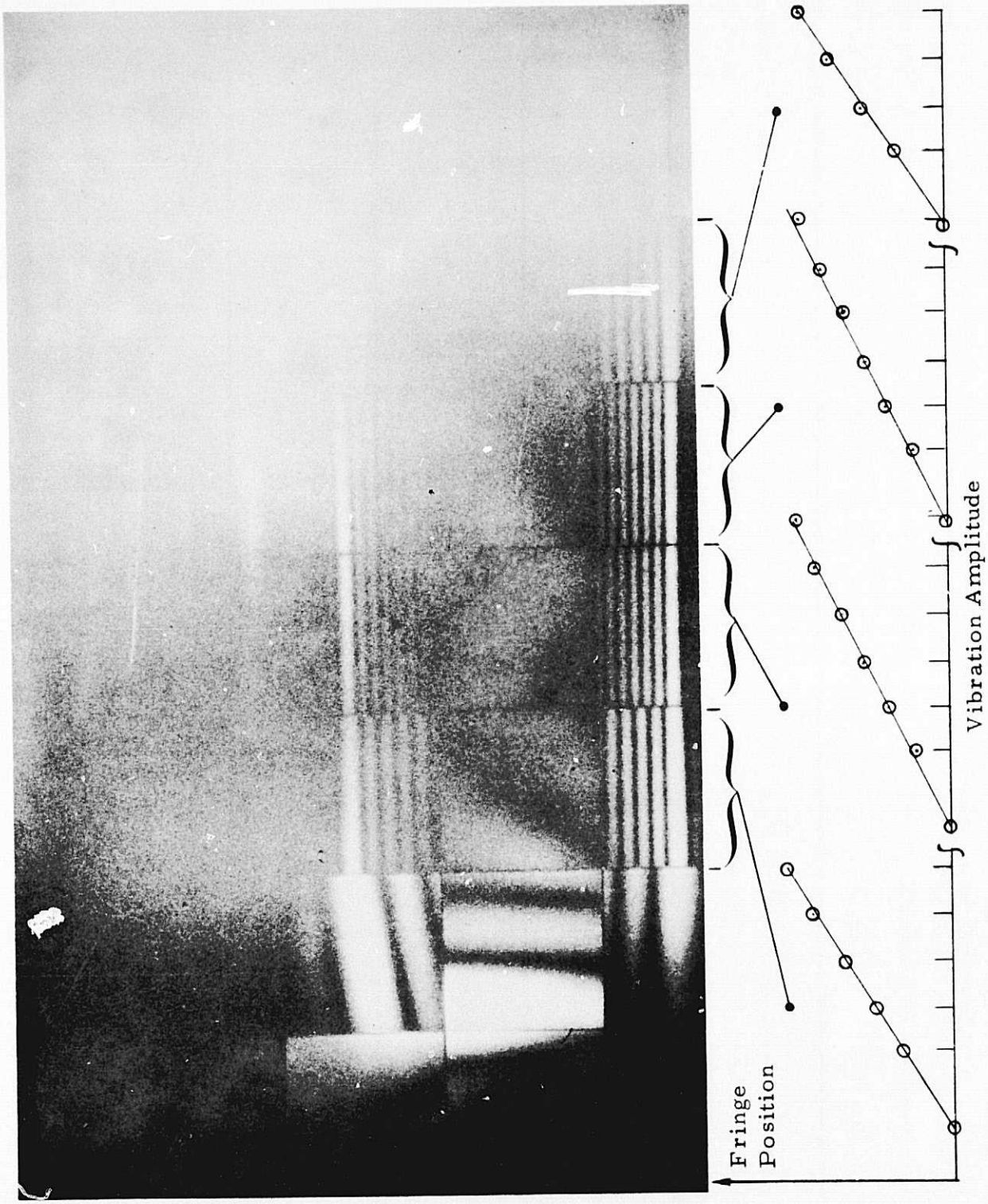

Figure 8. Time-Averaged Hologram of Tiled Panel, 160 Hz.

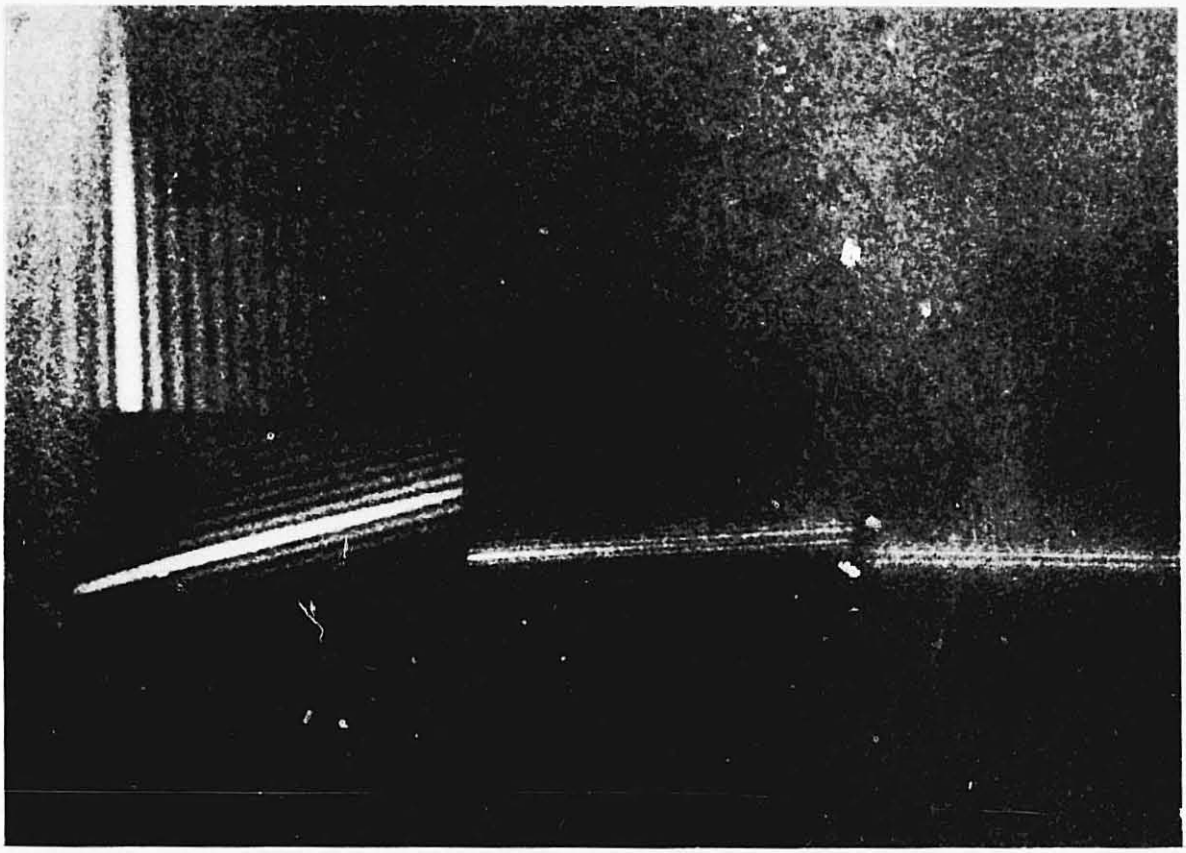

Close-up

Overall Fringe Pattern

Node Pattern

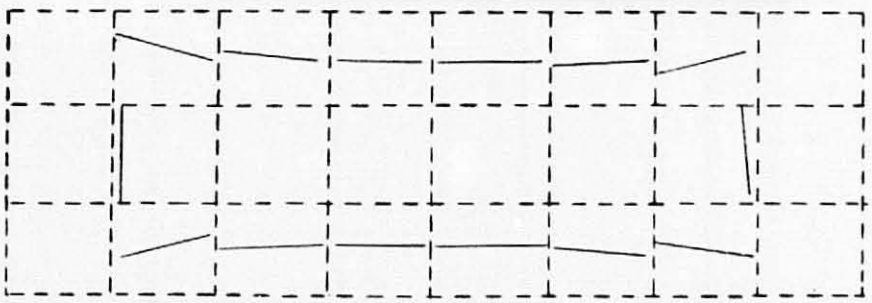

Figure 9. Time-Averaged Holograms of Tiled Panel, 122 Hz.

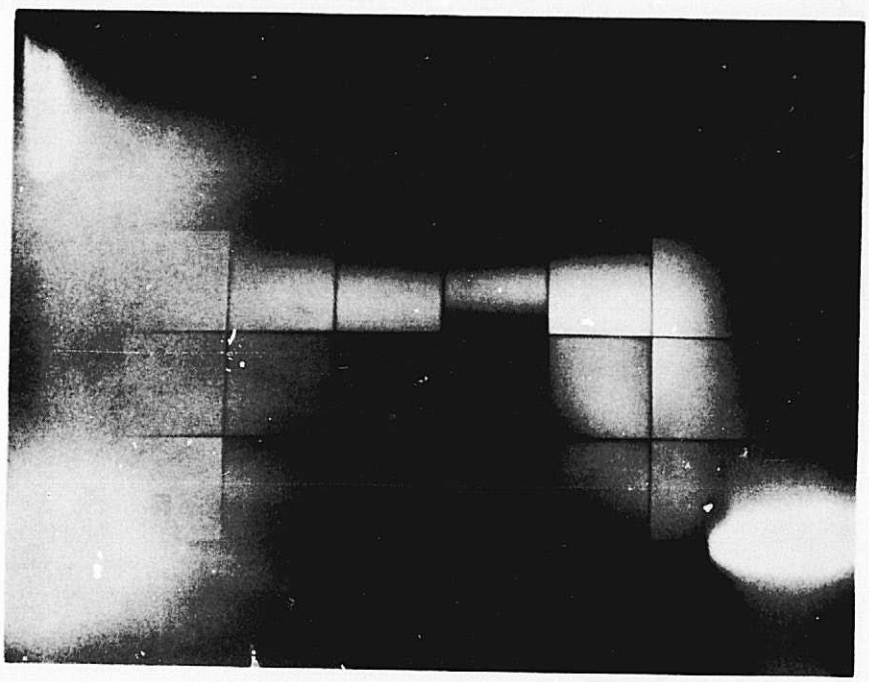

Figure 10. Time-Averaged Hologram of Mode at 777 Hz.

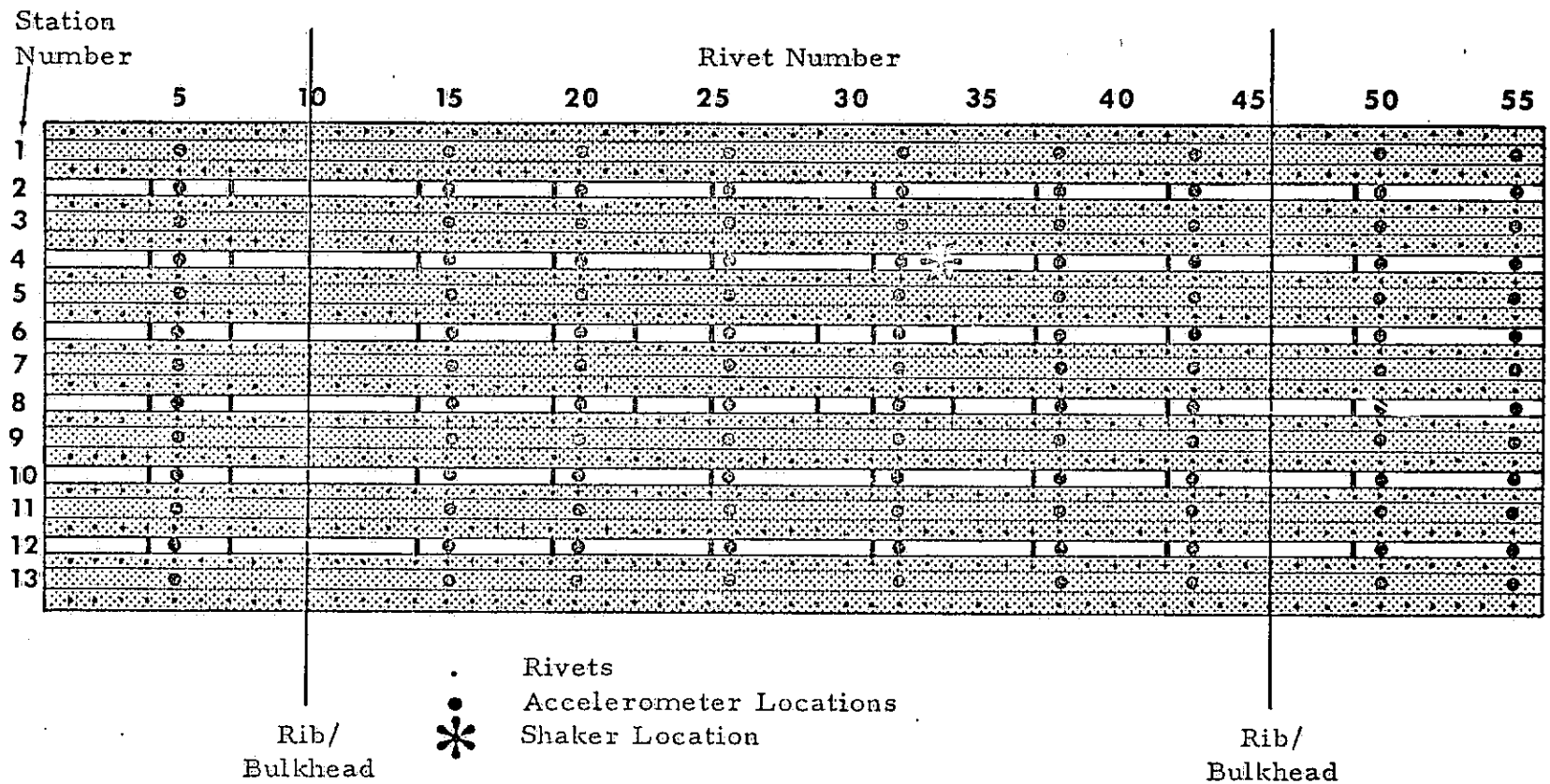

Figure 11. Accelerometer and Shaker Positions on Skin-Stringer Panel.

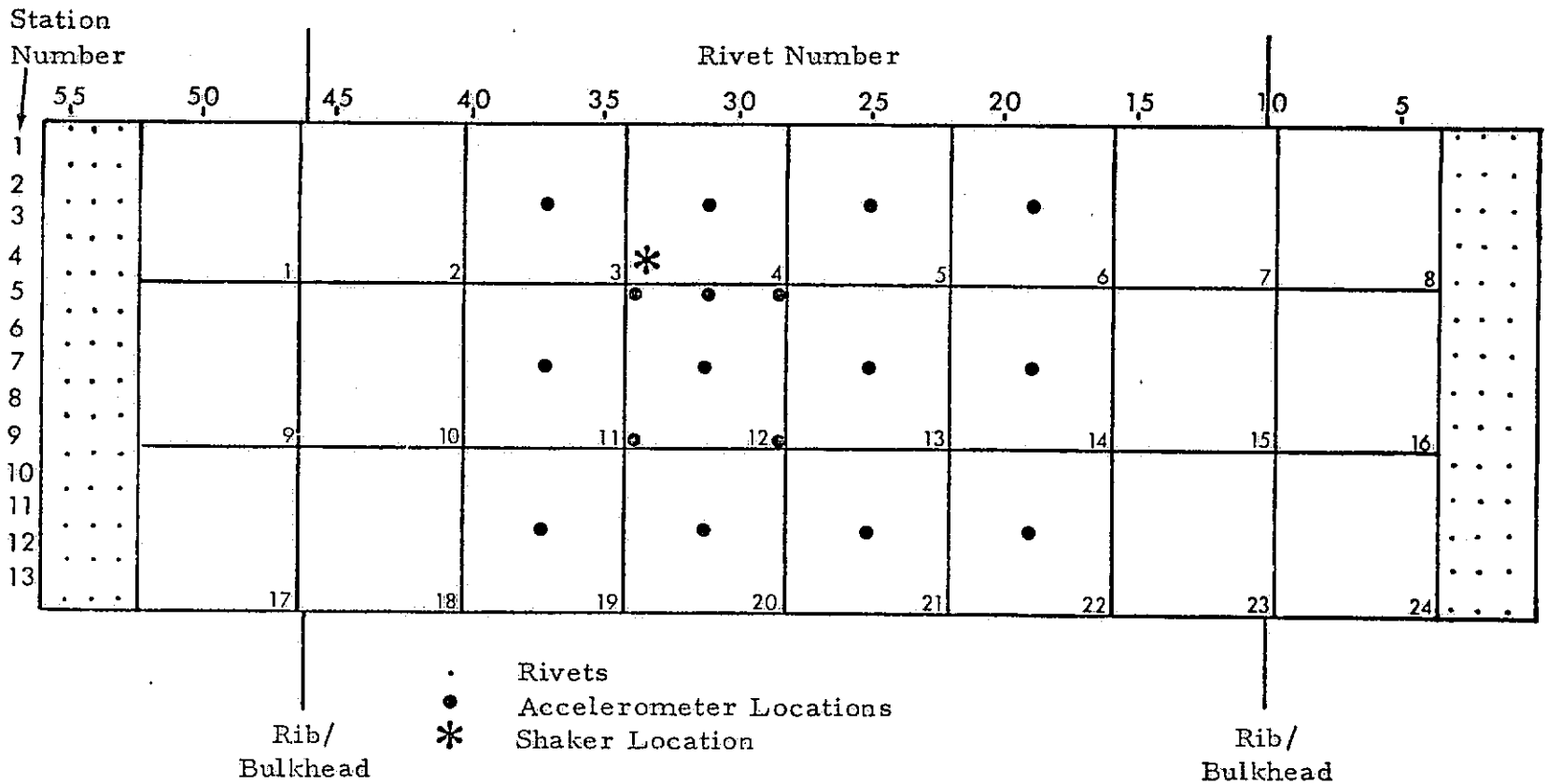

Figure 12. Accelerometer Positions on Thermal Tiles.

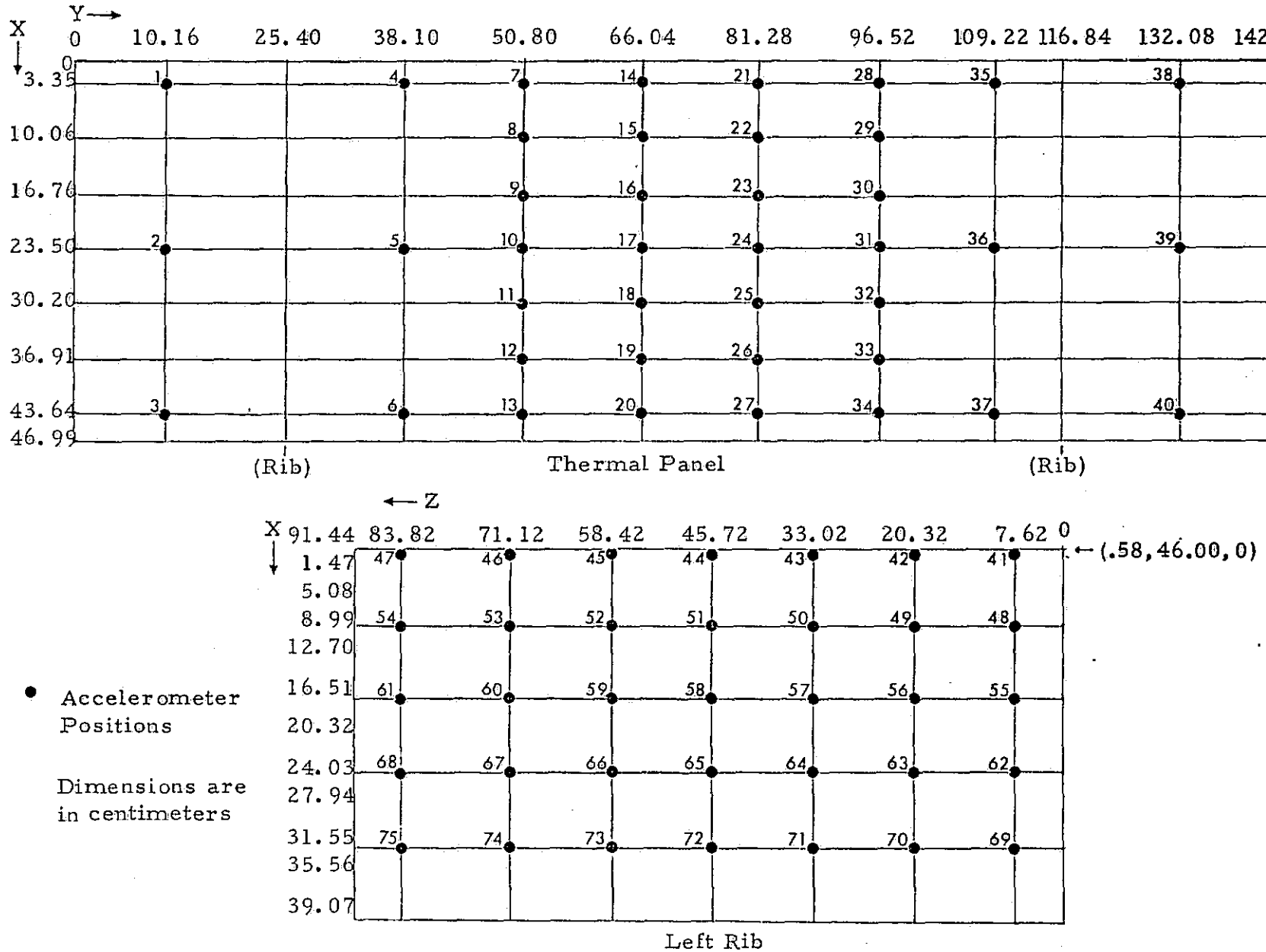

Figure 13. Skin-Stringer Panel and Left Rib.

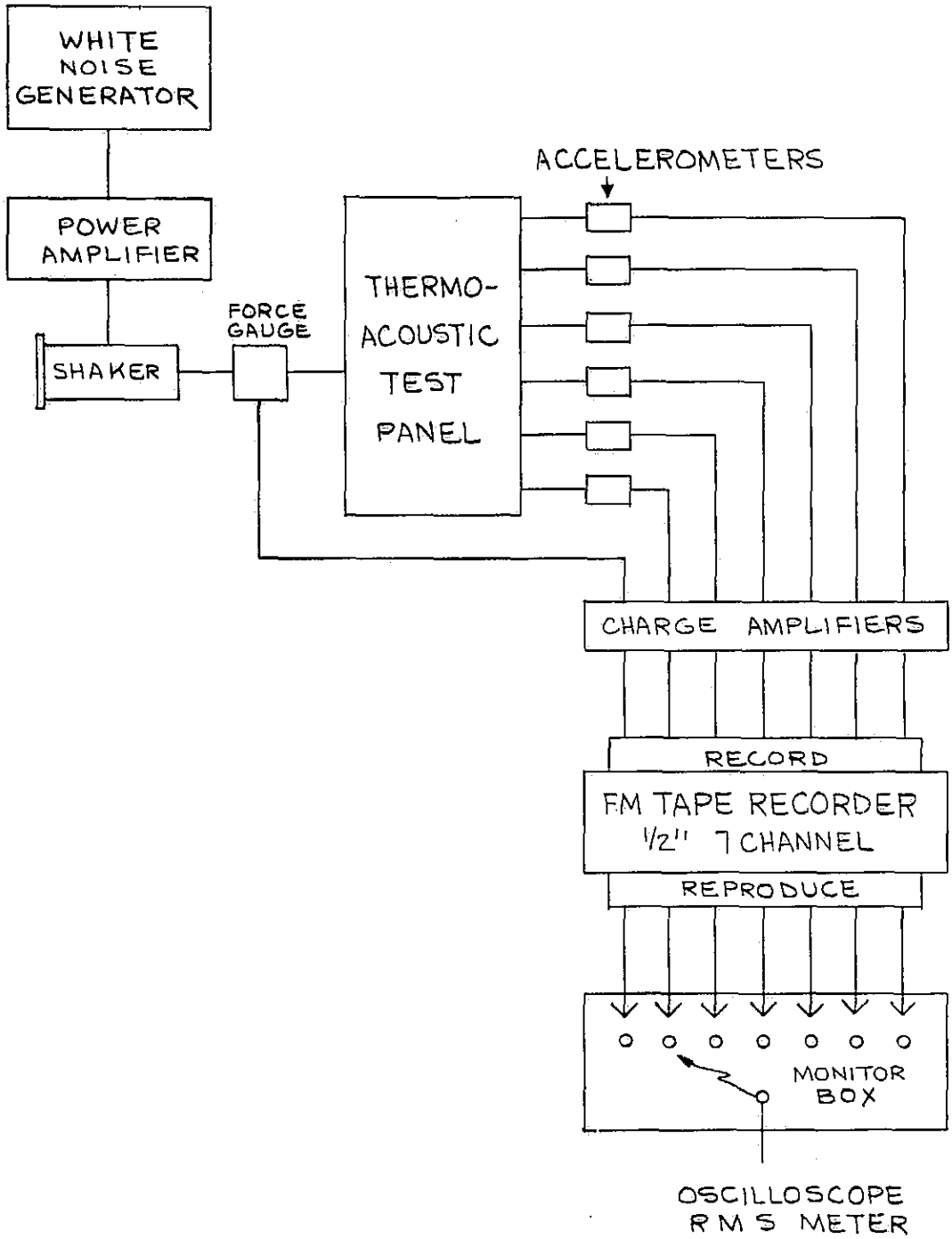

Figure 14. Block Diagram of System Instrumentation.

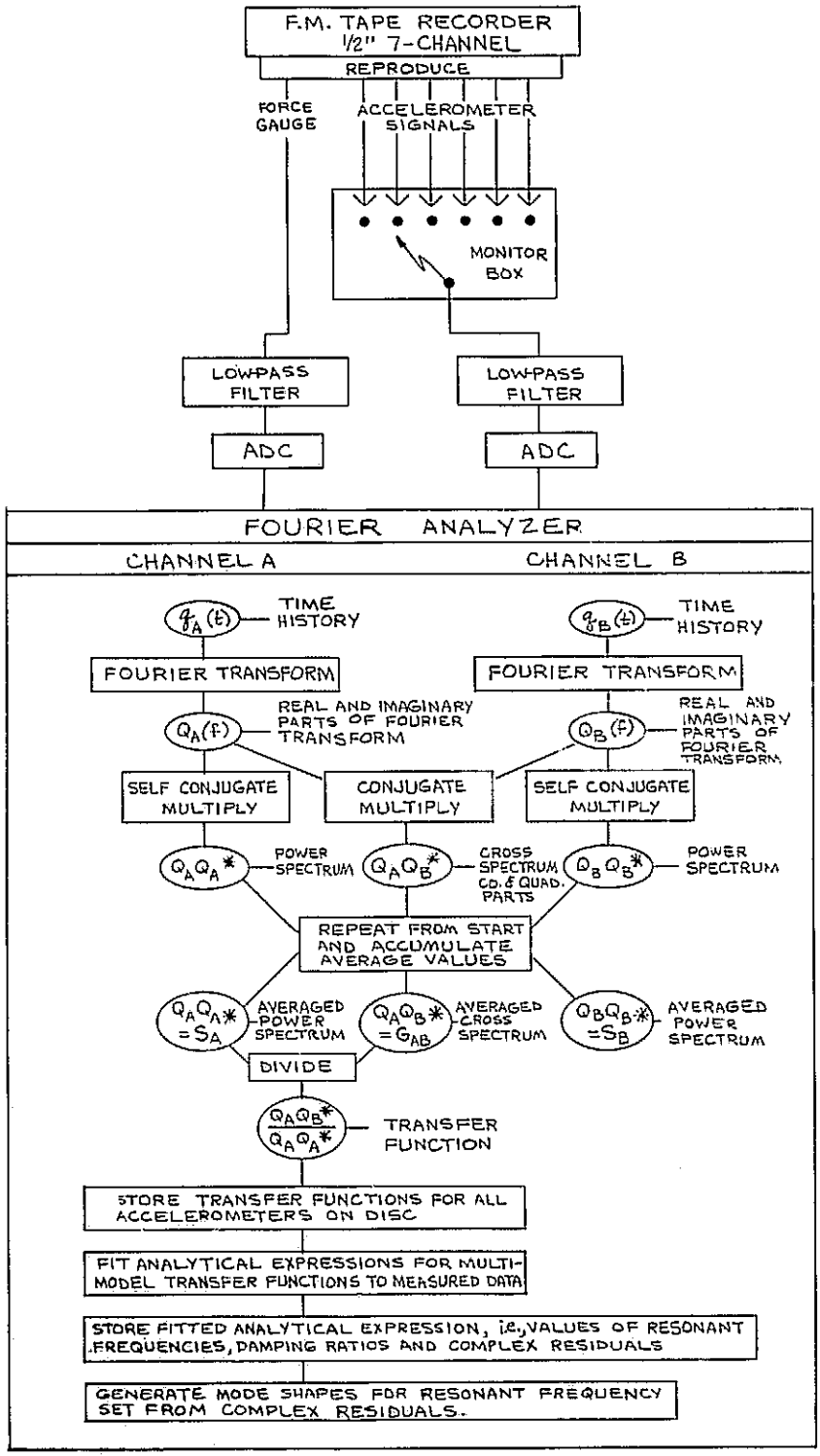

Figure 15. Calculation and Storage of Transfer Functions.

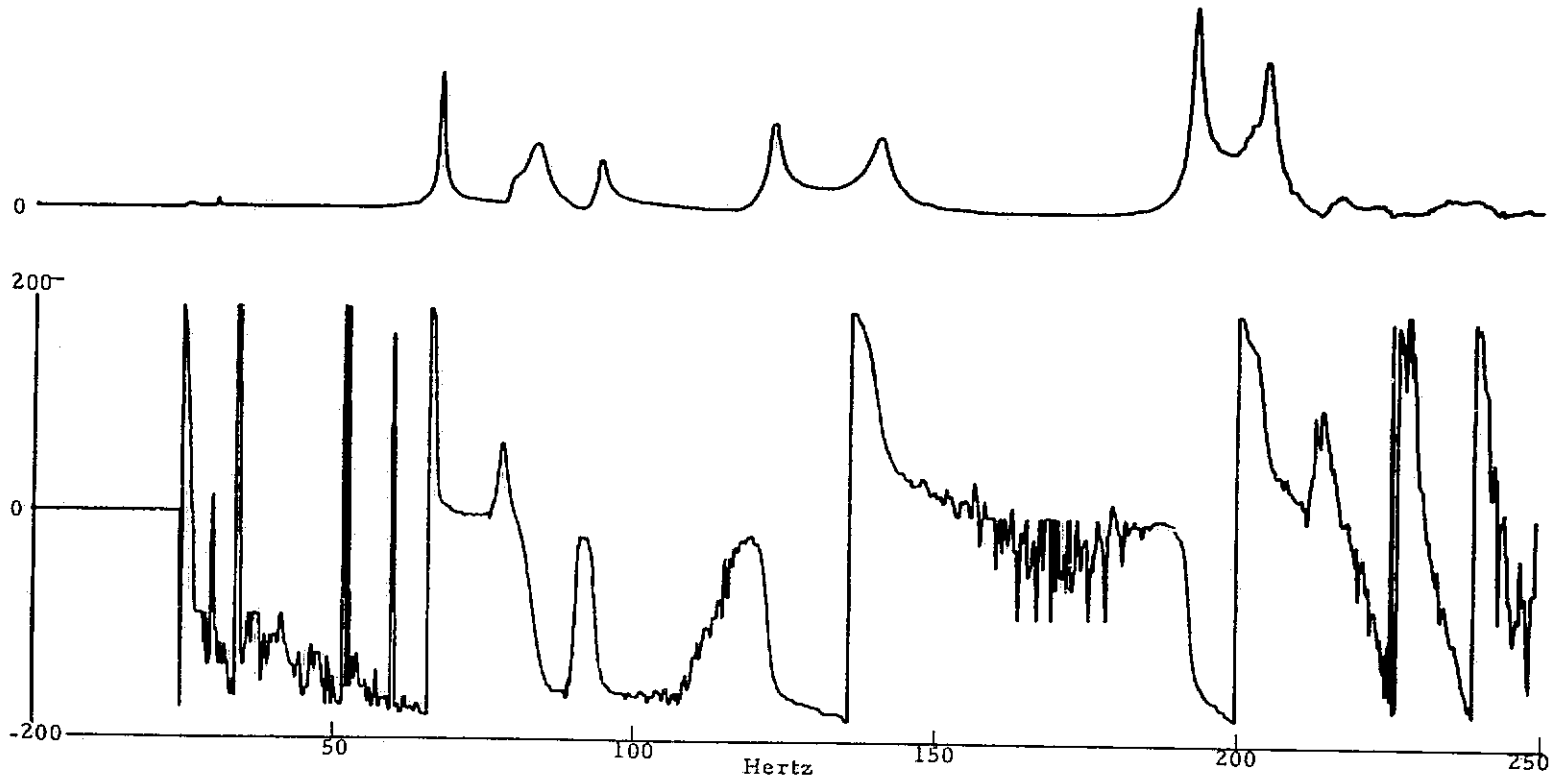

Figure 16. Typical Transfer Function on Skin-Stringer Panel (Ref. Figure 13, Position 6).

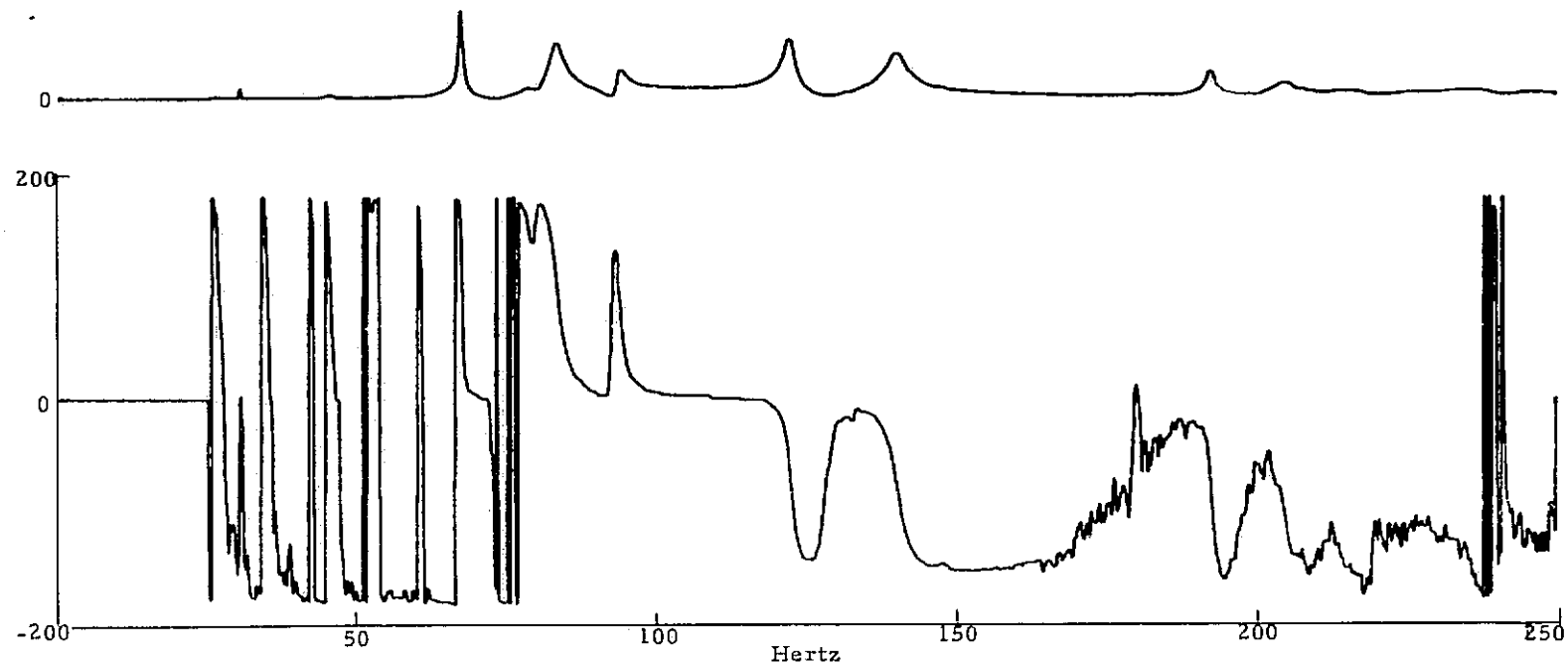

Figure 17. Typical Transfer Function on Skin-Stringer Panel (Ref. Figure 13, Position 14).

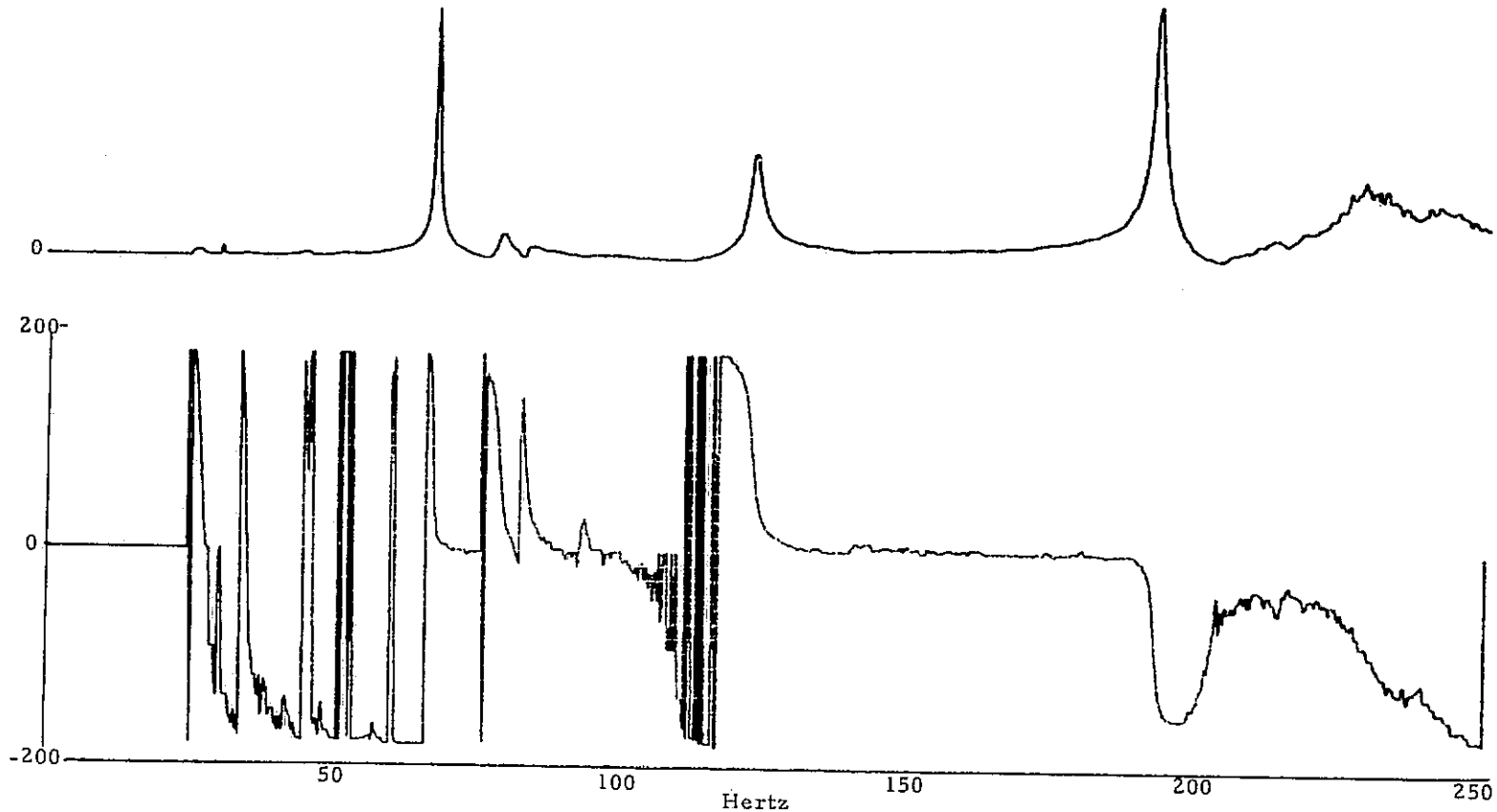

Figure 18. Typical Transfer Function on Skin-Stringer Panel (Ref. Figure 13, Position 10).

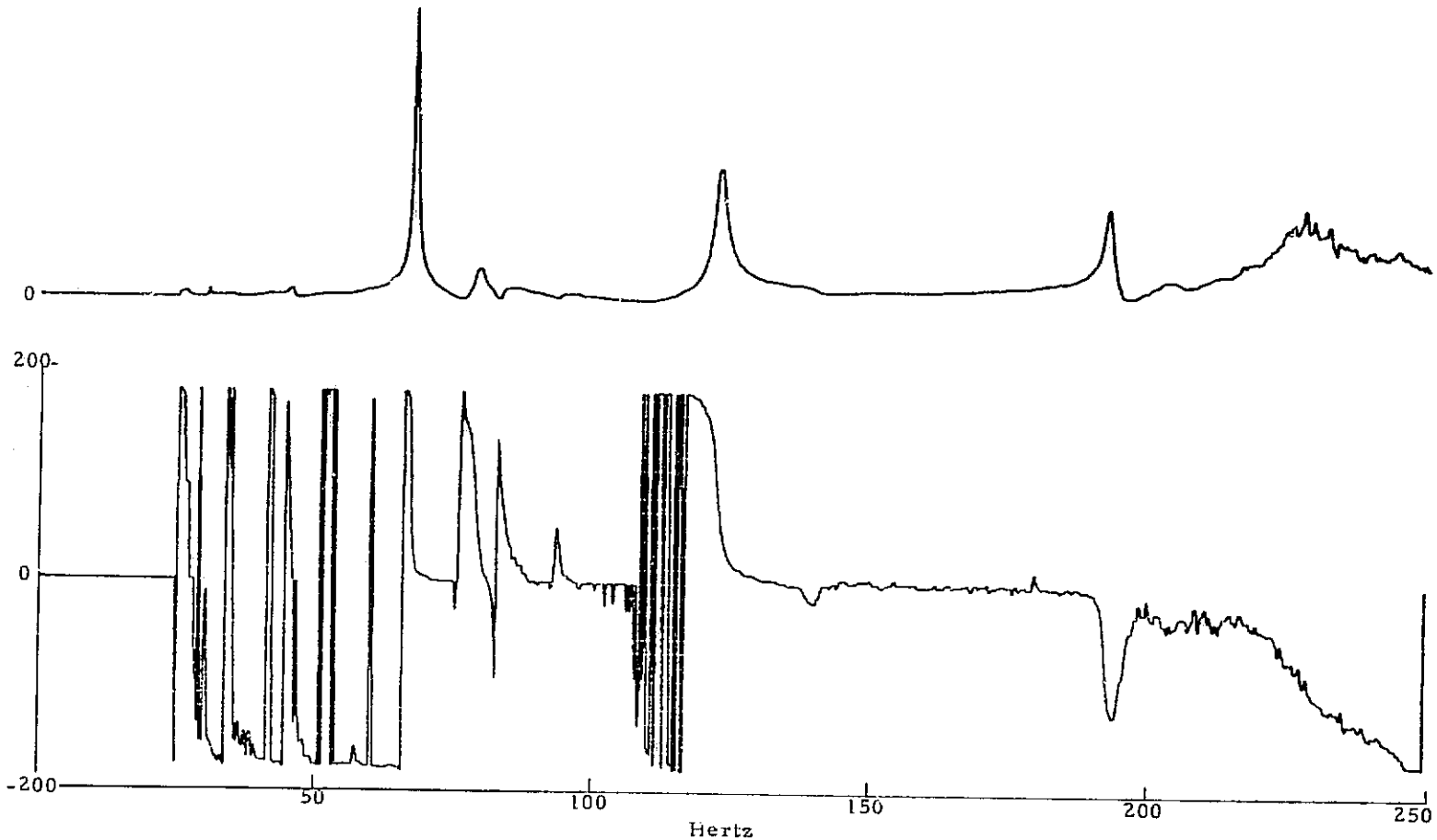

Figure 19. Typical Transfer Function on Skin-Stringer Panel (Ref. Figure 13, Position 17).

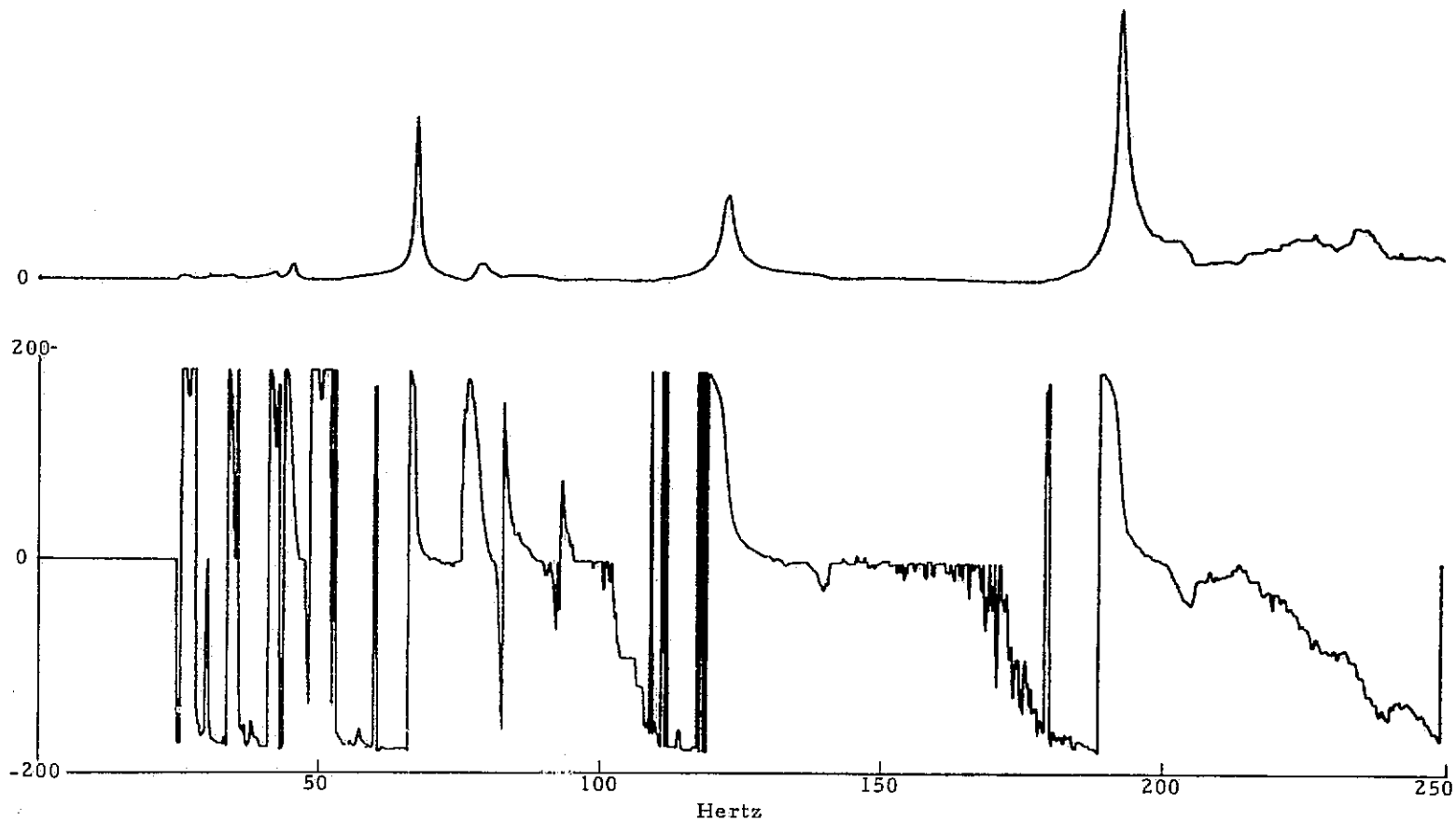

Figure 20. Typical Transfer Function on Skin-Stringer Panel (Ref. Figure 13, Position 31).

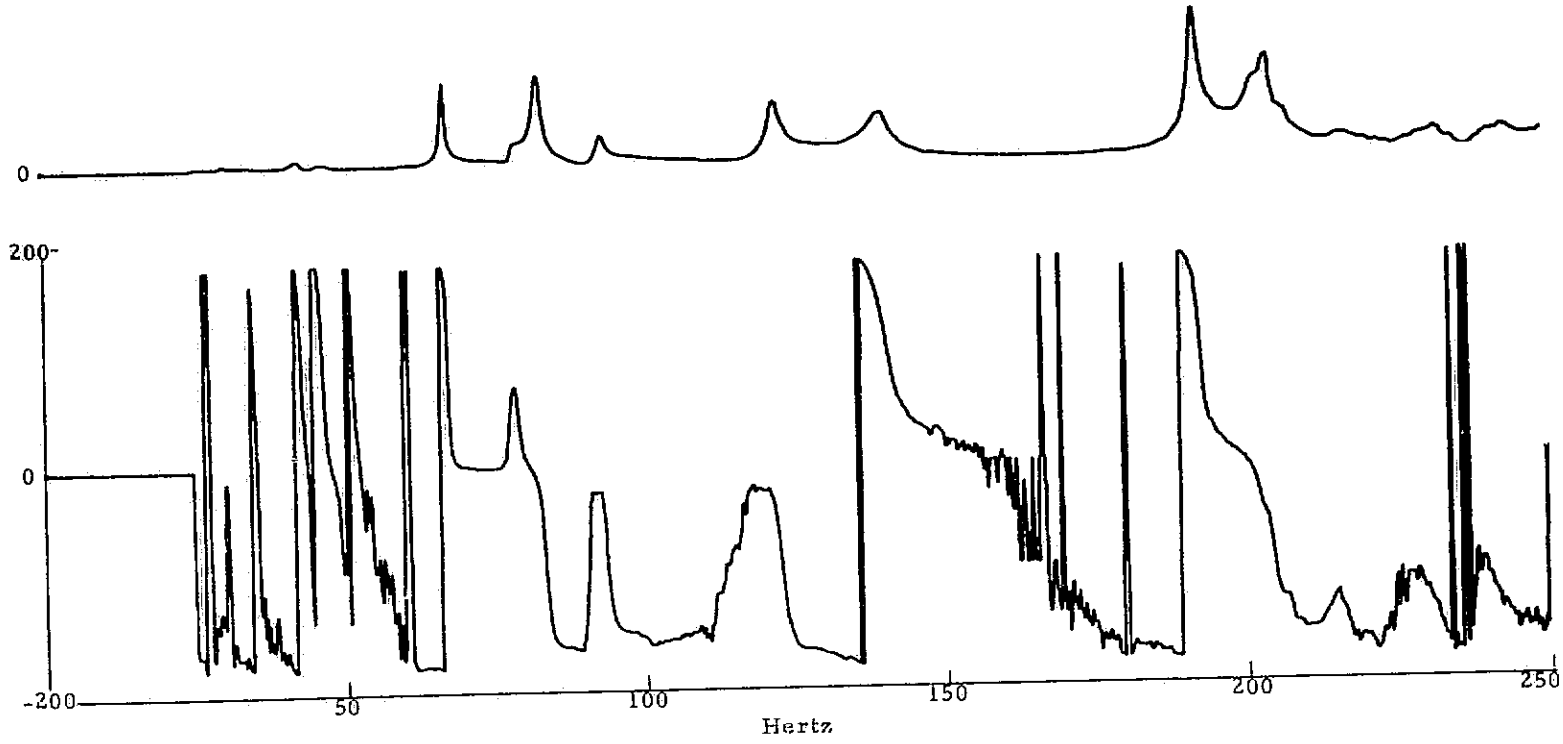

Figure 21. Typical Transfer Function on Skin-Stringer Panel (Ref. Figure 13, Position 37).

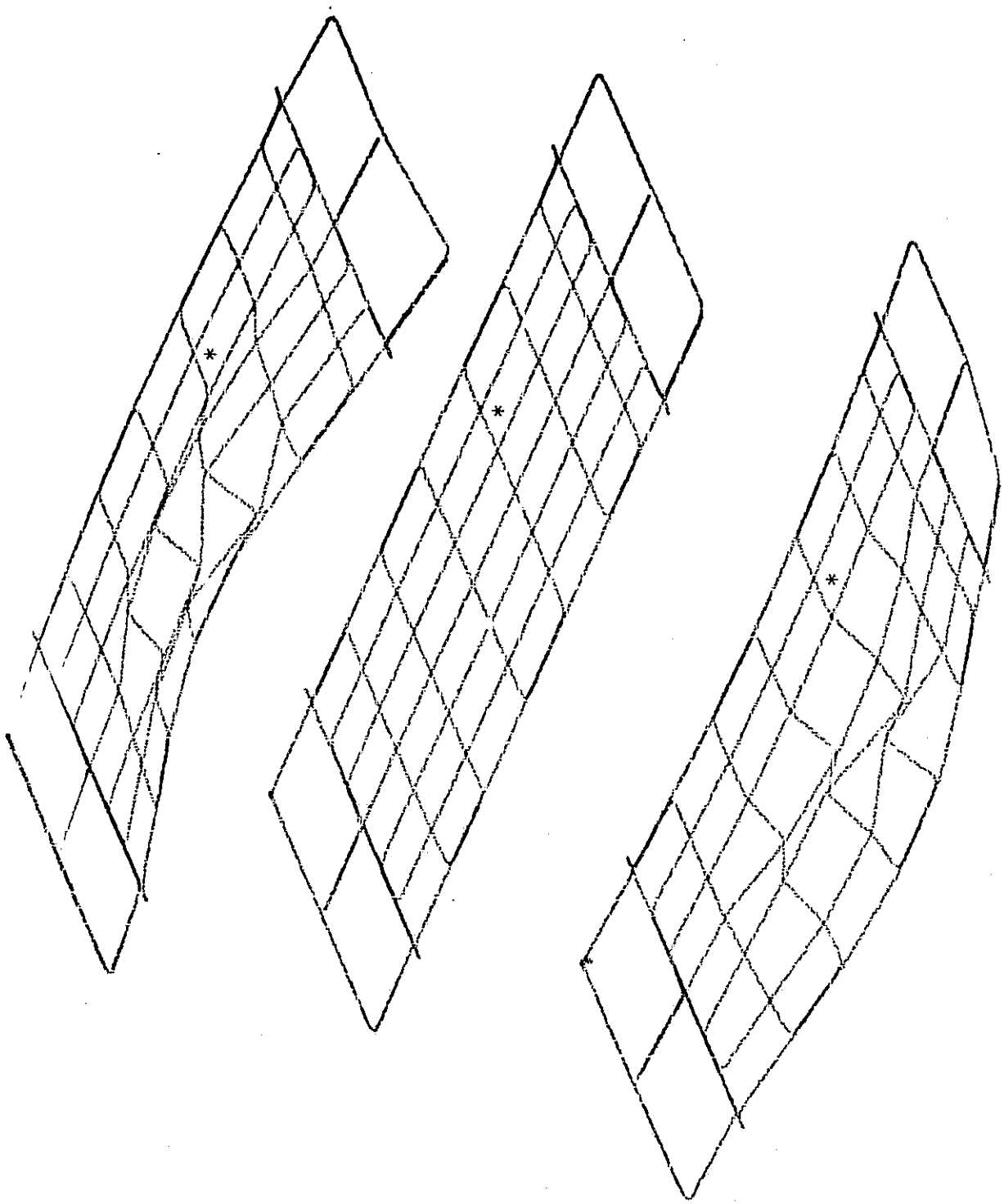

Figure 22. Typical Isometric Plots of Skin-Stringer Panel Deformation, 67Hz.

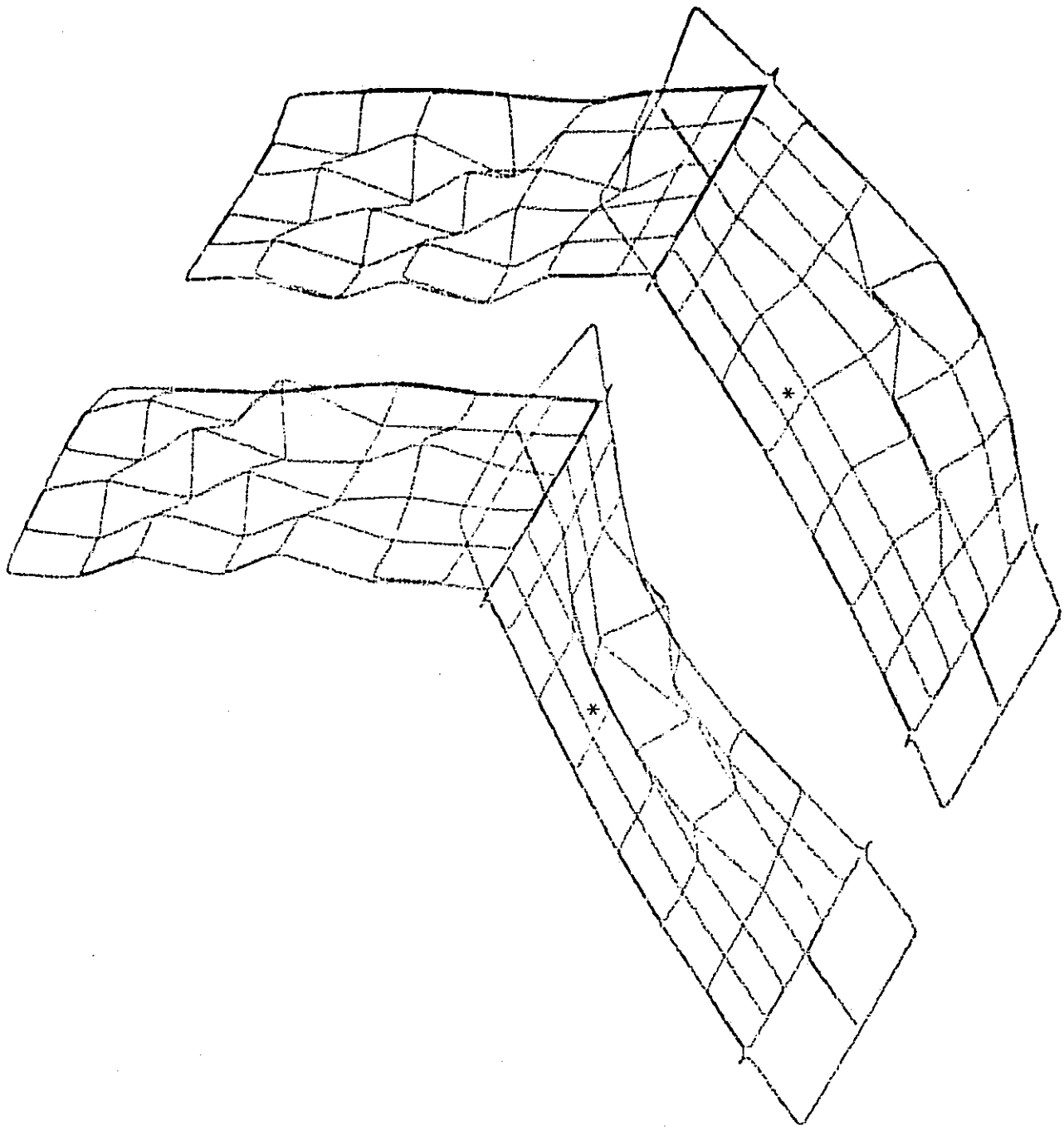

Figure 23. Typical Isometric Plots of Skin Stringer and Rib Panel Deformations, 67Hz.

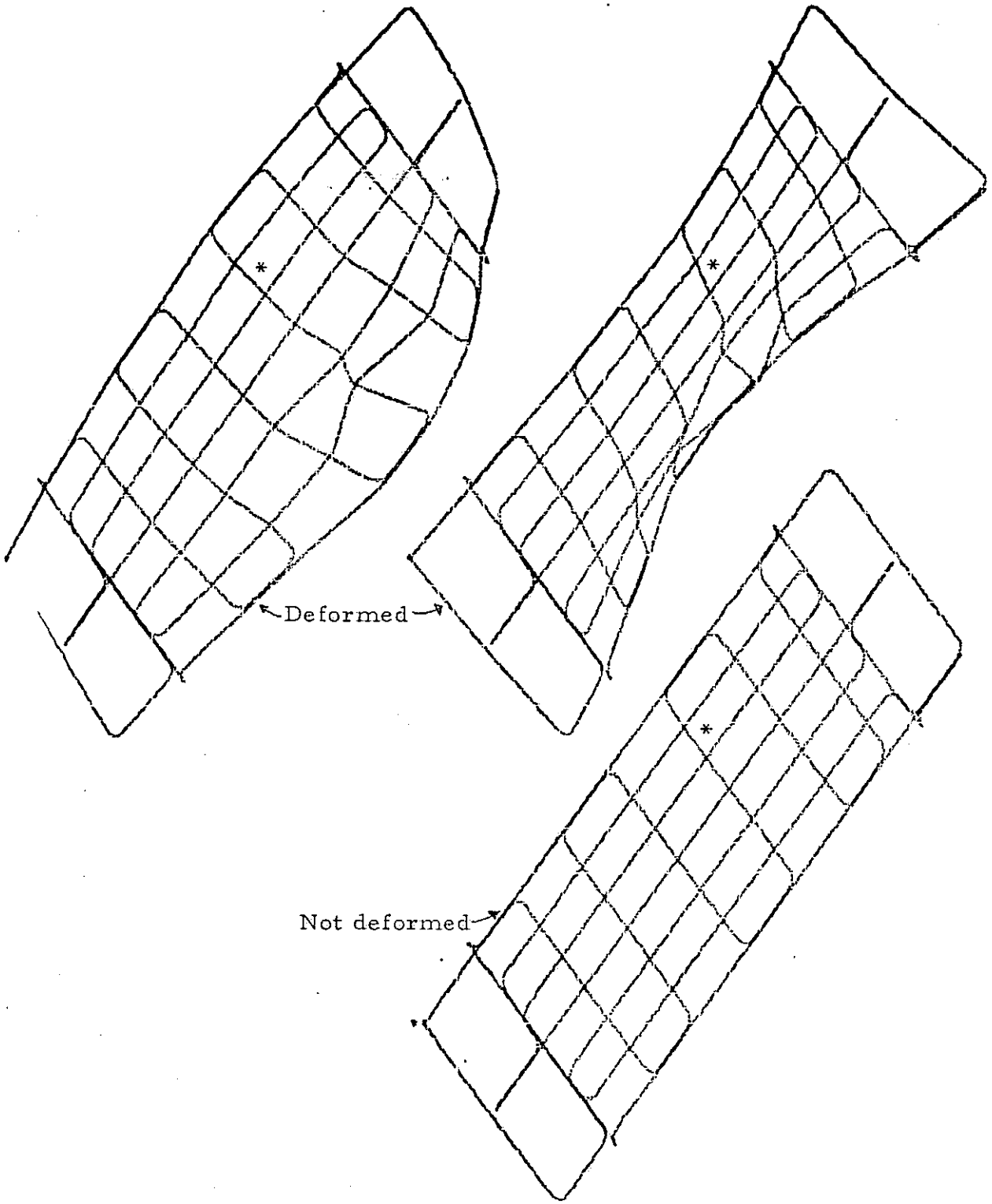

Figure 24. Typical Isometric Plots of Skin-Stringer Panel Deformation, 83 Hz.

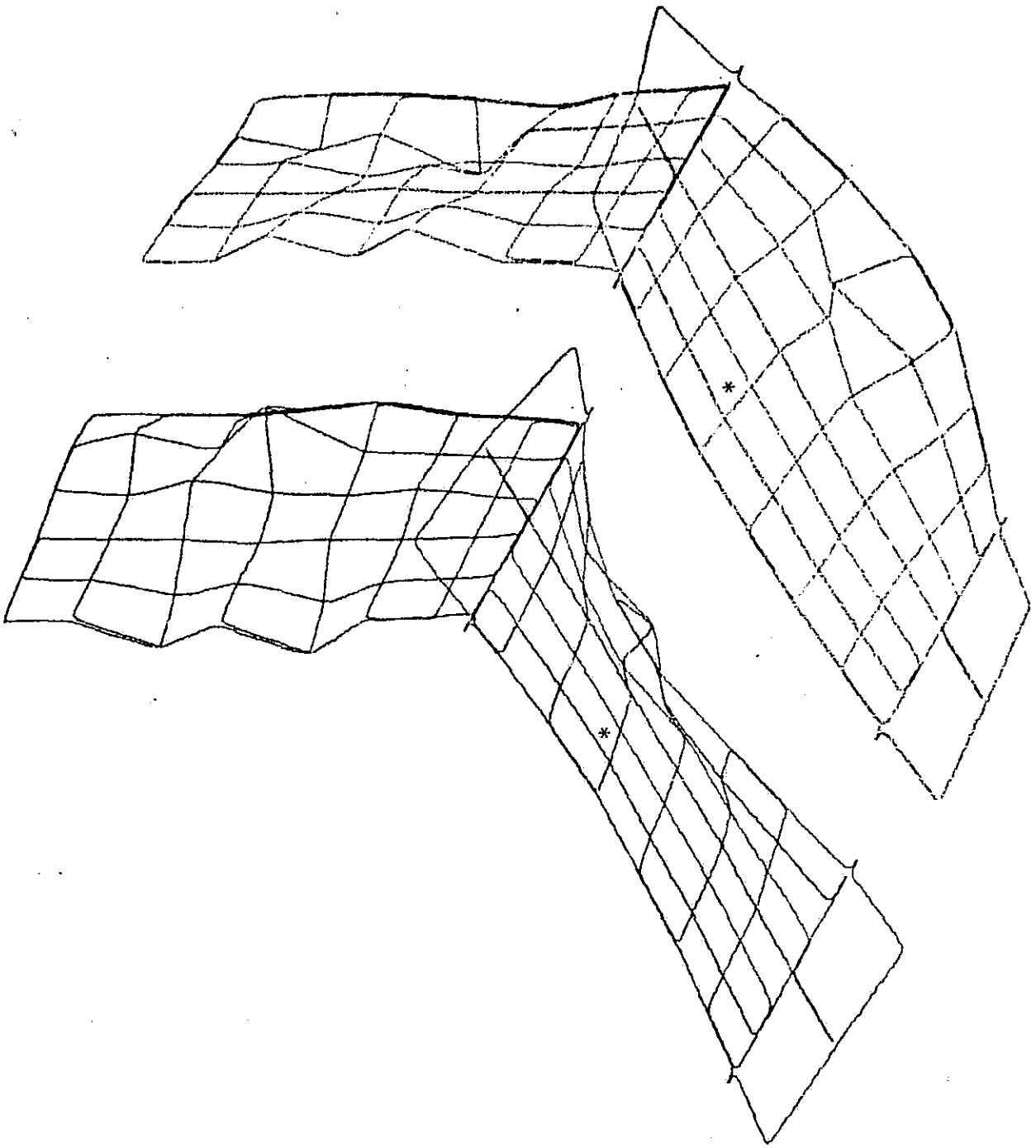

Figure 25. Typical Isometric Plots of Skin Stringer and Rib Panel Deformations, 83 Hz.

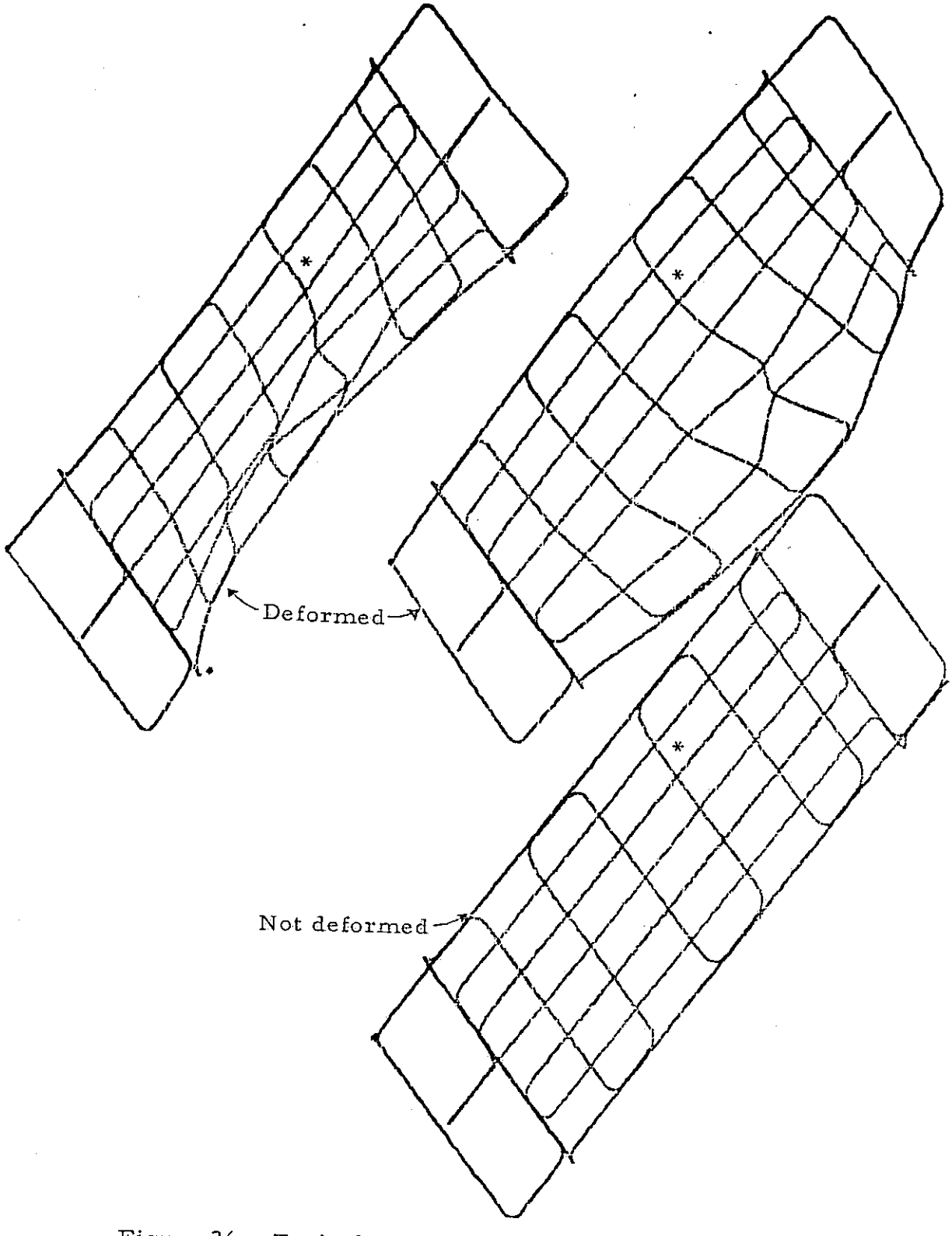

Figure 26. Typical Isometric Plots of Skin-Stringer Panel Deformation, 93 Hz.

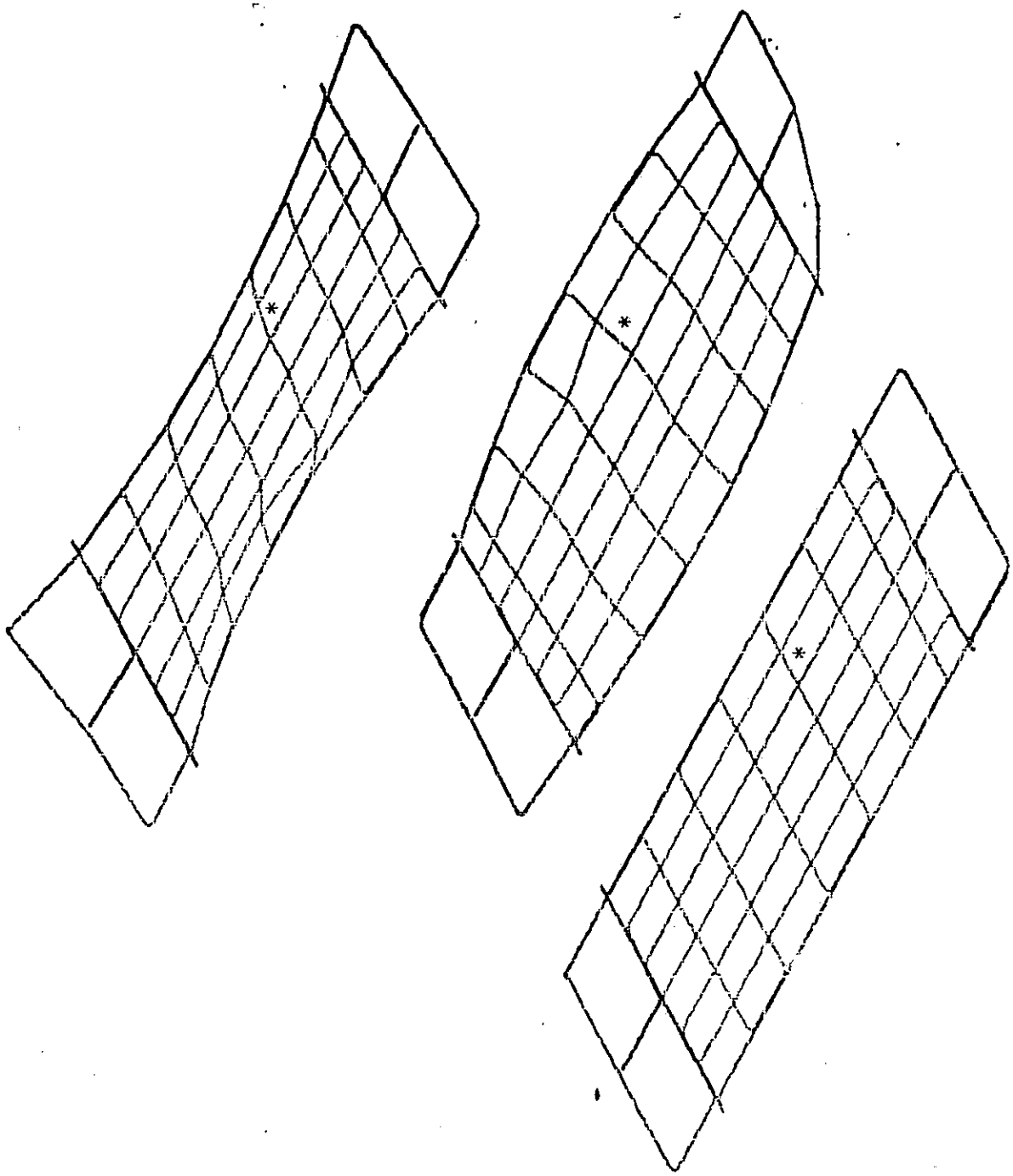

Figure 27. Typical Isometric Plots of Skin-Stringer Panel Deformation, 103 Hz.

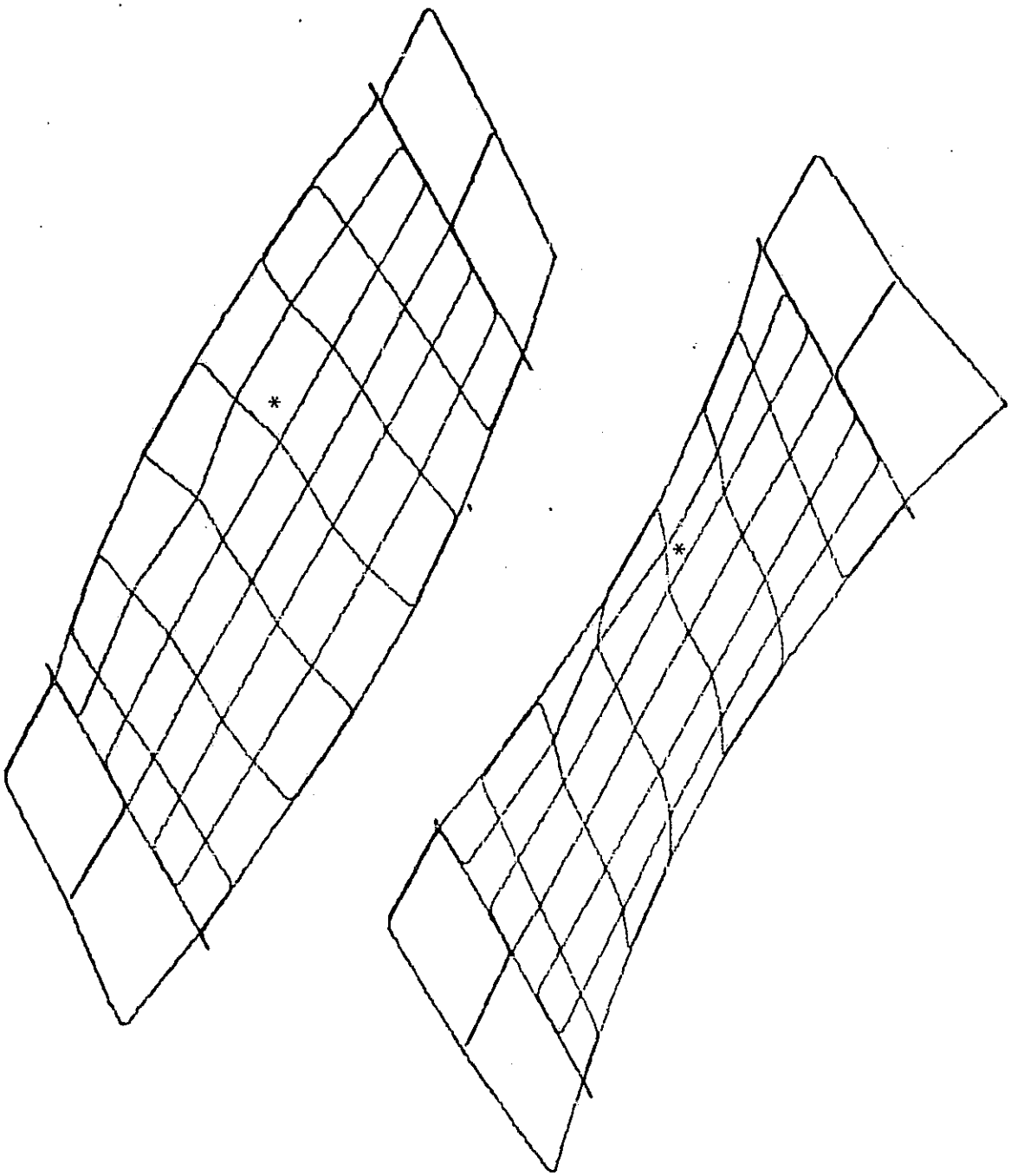

Figure 28. Typical Isometric Plots of Skin-Stringer Panel Deformation, 108 Hz.

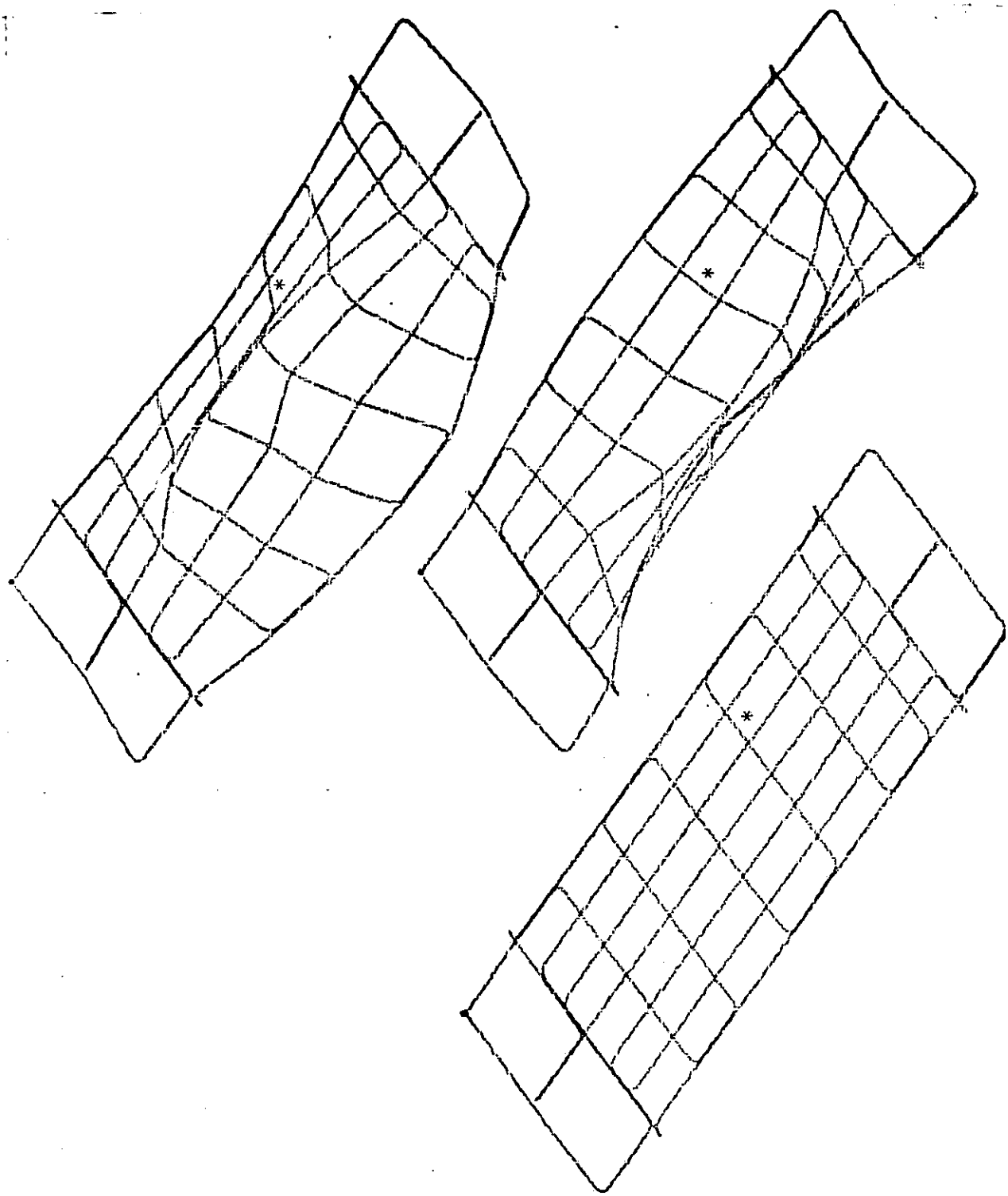

Figure 29. Typical Isometric Plots of Skin-Stringer Panel Deformation, 122 Hz.

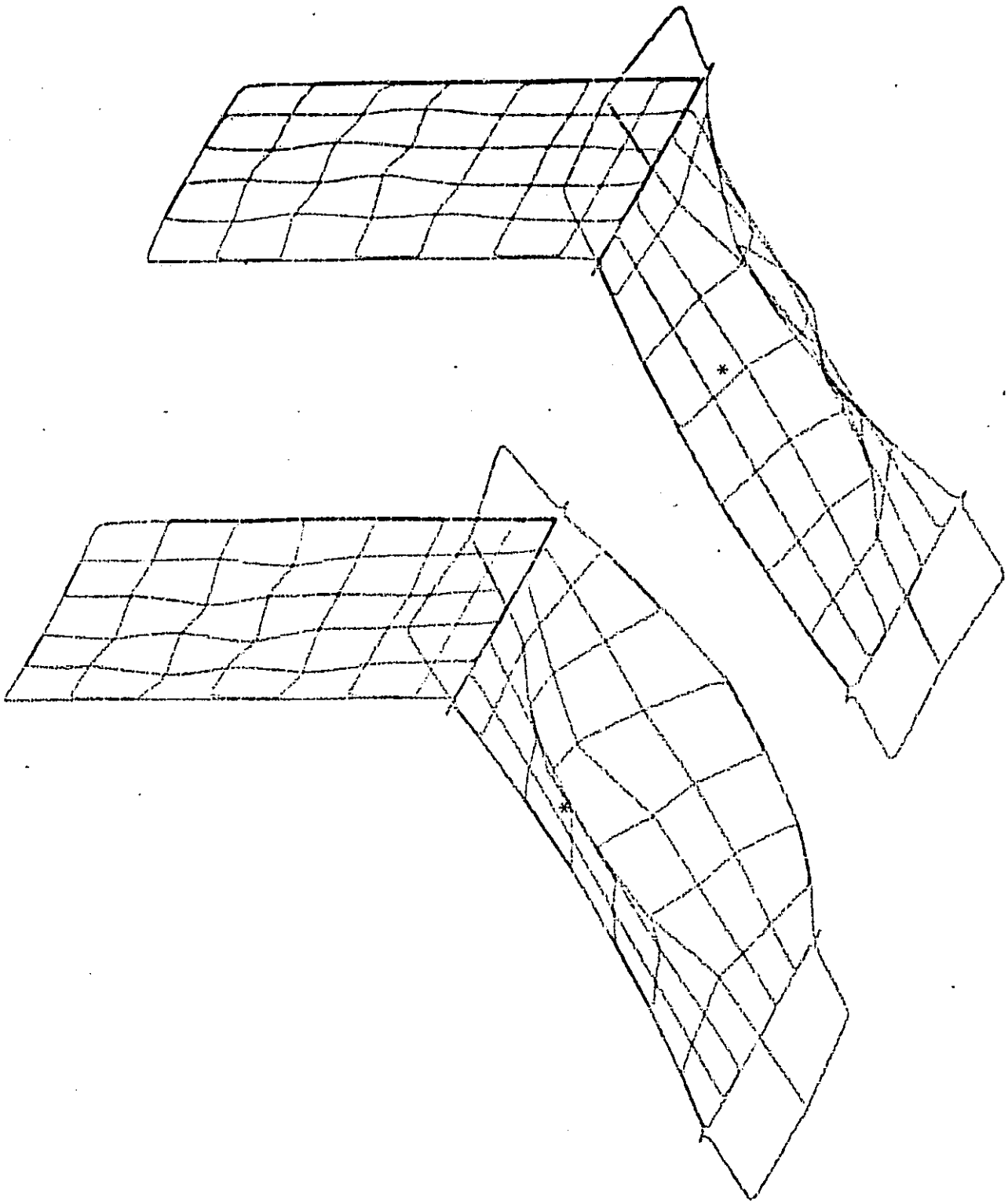

Figure 30. Typical Isometric Plots of Skin Stringer and Rib Panel Deformations, 122 Hz.

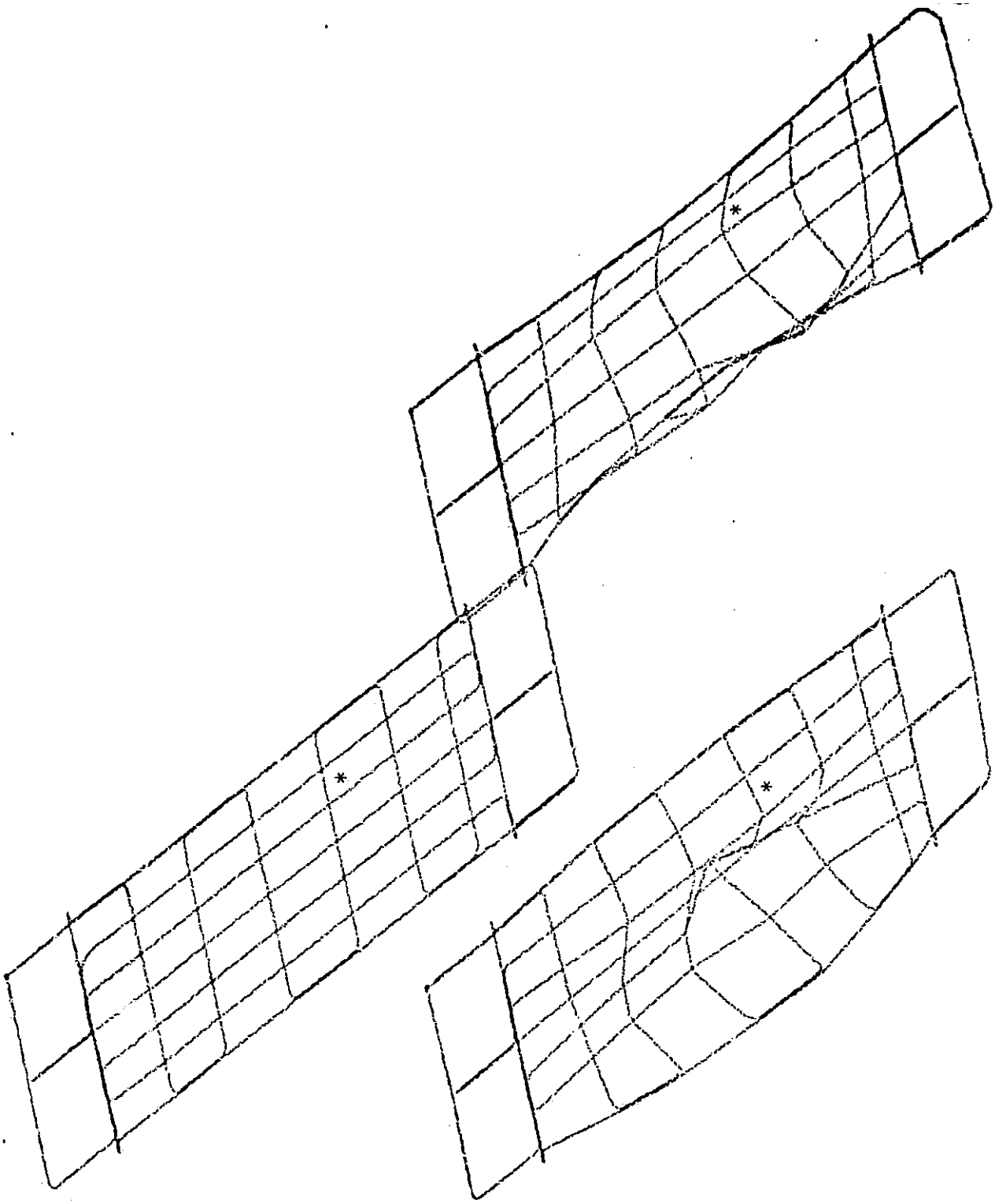

Figure 31. Typical Isometric Plots of Skin-Stringer Panel Deformation, 141 Hz.

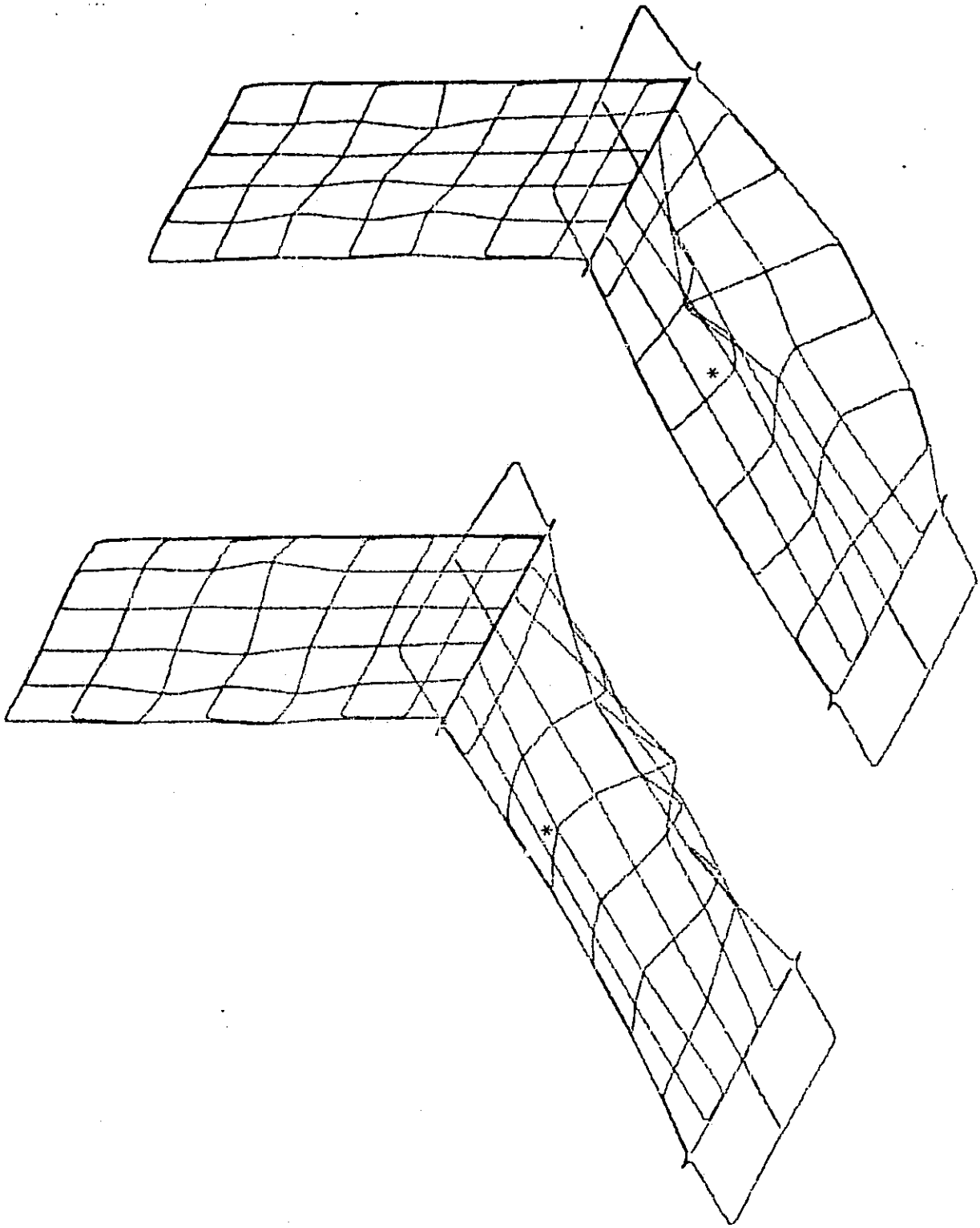

Figure 32. Typical Isometric Plots of Skin Stringer and Rib Panel Deformations, 141 Hz.

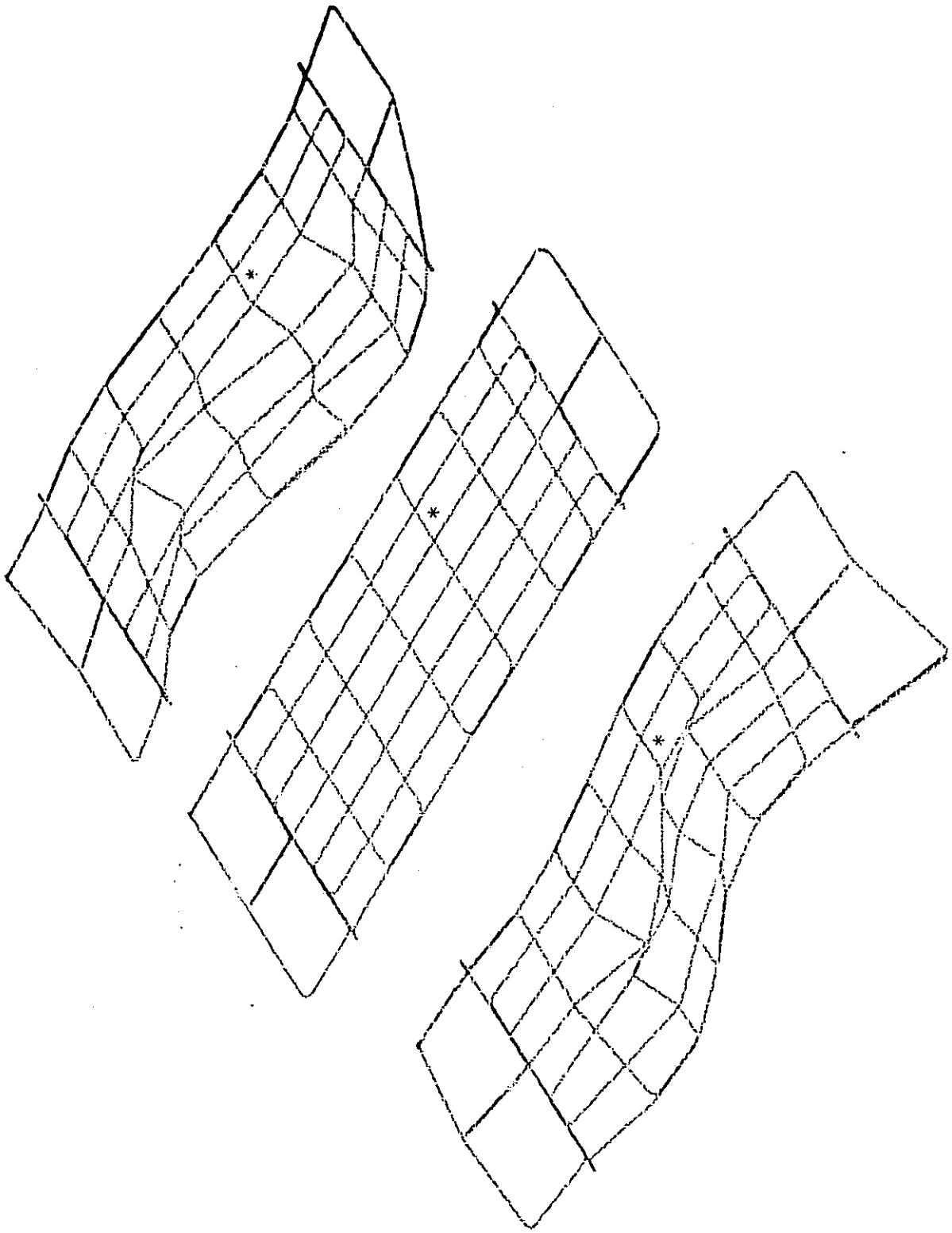

Figure 33. Typical Isometric Plots of Skin-Stringer Panel Deformation, 193 Hz.

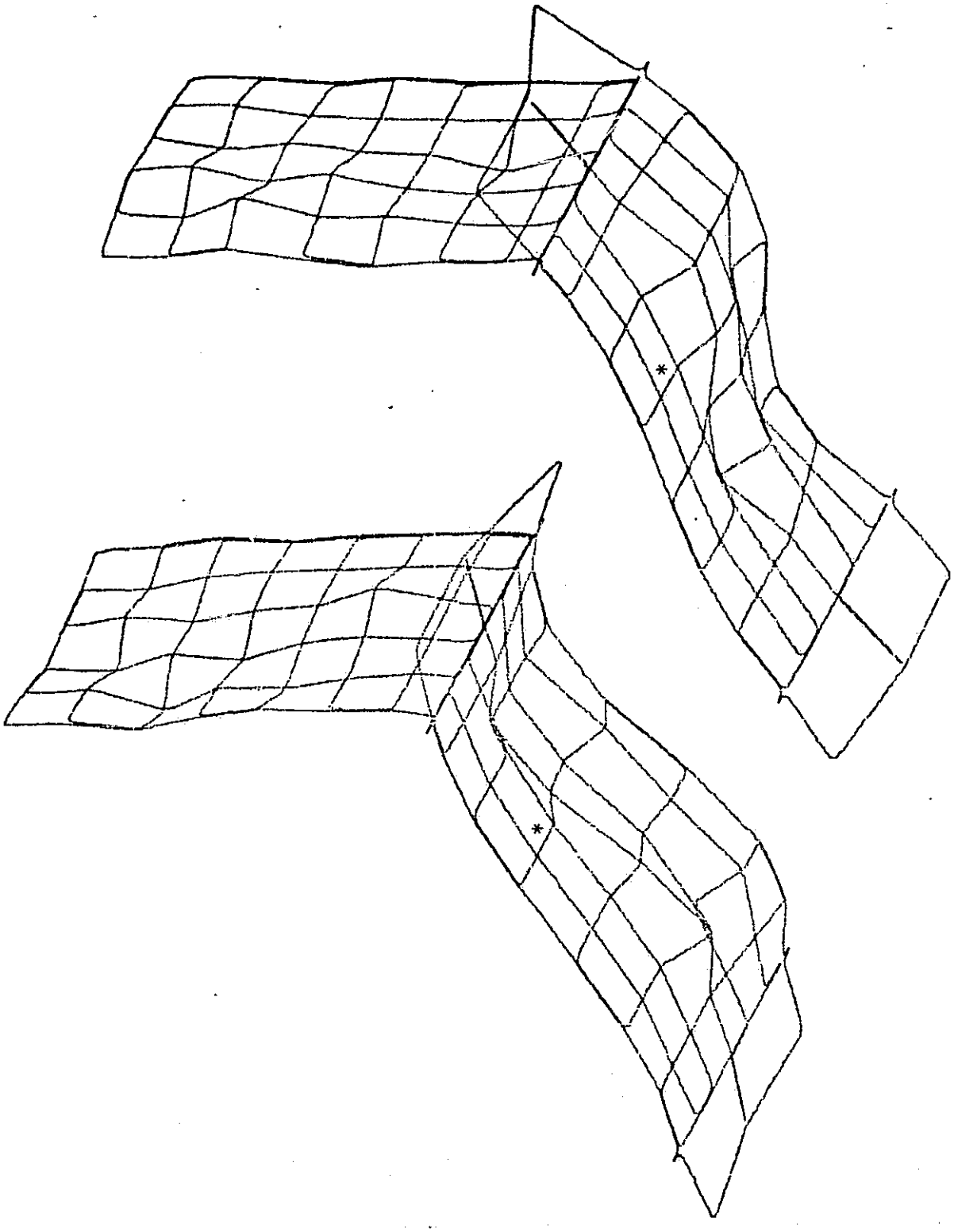

Figure 34. Typical Isometric Plots of Skin Stringer and Rib Panel Deformations, 193 Hz.

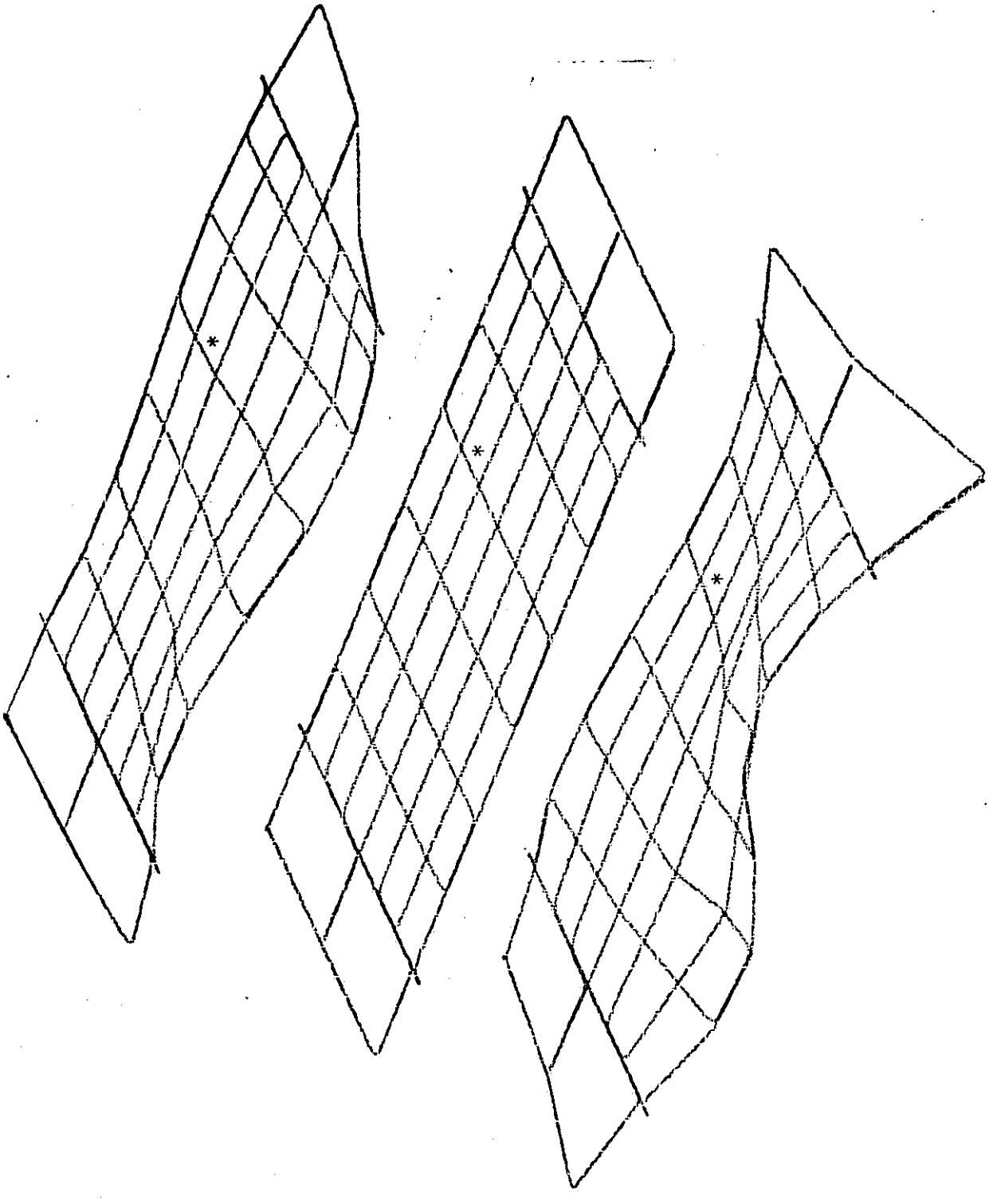

Figure 35. Typical Isometric Plots of Skin-Stringer Panel Deformation, 204 Hz.

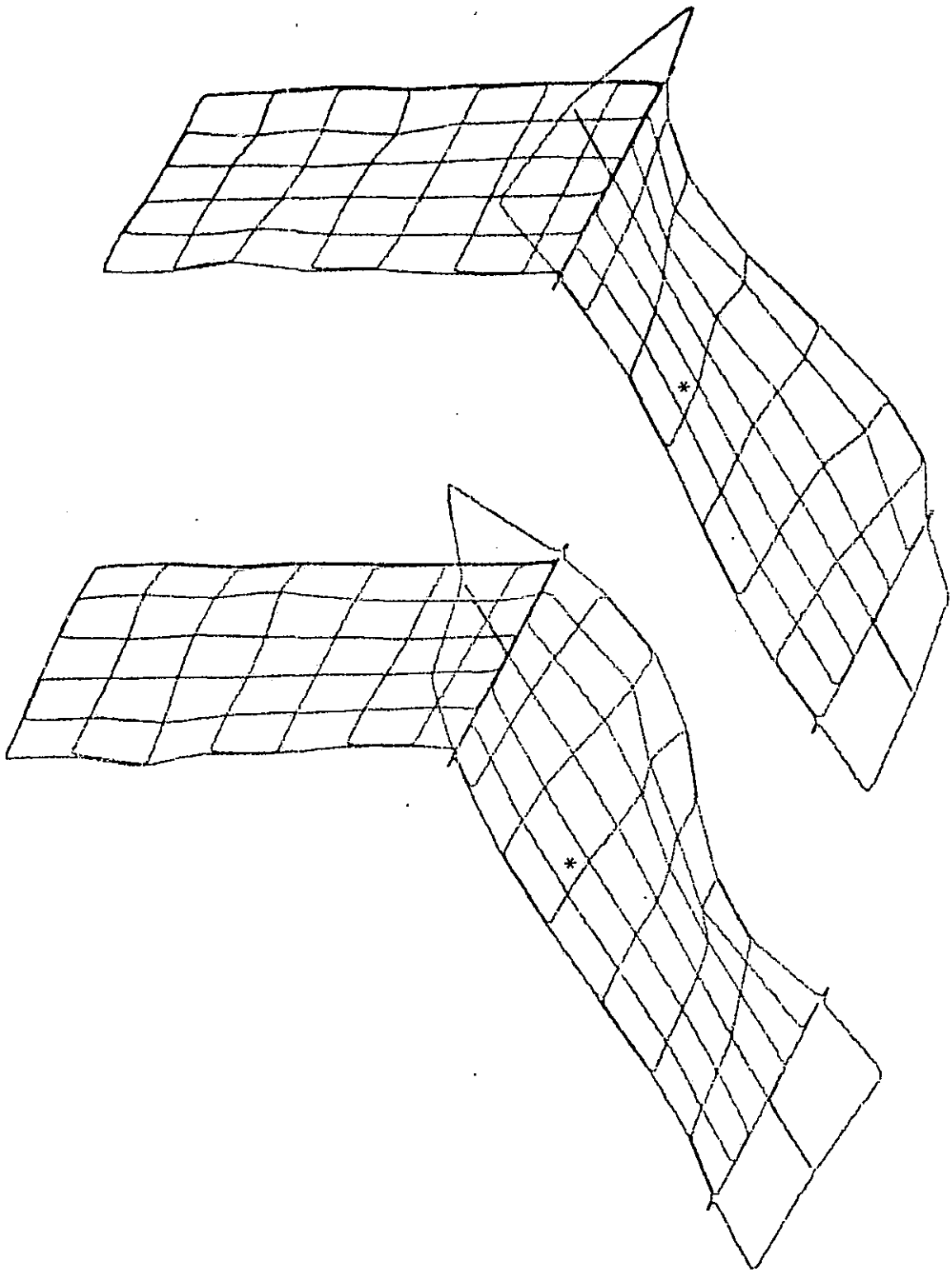

Figure 36. Typical Isometric Plots of Skin Stringer and Rib Panel Deformations, 204 Hz.

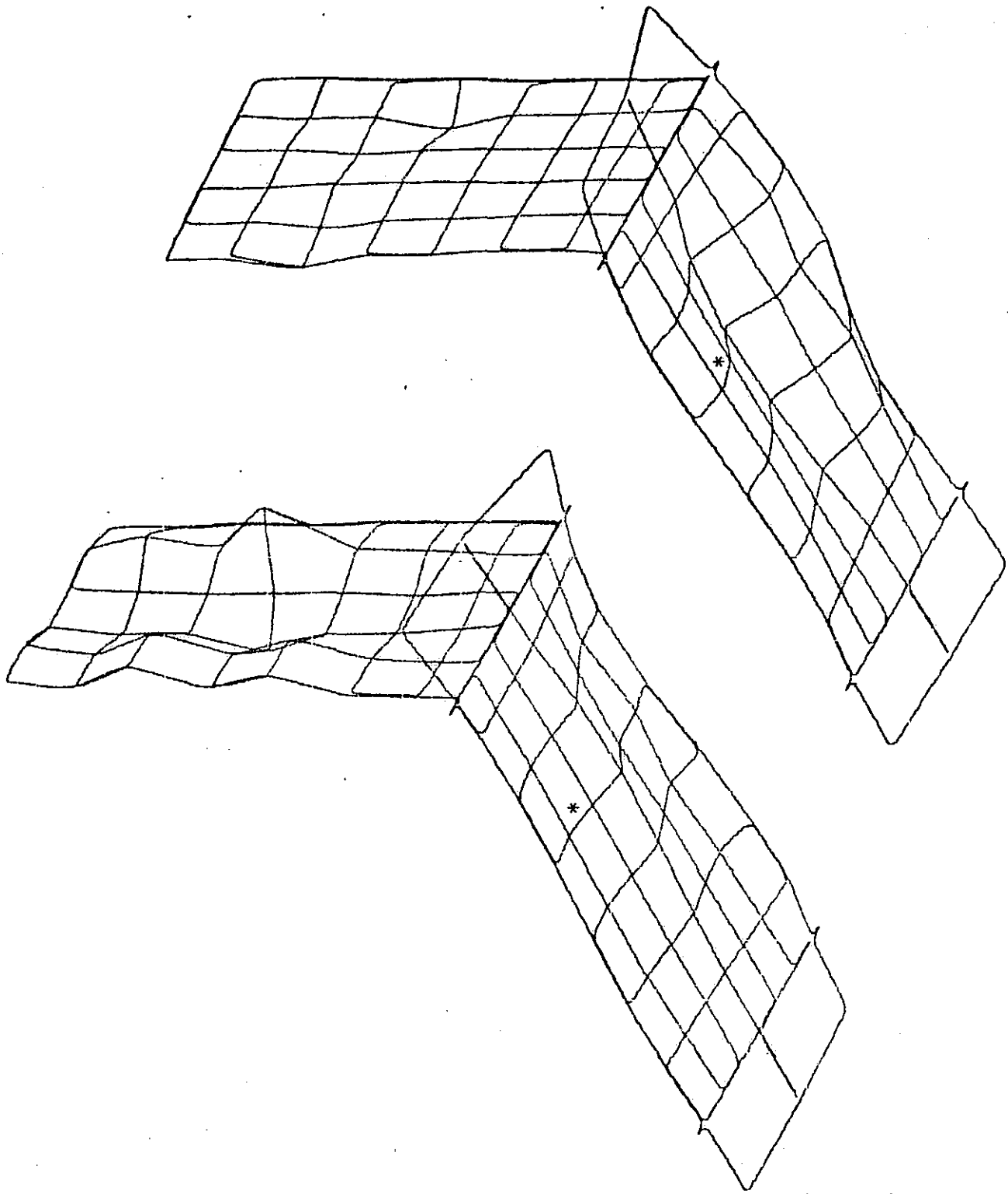

Figure 37. Typical Isometric Plots of Skin Stringer and Rib Panel Deformations, 217 Hz.

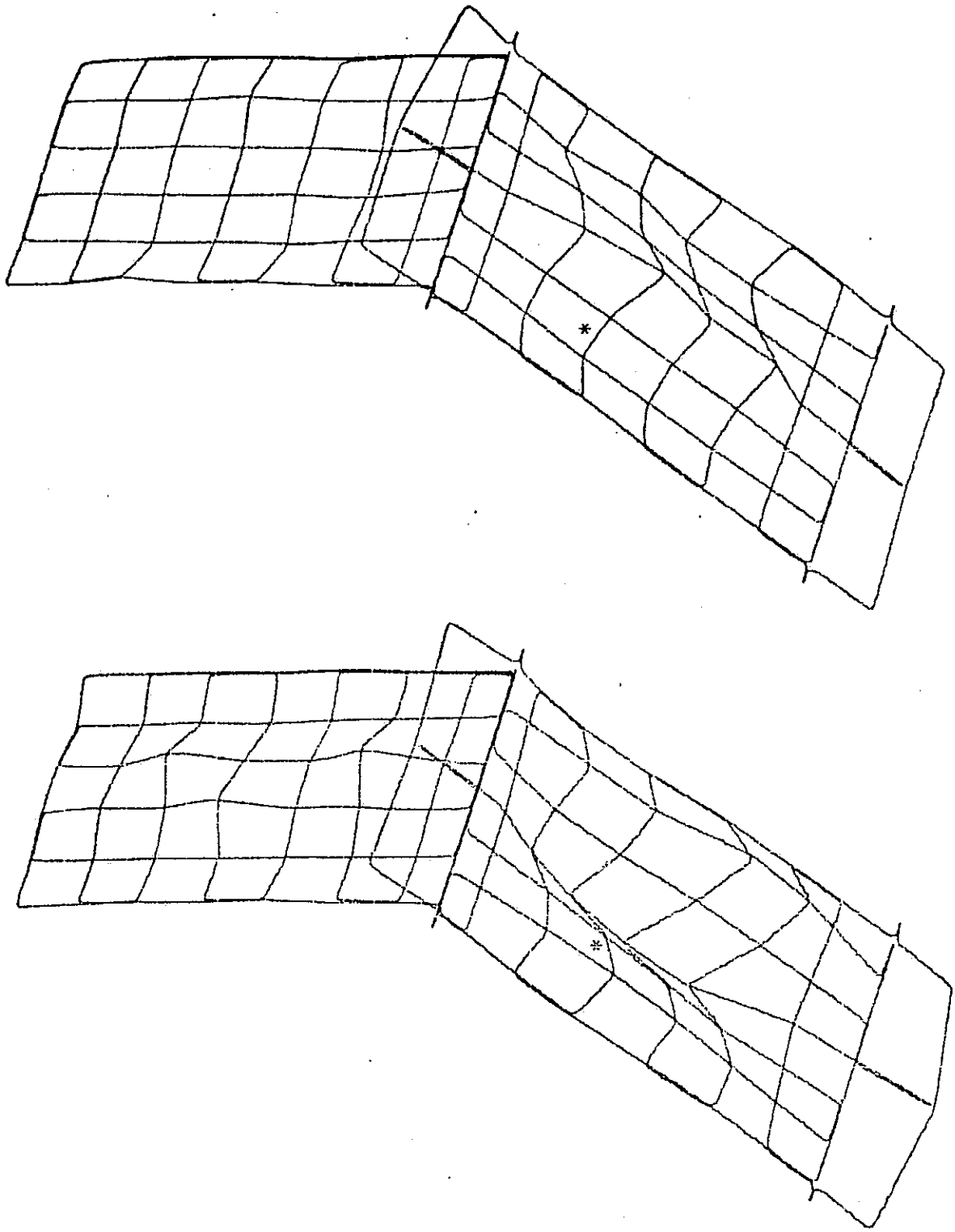

Figure 38. Typical Isometric Plots of Skin Stringer and Rib Panel Deformations, 231 Hz.

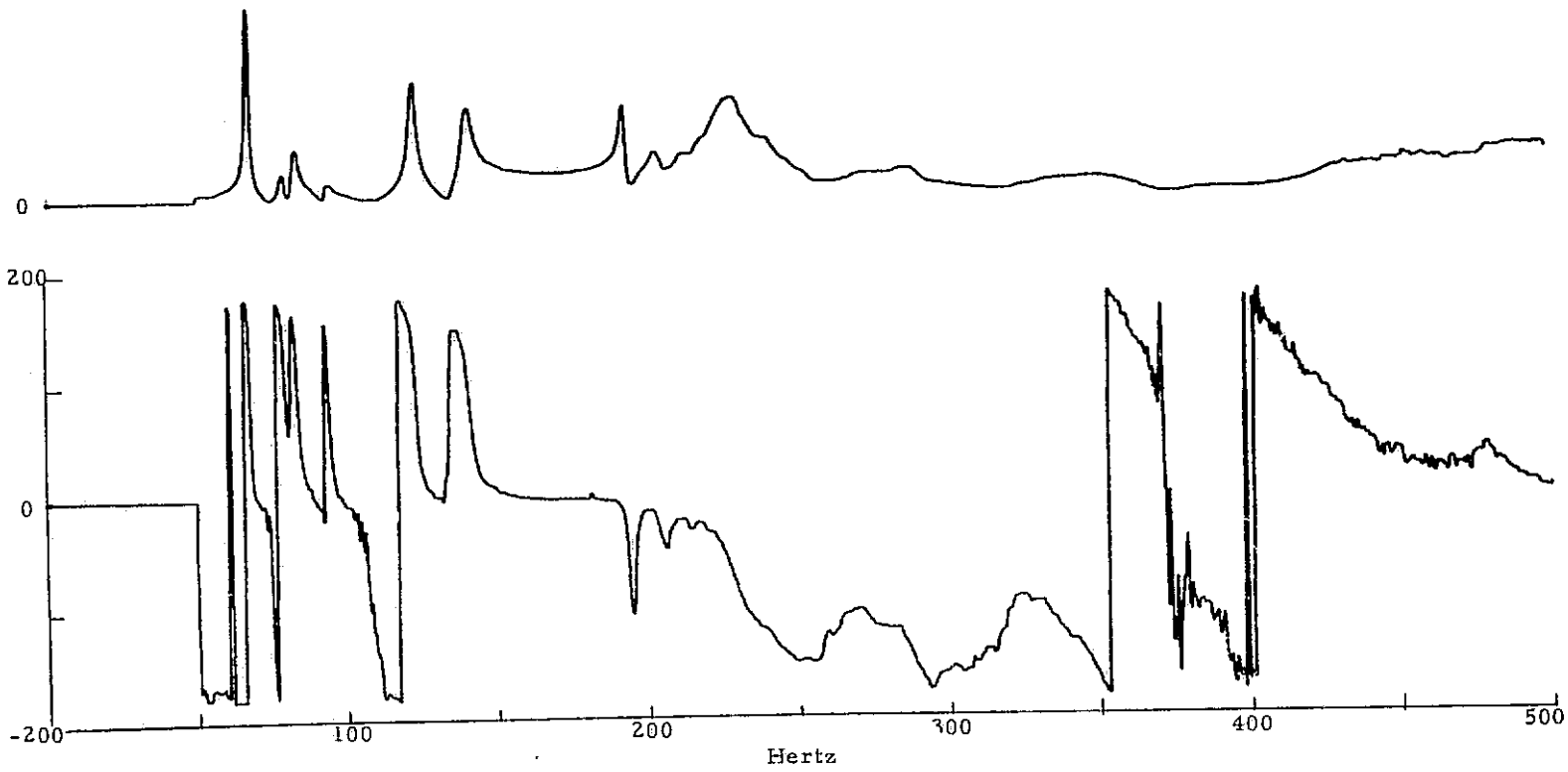

Figure 39. Typical Transfer Function on Skin-Stringer Panel (Ref. Figure 13, Midway between Positions 16 & 17).

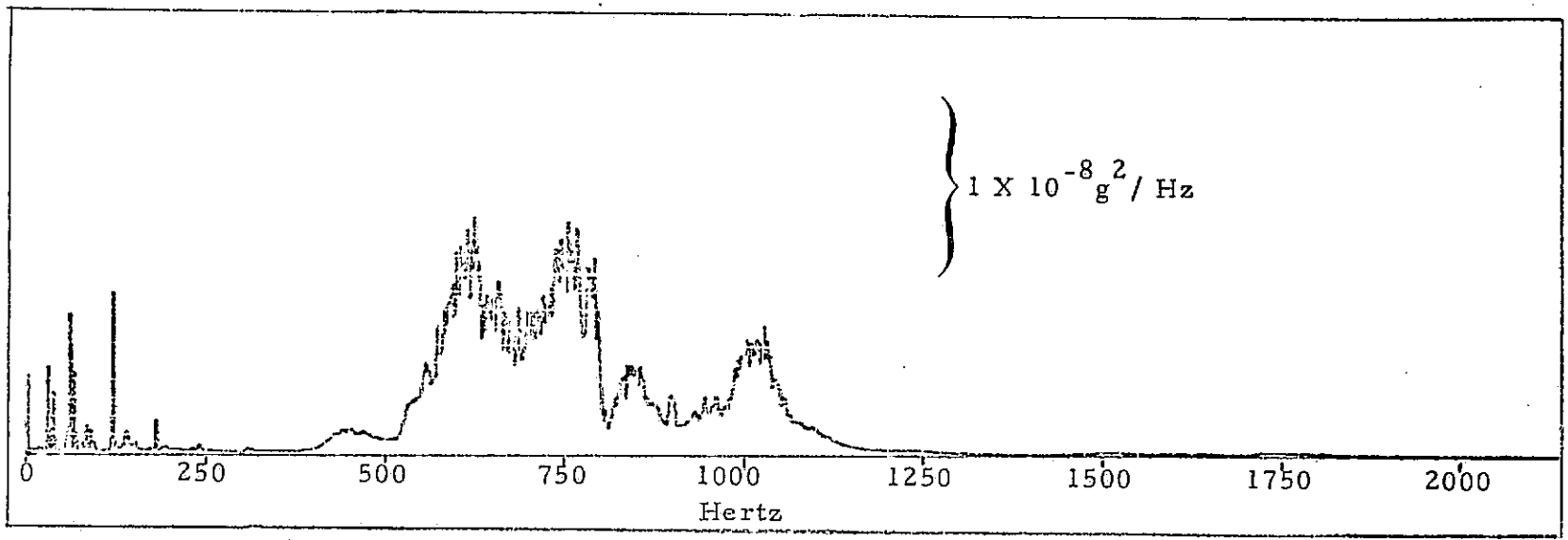

Figure 40. Power Spectrum of Accelerometer Signal on Skin-Stringer Panel behind Tile No. 12, Upper Left, Figure 12, near Position 23, Figure 13.

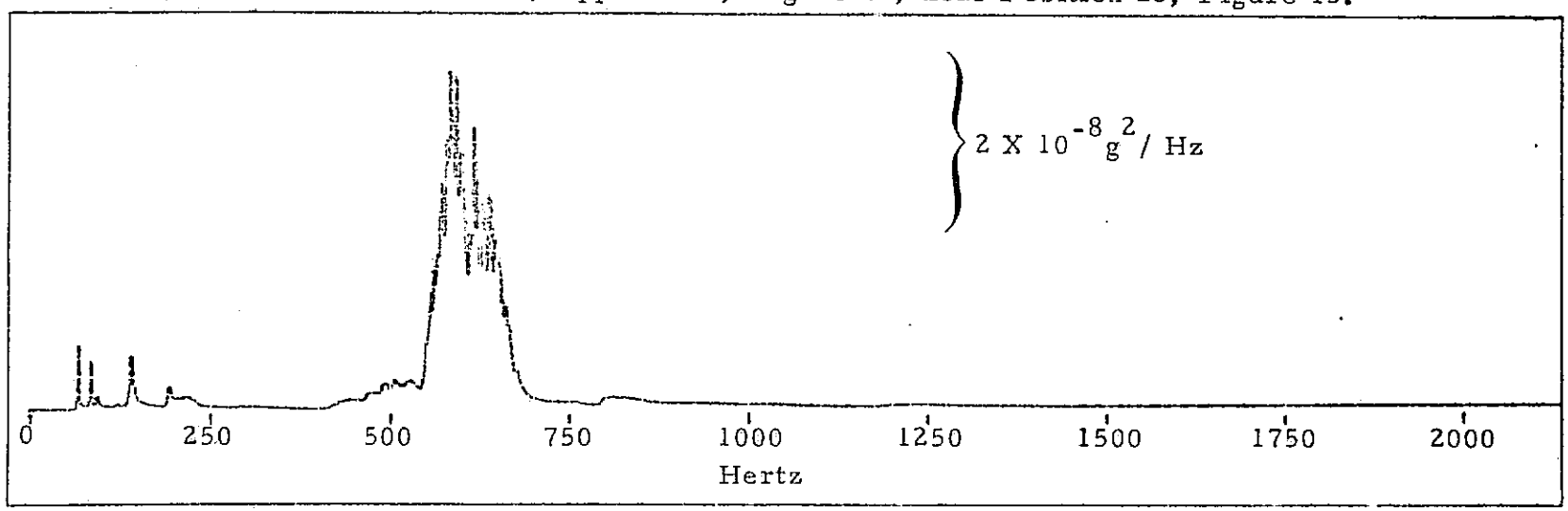

Figure 41. Power Spectrum of Accel rometer Signal from Upper Left Position on Tile No. 12, Figure 12.

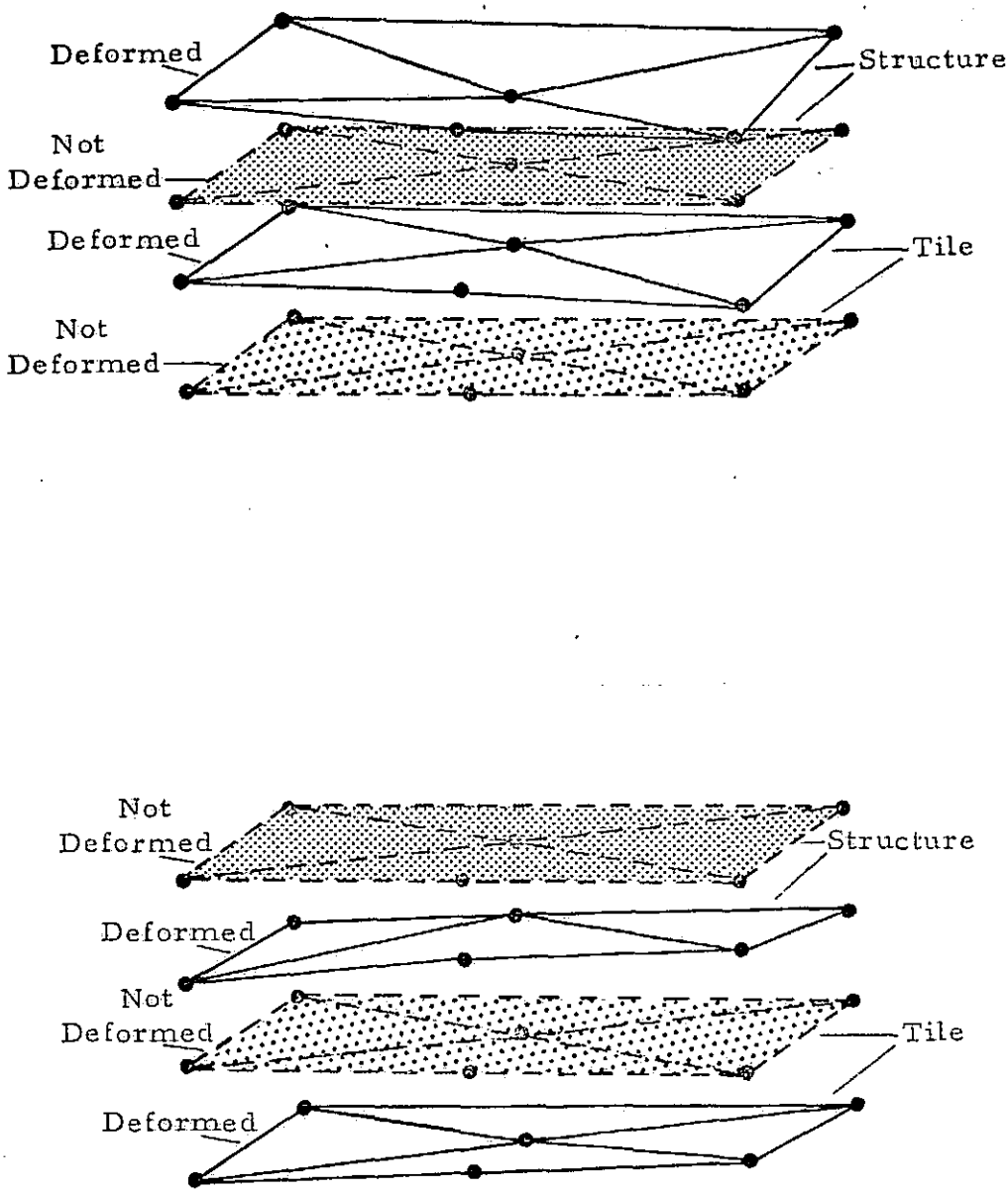

Figure 42. Single Tile Mode, 67 Hz.

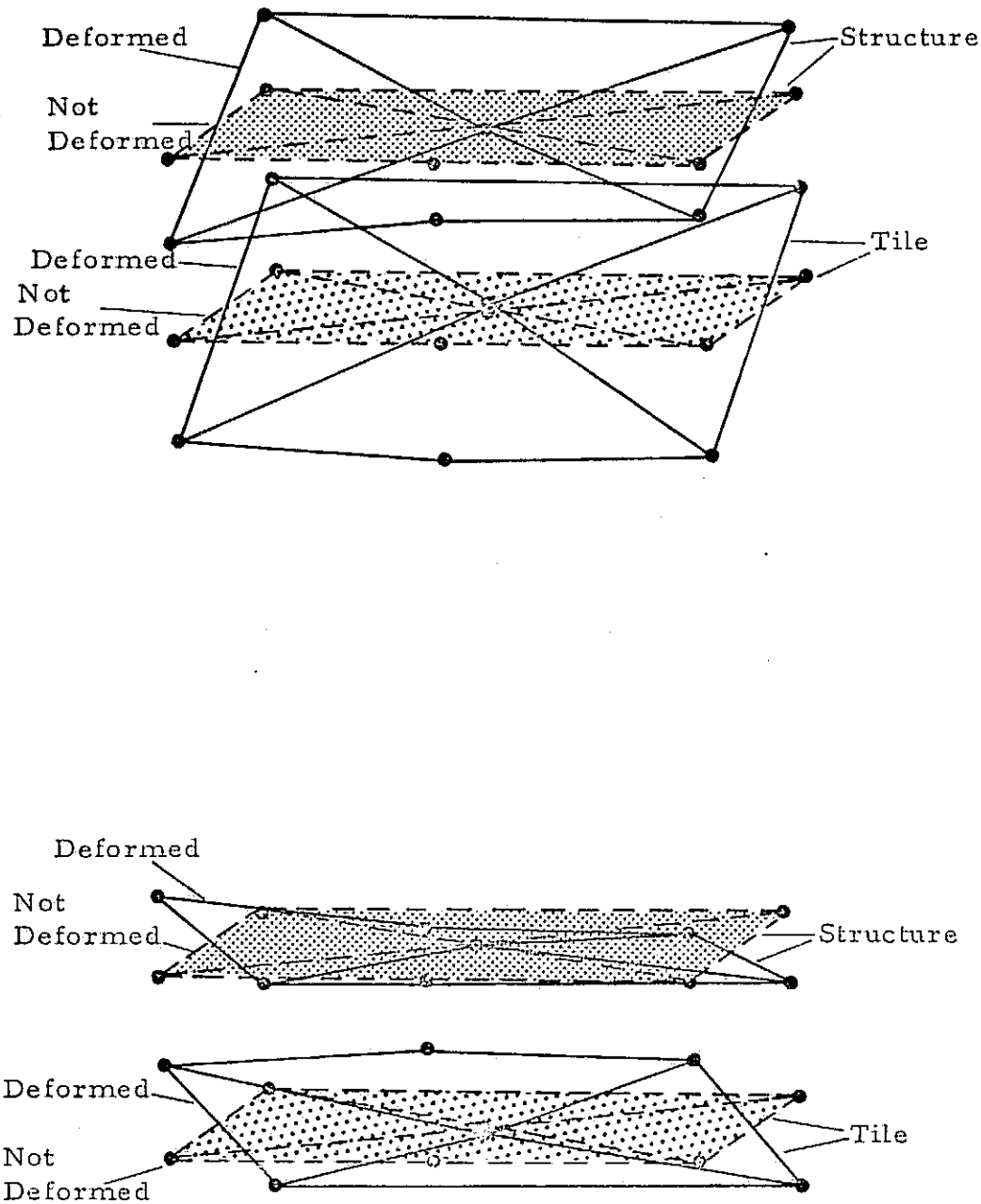

Figure 43. Single Tile Mode, 140 Hz.

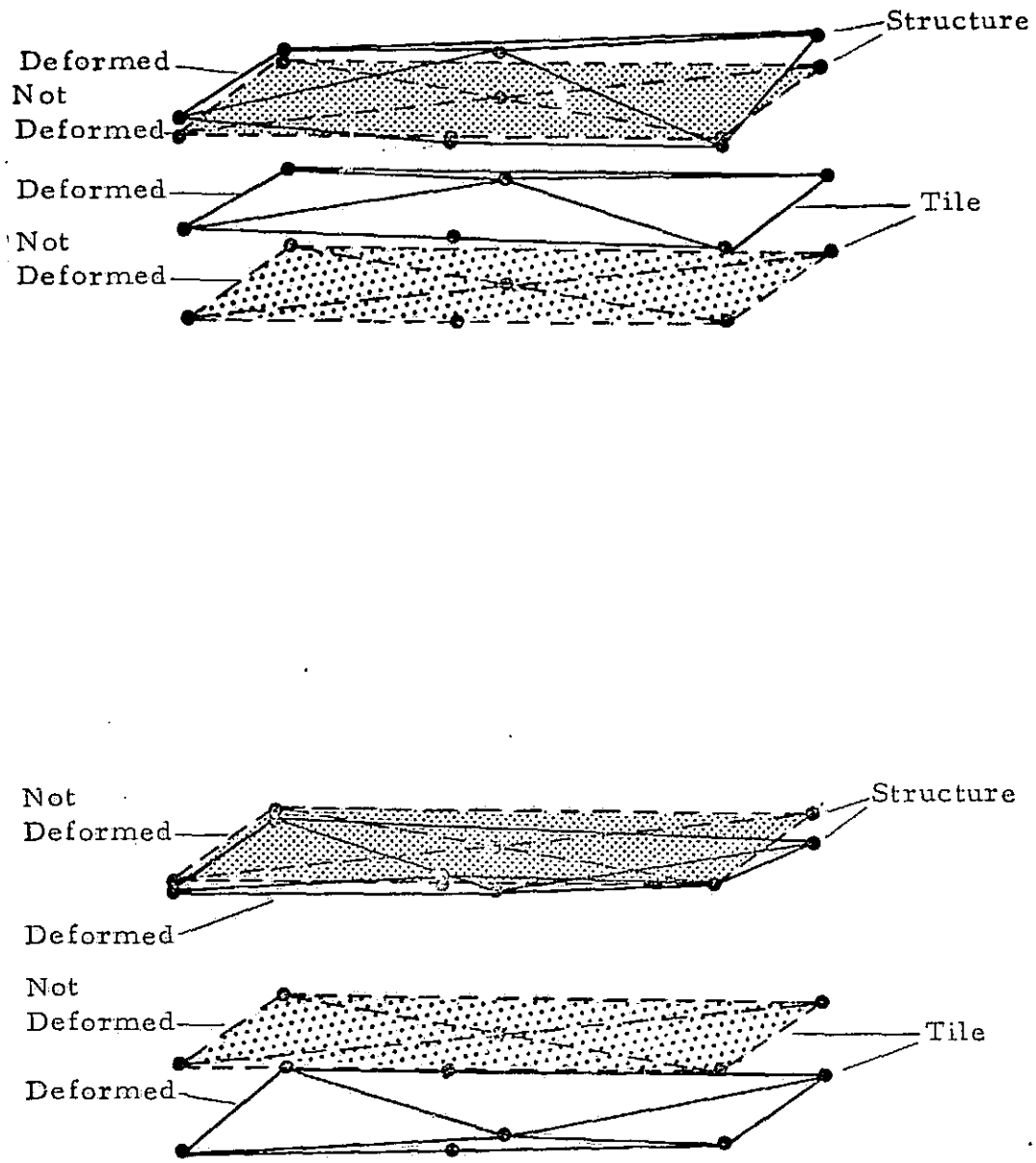

Figure 44. Single Tile Mode, 233 Hz.

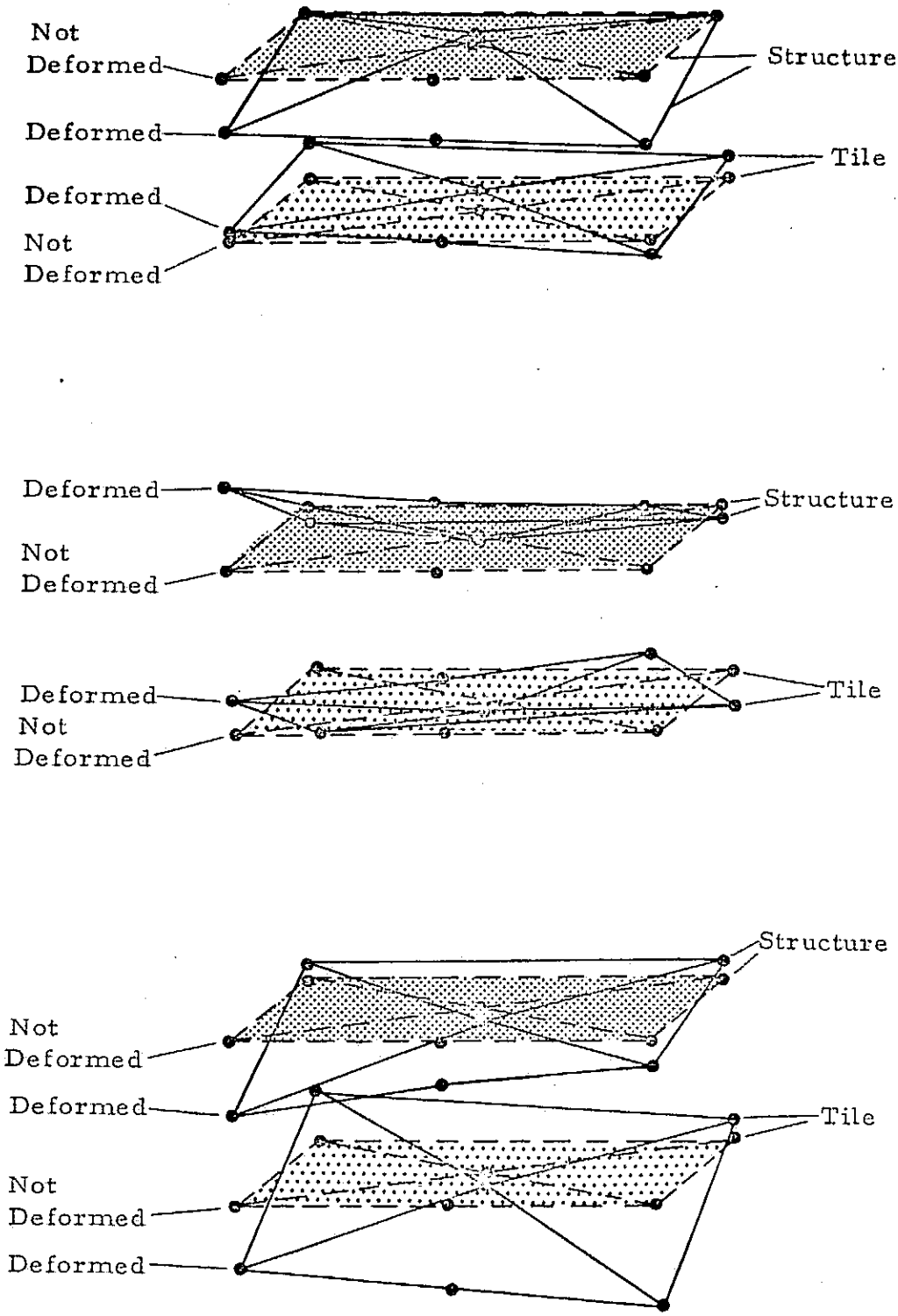

Figure 45. Single Tile Mode, 475 Hz.

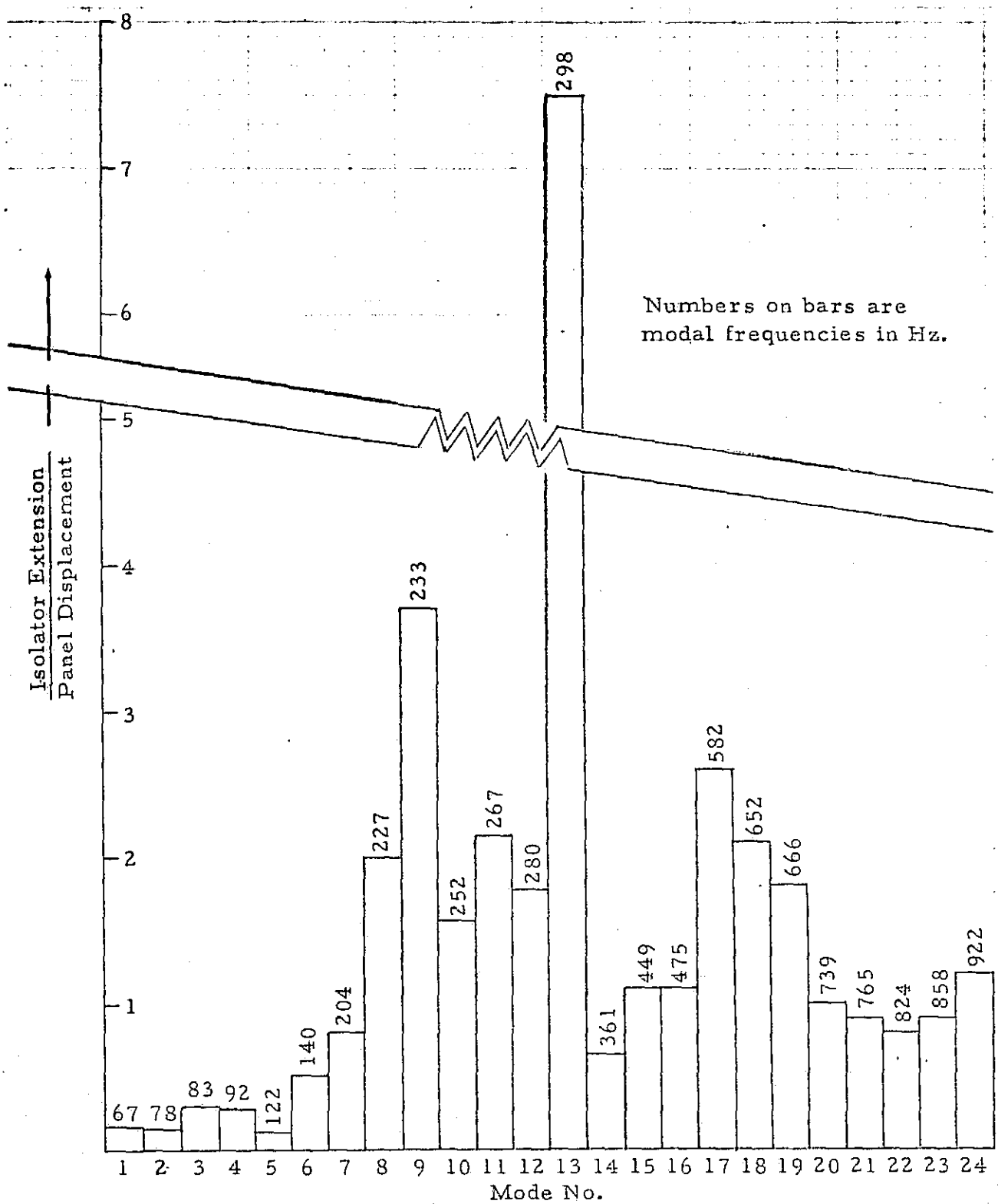

Figure 46. Ratio of Strain Isolator Extension or Compression to Panel Displacement for Entire Range of Resonant Response

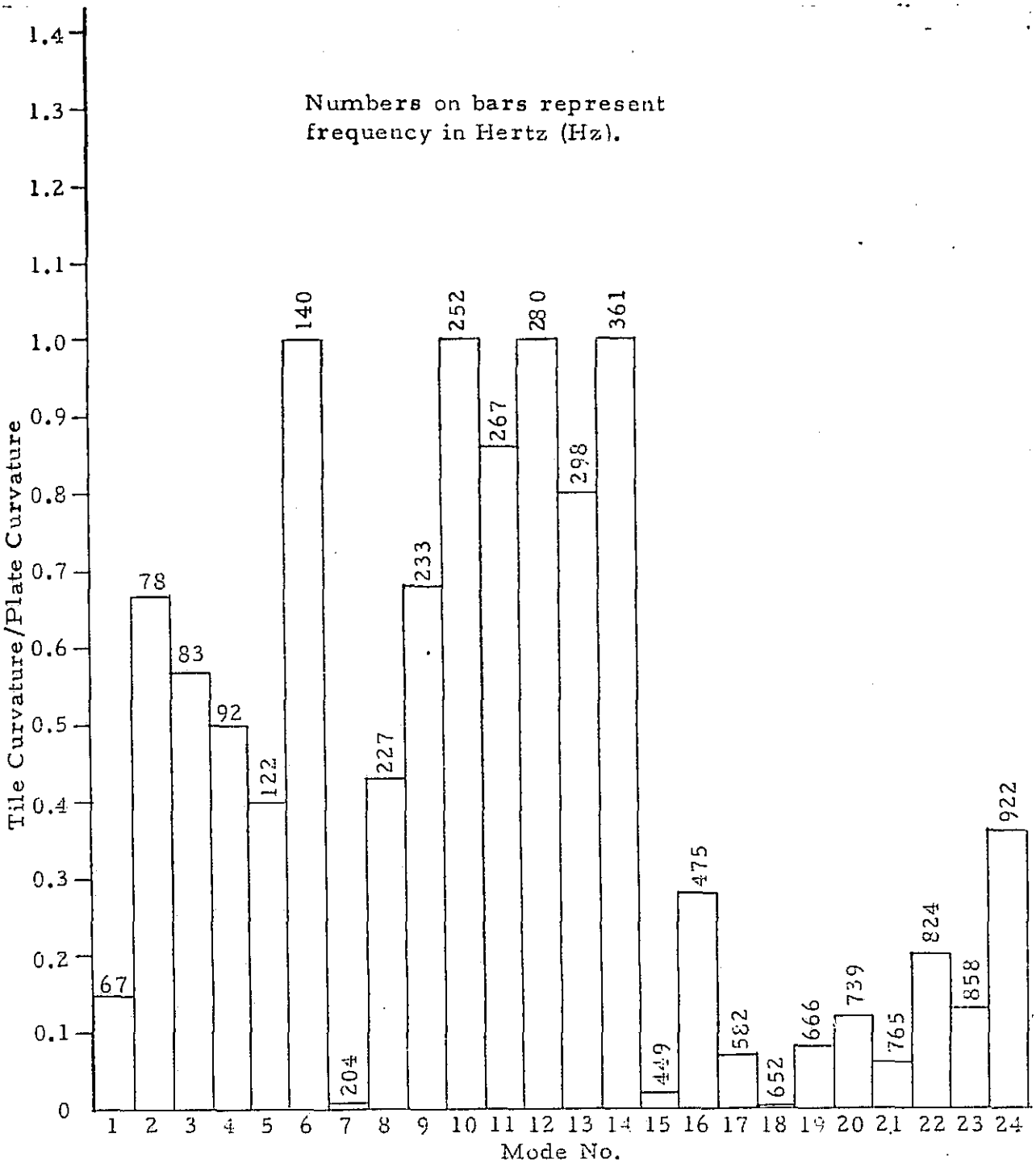

Figure 47. Ratio of Tile Curvature to Panel Curvature over Entire Range of Resonant Response.

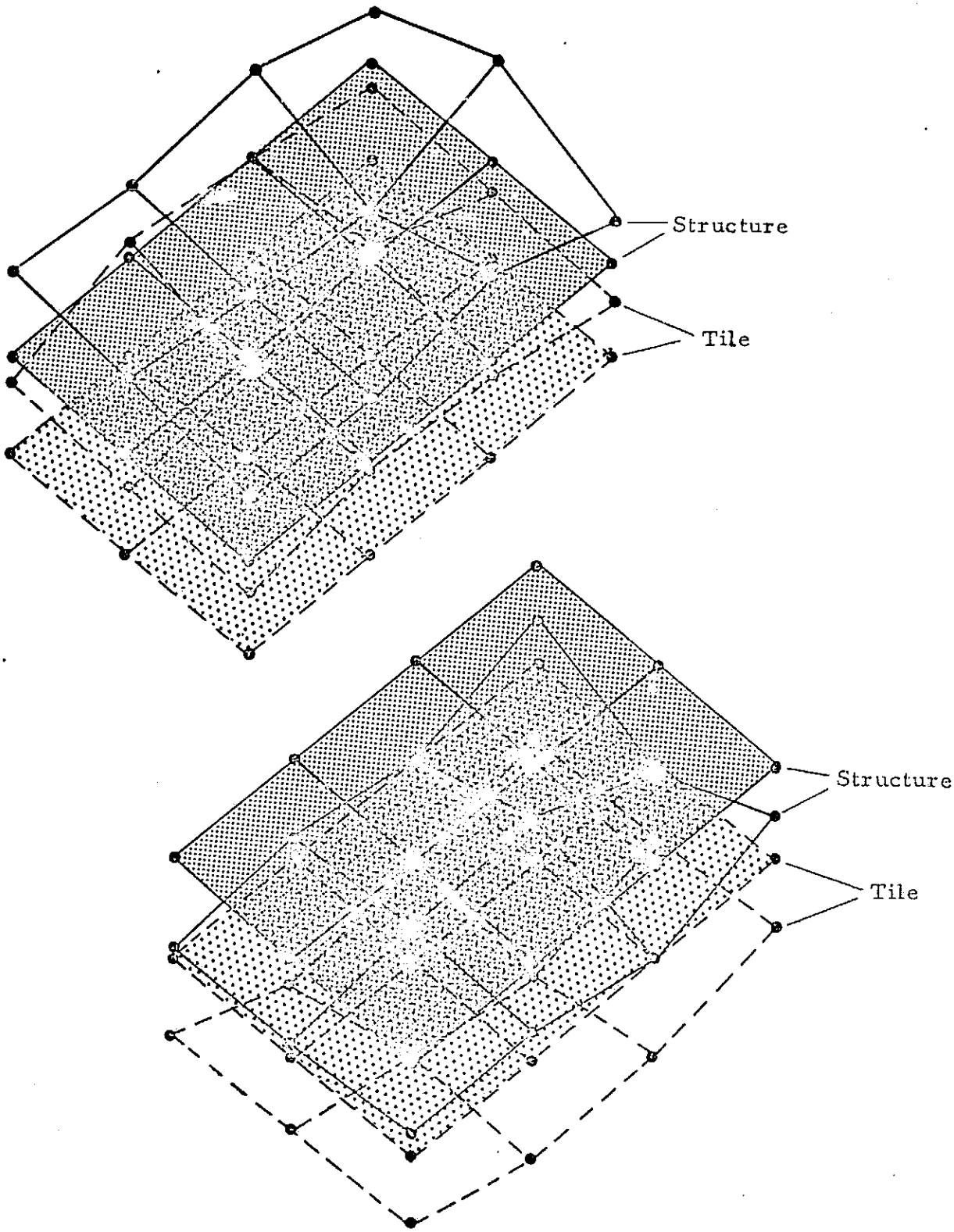

Figure 48. Mode of Tiles and Skin-Stringer Panel, 66 Hz.

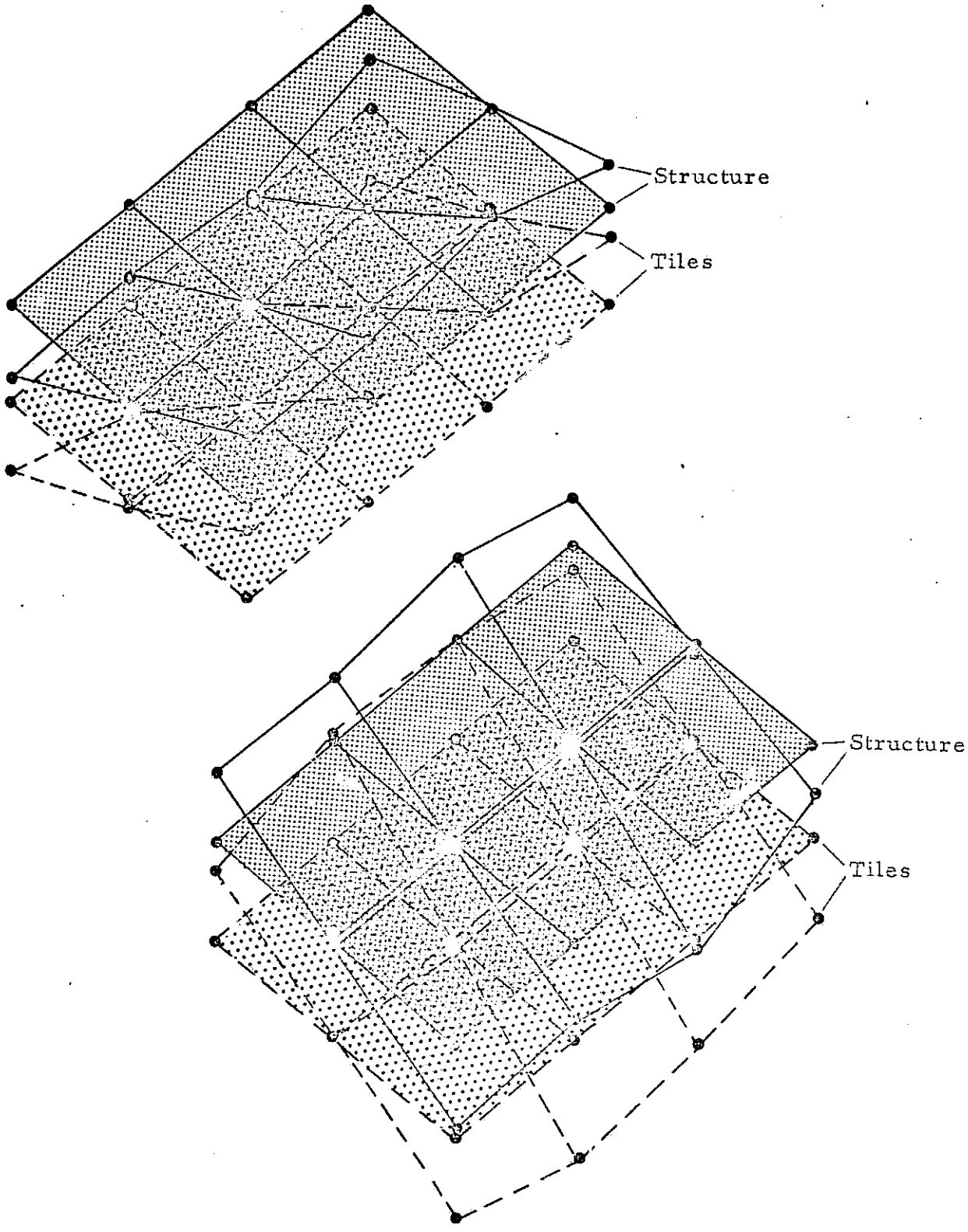

Figure 49. Mode of Tiles and Skin-Stringer Panel, 83 Hz.

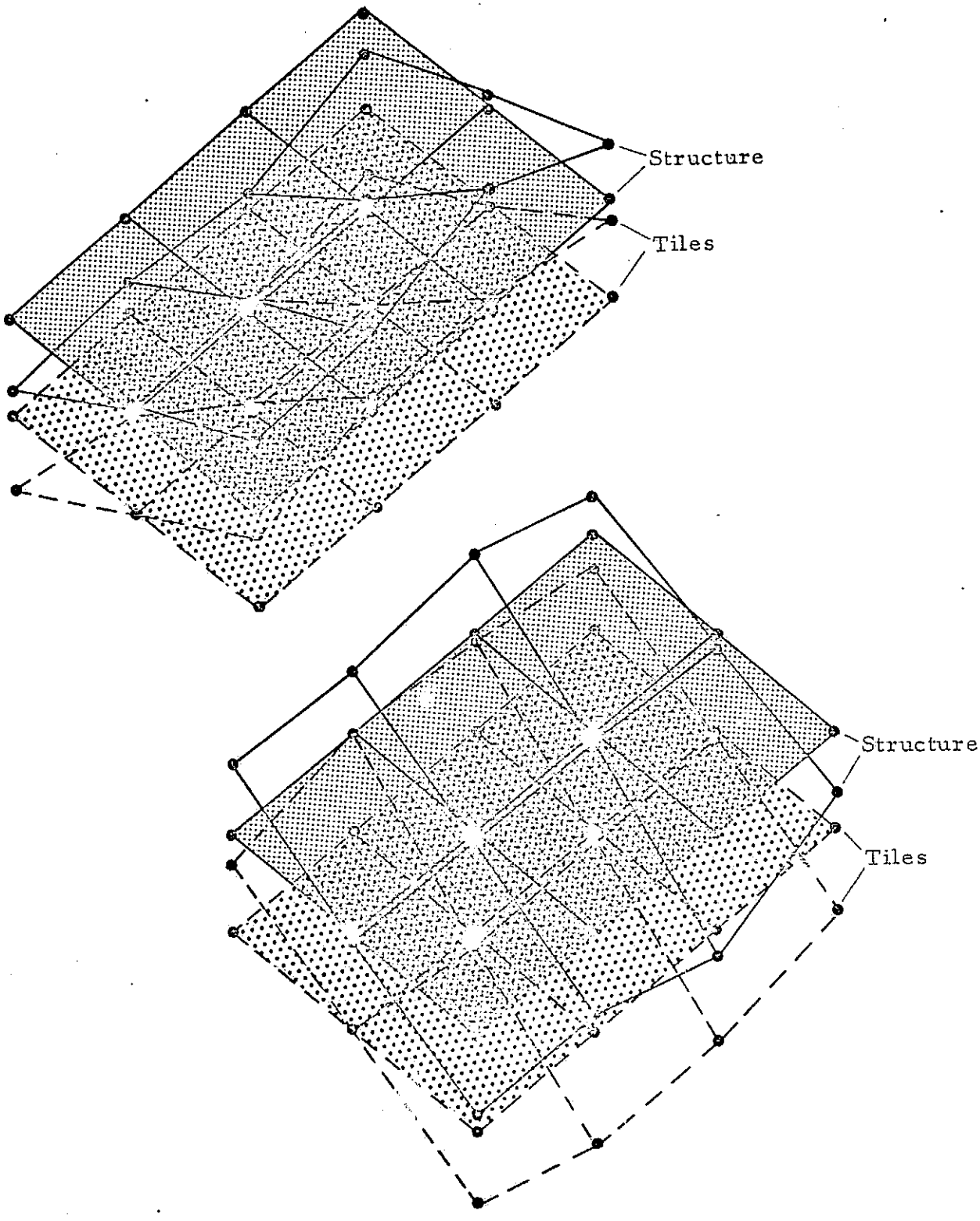

Figure 50. Mode of Tiles and Skin-Stringer Panel, 92 Hz.

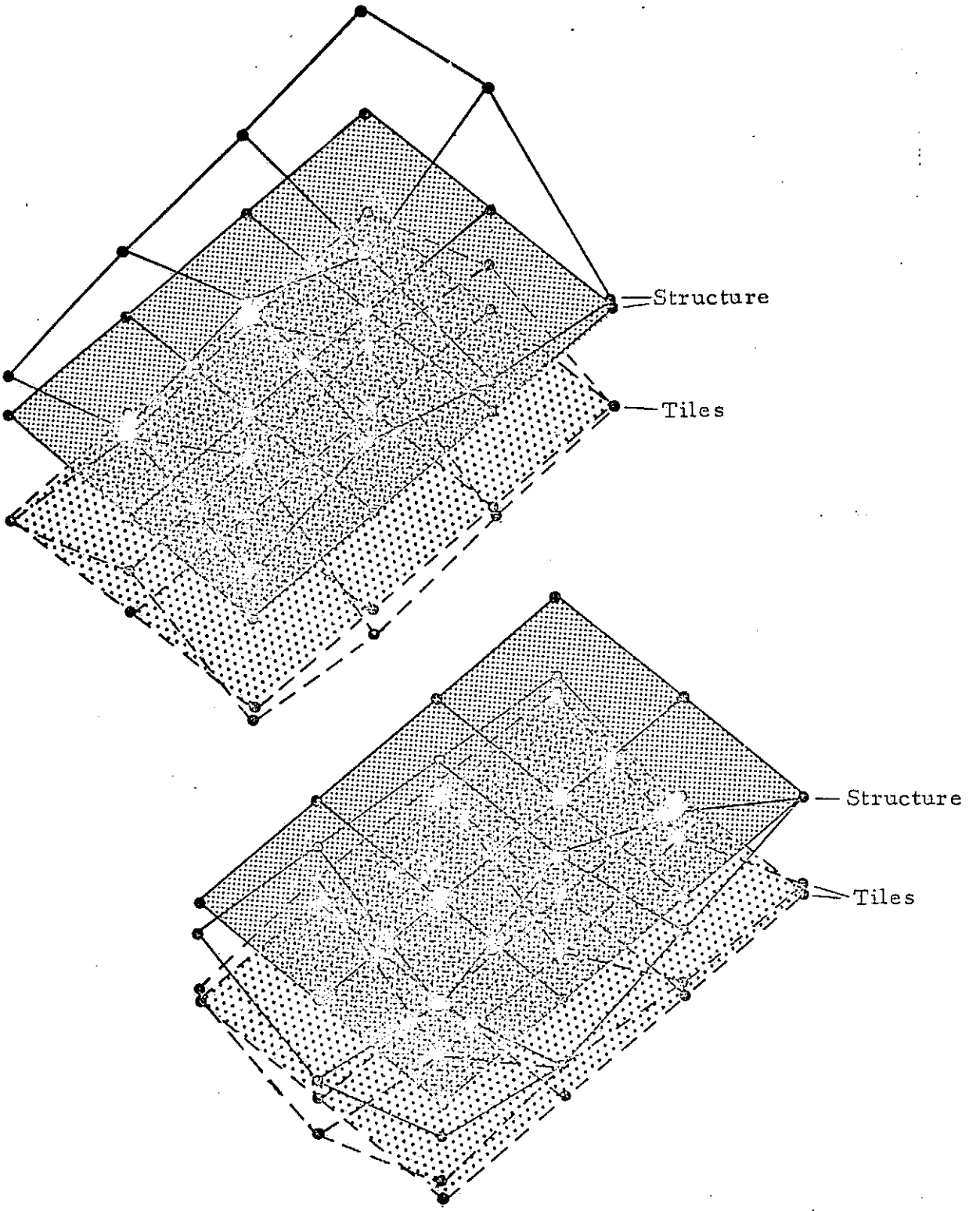

Figure 51. Mode of Tiles and Skin-Stringer Panel, 122 Hz.

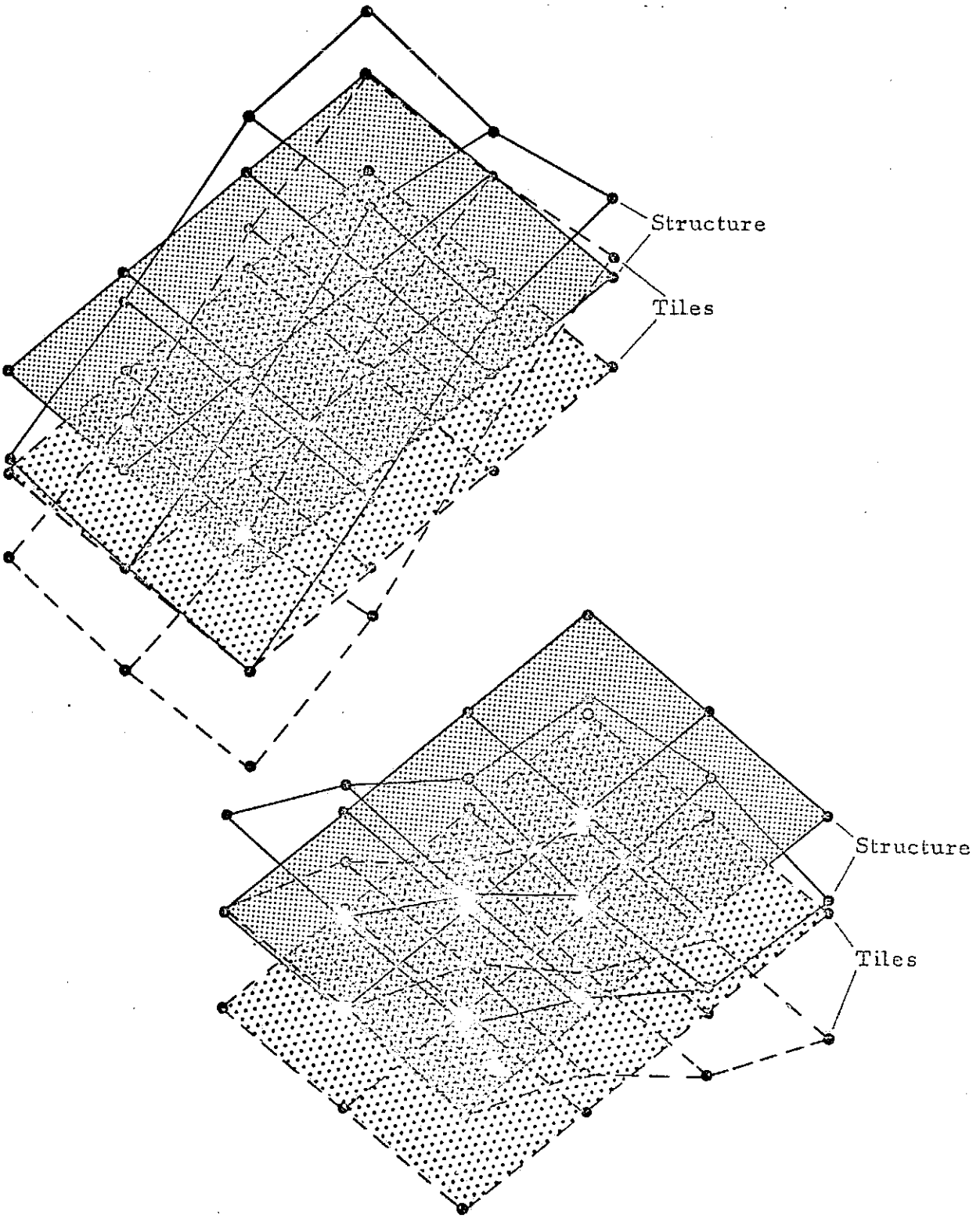

Figure 52. Mode of Tiles and Skin-Stringer Panel, 193 Hz.

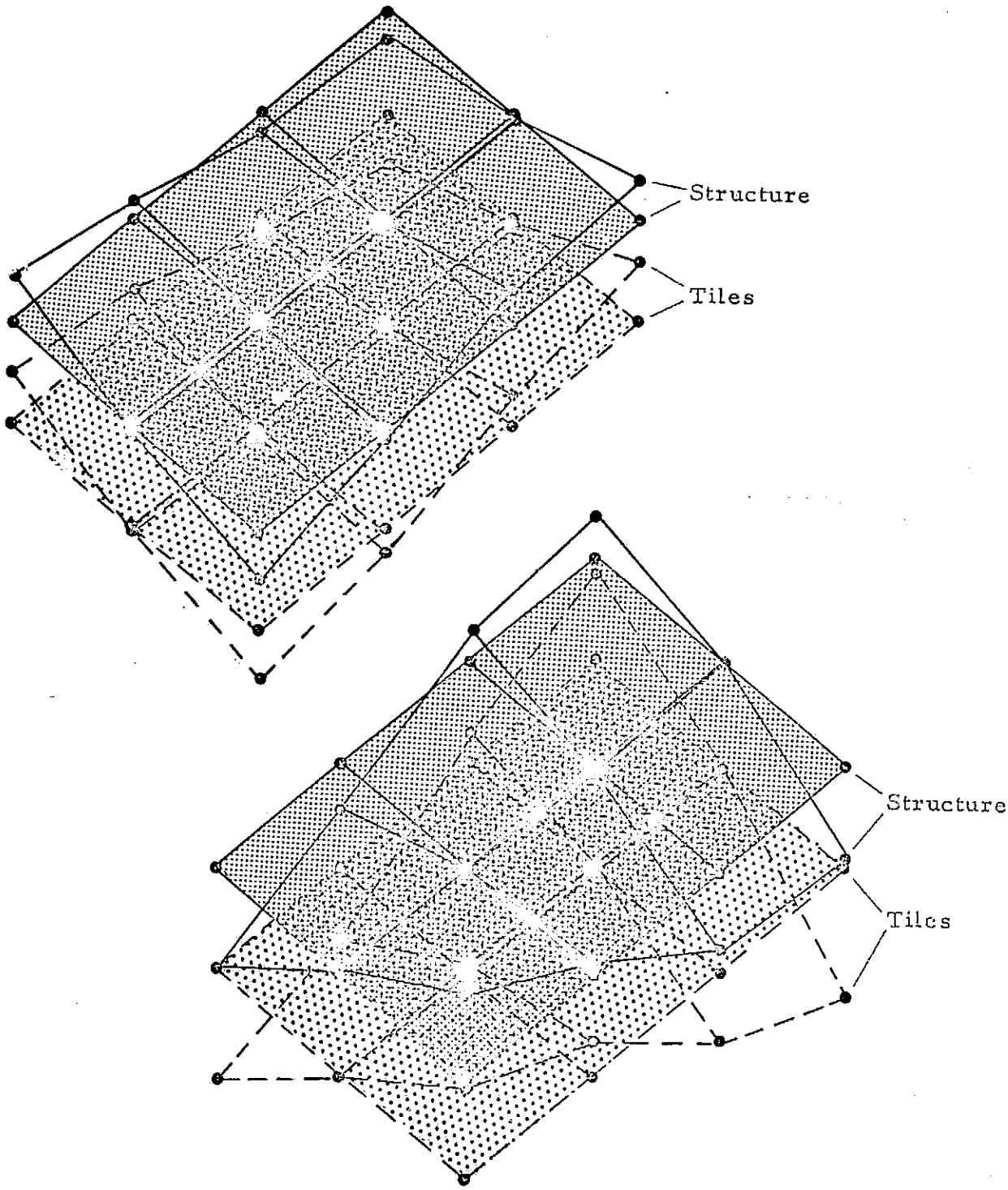

Figure 53. Mode of Tiles and Skin-Stringer Panel, 204 Hz.